Supramolecular aggregates in high magnetic fields

Jeroen Gielen

Supramolecular aggregates in high magnetic fields
Jeroen Constantijn Gielen
Thesis Radboud Universiteit Nijmegen - Illustrated
With references - With summary in Dutch
ISBN: 978-90-9025204-9

Supramolecular aggregates in high magnetic fields

Een wetenschappelijke proeve op het gebied van de
Natuurwetenschappen, Wiskunde en Informatica

Proefschrift

ter verkrijging van de graad van doctor
aan de Radboud Universiteit Nijmegen
op gezag van de rector magnificus prof. mr. S.C.J.J. Kortmann,
volgens besluit van het college van decanen
in het openbaar te verdedigen op vrijdag 28 mei 2010
om 13:00 uur precies

door

Jeroen Constantijn Gielen
geboren op 11 oktober 1983
te Utrecht

PROMOTOR: PROF. DR. IR. J. C. MAAN

COPROMOTOR: DR. P. C. M. CHRISTIANEN

MANUSCRIPTCOMMISSIE:
PROF. DR. R. J. M. NOLTE
PROF. DR. A. FASOLINO
DR. A. P. H. J. SCHENNING (TECHNISCHE UNIVERSITEIT EINDHOVEN)

Contents

Chapter 1

Introduction

History

In 1987, the Nobel Prize in Chemistry was awarded to Donald J. Cram, Jean-Marie Lehn, and Charles J. Pedersen "for their development and use of molecules with structure-specific interactions of high selectivity" [1]. It was a recognition for the synthesis of complex molecules and their importance in the emerging research field of supramolecular self-assembly. In this field, carefully designed (organic) molecules are used as building blocks for larger structures with a nano- or microscopic length scale, so called supramolecular aggregates. For such a bottom-up process, it is important to control intermolecular interactions in the same way that a synthetic chemist controls the formation of covalent bonds. Although these non-covalent interactions, like hydrogen bonding, π-π interactions and Van der Waals forces are relatively weak compared to a covalent bond, life would not be possible without them: the double helix of DNA is one of the most important examples.

In the last decades, the field has greatly expanded, and the discoveries of Cram, Lehn and Pederson have proven to be of great use. Driven by the miniaturization of electronics and the rise of nanotechnology, supramolecular self-assembly emerged as an attractive strategy for the bottom-up design of small structures and devices [2]. Compared to top down methods like lithography, it has many advantages. Extremely small structures can be made, the production of the molecular building blocks is very versatile and relatively cheap, the aggregates can easily be processed in solution and have the possibility of self-repair. Because of the weak interactions, a dislocated molecule can be readjusted or replaced, to restore the internal periodicity. This has lead to a variety of nanostructures with different shapes and sizes, i.e. wires, ribbons, spheres and cylinders [3–6].

From an application point of view, this approach has been very successful, with examples in sensors, memory elements, catalysts, artificial light harvesting complexes and drug delivery systems [7–12]. From a scientific point of view, the formation is a fascinating research topic in itself, and it allows for studying physical phenomena on the nano-scale, like confinement effects [13] or transportation of light [12, 14], attracting a diverse group of scientists to the field of supramolecular self-assembly. The efforts that merited the Nobel Prize were of a chemical nature: the synthesis of new and complex molecules. In the last decades, it has evolved into a truly interdisciplinary field: chemistry is required for the synthesis of the molecular building blocks, complex biological systems provide inspiration for the design, and physics is required for characterization, modeling and understanding the properties of supramolecular assemblies.

Progress and challenges

The joined efforts of the different disciplines have lead to great progress over the years, indicated by the numerous examples of self-assembled nanostructures. Although many questions have been answered, there is still a long way to go. Here, we mention some successes and challenges.

Many important factors influencing the *type of aggregate* (i.e. the shape and internal organization) have been identified. Both external influences like solvent, temperature and pH, as well as molecular properties like solubility and the size of the conjugated area. For example, for “simple” amphiphiles it is known that increasing the carbon chain length causes a change from cylindrical to spherical micelles [15]. For π-conjugated organic molecules, several interactions are involved, making a prediction of the aggregate type very difficult. A structural variation of the different parameters is required to reveal the individual contributions.

Things get even more complex when multiple types of building blocks are involved within a single aggregate. Examples are *hybrid materials* that consist of organic molecules and inorganic material, using one material to steer the aggregation of the other [16, 17]. Other examples are *templated assemblies* to control the aggregate size [18]. Self-assembly gives a broad size distribution of aggregates, whereas most applications rather require a well-defined aggregate size. However, making nanostructures with a monodisperse pre-defined size, still remains a formidable task.

Several theoretical models have been successfully developed, and some important factors that determine the type of aggregation have been identified, like electronic, structural of hydrophobic effects [19, 20]. In many cases, inspiration for *kinetic-* and *thermodynamic models* was found in present biophysical literature on the aggregation of proteins. The requirement that a system minimizes its free energy leads to the formation of complex ordered structures. To extract the relevant parameters and translate them to molecular properties, those models have to be compared to different aggregation processes.

The number and quality of *techniques* to characterize aggregates have seriously grown. The toolbox of a modern supramolecular scientist ranges from microscope techniques, spectroscopic techniques, scattering techniques to scanning probe techniques; all giving different pieces of information about the aggregates, which need to be combined to obtain the complete picture. Improving the techniques will lead to an increasing understanding of the process of aggregate, and magnetic fields can play an important role here.

A magnetic field gives a well-defined, contact free, nondestructive, homogeneous force on many type of objects. For example, magnetic fields have been used in the past as an alignment tool for liquid crystals, protein crystals, polymers and biological systems [21–24]. However, magnetic fields are also ideal for aligning and studying supramolecular aggregates, providing a valuable addition to the toolbox. Despite the limited availability of strong magnetic fields, the rare use of this technique is remarkable. The organic molecules used for self-assembly are anisotropic, to achieve directionality in the intermolecular non-covalent interactions [2]. Consequently, the magnetic and optical properties of the molecules are also anisotropic, which enables the magnetic alignment of aggregates and the measurement of the alignment using linear birefringence [25, 26]. The degree of alignment depends on the size, flexibility, internal organization and the degree of order of the entire aggregate. The use of magnetic fields is therefore a great step forwards compared to existing characterization methods.

Results

The experiments in this thesis use the induced alignment to investigate different supramolecular aggregates in high magnetic fields. We have measured aspects like the type of aggregate, the internal organization, and the kinetic and thermodynamic properties of the formation process. We focus on fiber shaped or semi-one-dimensional aggregates in solution, which are of special interest. Most importantly, they are excellent model systems. Describing the growth and kinetics in the case where aggregates can break and recombine, and where molecules can only attach and detach at the end of the aggregate, is easier than modeling 3D structures. In contrast to solid aggregates, they allow for an investigation of the flexibility, which is an indication for the type and strength of the intermolecular interactions. Additionally, these type of aggregates are promising materials for nanoscale components in supramolecular electronics, optical waveguides, or as thermo-reversible gelators [14, 27–30].

We have investigated cylindrical thiophene aggregates, flexible cyanine fibers, chiral oligo-phenylenevinylene stacks and shape-persistent macrocycle aggregates. The aggregates were formed by dissolving the monomers in a proper solvent, and forcing the aggregation by cooling or ion-addition. We have found that all the aggregates align in a magnetic field. Exploiting this alignment to measure the size and internal organization, we have found that the aggregation-type of the thiophene molecules drastically changes when slightly changing the solvent. The process is irreversible, one practically cannot switch back and forth between the two structures. For the cyanine fibers, a reversible change of the aggregate morphology can be induced by a magnetic field: applying a magnetic field transforms the flexible fibers into rigid rods.

In addition to external influences, the chemical properties of the molecule are important for the aggregation. For the macrocycles, we have found that the long polystyrene tails slow down the formation of ordered aggregates, allowing us to link the kinetics to molecular properties. For the oligo-phenylenevinylene molecules, the temperature induced growth was compared with theoretical models. We have found that the properties of the conjugated core probably causes the assembly process to be a cooperative process.

All these effects were found by investigating the behavior of the aggregates in strong magnetic fields. This technique provides information that cannot be obtained by other methods, giving a valuable contribution towards an improved understanding on many aspects involved in the formation of supramolecular aggregates.

Outline

This thesis is organized as follows: chapter 2 describes the theory of the alignment of supramolecular aggregates in a magnetic field. We can calculate the degree of alignment and the induced birefringence, both the molecular- and form birefringence, for aggregates in solution with any size, shape and internal organization. The only required parameters are the molecular static polarizabilities, which can be calculated using MOPAC, and the molecular diamagnetic susceptibilities, which can be estimated by summing the contributions from the individual chemical groups [31]. This allows for a quantitative interpretation of magnetic birefringence data, allowing for an accurate measurement of the aggregate size and a determination of the internal structure of the aggregates.

Chapter 3 describes the use of laser light scattering to measure the size and shape of aggregates in solution. An overview is given of the experimental setup and sample preparation, and the principles of dynamic and static light scattering are discussed and illustrated with a few examples. In a magnetic field, the orientational distribution function of the aggregates changes and thereby the diffusivity. We discuss the consequences of the alignment for a light scattering experiment, and show that this improves the accuracy in the case of anisotropically shaped aggregates.

Chapter 4 describes cylindrical aggregates of sexithiophene molecules. The use of X-rays on magnetically aligned aggregates allowed us to reveal the shape and internal aggregate structure: a multi-walled rigid cylinder, which is considerably different from aggregate types found in other solvents. The aggregates of this semiconducting material can thus be tuned by using different solvents, which allows us to build nanostructures with desired functionalities, especially in combination with the alignment in a magnetic field.

Chapter 5 deals with fiber shaped aggregates of thiacyanine molecules, which show the peculiar behavior of a changing flexibility in a magnetic field. In only 2 T, the fiber morphology changes from a flexible fiber, with a persistence length of a few micrometer, to a completely rigid rod. To investigate the origin of this reversible change, we have characterized the magnetic properties of the fibers, using a complementary set of techniques, including magnetic birefringence, polarized absorbance and small angle X-ray scattering. We have found a simple brickwork arrangement of the thiacyanine molecules in the fiber, and that the rigidification of the fibers is caused by a field induced change in the internal structure.

Chapter 6 focuses on the formation mechanism of oligo (p-phenylenevinylene) aggregates. Using light scattering and magnetic birefringence in addition to spectroscopic techniques and atomic force microscopy, we succeeded in a full characterization of the aggregate growth, and we have determined the corresponding thermodynamic parameters. A proper understanding of the growth mechanisms allows for a better tuning of the supramolecular aggregates and their properties to have the desired functionalities.

The last chapter shows that magnetic alignment can be used to determine aggregation kinetics. After cooling a monomeric solution of macrocycle molecules, we find a fast formation of disordered objects, followed by a very slow transition to ordered fibers. The slow transition is probably caused by the polystyrene tails attached to the molecular backbone. Linking aggregation kinetics to molecular properties, will lead to a better understanding of the mechanisms by which molecules self-assemble, allowing for a more rational design of the molecular building blocks.

References

[1] Lehn, J.-M., Supramolecular Chemistry - Scope and Perspectives. Molecules - Supermolecules - Molecular devices. *Nobel Lecture*, 1987.

[2] Hoeben, F.J.M., Jonkheijm, P., Meijer, E.W., Schenning, A.P.H.J., *Chemical Reviews*, **105** (4), 1491-1546, 2005.

[3] Briseno, A.L., Mannsfeld, S.C.B., Jenekhe, S.A., Bao, Z., Xia, Y., *Materials Today*, **11** (4), 38-47, 2008.

[4] Jung, J.H., Do, Y., Lee, Y.-A., Shimizu, T., *Chemistry - A European Journal*, **11** (19), 5538-5544, 2005.

[5] Ryu, J.-H., Hong, D.-J., Lee, M., *Chemical Communications*, (9), 1043-1054, 2008.

[6] Wang, Z., Medforth, C.J., Shelnutt, J.A., *Journal of the American Chemical Society*, **126** (49), 15954-15955, 2004.

[7] Hickman, J.J., Ofer, D., Laibinis, P.E., Whitesides, G.M., Wrighton, M.S., *Science*, **252** (5006), 688-691, 1991.

[8] Huang, J., Virji, S., Weiller, B.H., Kaner, R.B., *Journal of the American Chemical Society*, **125** (2), 314-315, 2003.

[9] Tseng, R.J., Huang, J., Ouyang, J., Kaner, R.B., Yang, Y., *Nano Letters*, **5** (6), 1077-1080, 2005.

[10] Hoogenboom, R., Rogers, S., Can, A., Becer, C.R., Guerrero-Sanchez, C., Wouters, D., Hoeppener, S., Schubert, U.S., *Chemical Communications*, 5582-5584, 2009.

[11] Beletskaya, I., Tyurin, V.S., Tsivadze, A.Y., Guilard, R., Stern, C., *Chemical Reviews*, **109** (5), 1659-1713, 2009.

[12] Vlaming, S.M., Augulis, R., Stuart, M.C.A., Knoester, J., Van Loosdrecht, P.H.M., *The Journal of Physical Chemistry B*, **113** (8), 2273-2283, 2009.

[13] Lagoudakis, P.G., De Souza, M.M., Schindler, F., Lupton, J.M., Feldmann, J., *Physical Review Letters*, **93**, 257401, 2004.

[14] Takazawa, K., *Journal of Physical Chemistry C*, **111** (24), 8671-8676, 2007.

[15] Jones, R.A.L., Soft Condensed Matter, Oxford University Press, Oxford, 2002.

[16] Mann, S., *Nature Materials*, **8** (10), 781-792, 2009.

[17] Van Herrikhuyzen, J., George, S.J., Vos, M.R.J., Sommerdijk, N.A.J.M., Ajayaghosh, A., Meskers, S.C.J., Schenning, A.P.H.J., *Angewandte Chemie International Edition*, **46** (11), 1825-1828, 2007.

[18] Janssen, P.G.A., Jabbari-Farouji, S., Surin, M., Vila, X., Gielen, J.C., de Greef, T.F.A., Vos, M.R.J., Bomans, P.H.H., Sommerdijk, N.A.J.M., Christianen, P.C.M., Leclère, P., Lazzaroni, R., Van der Schoot, P., Meijer, E.W., Schenning, A.P.H.J., *Journal of the American Chemical Society*, **131** (3), 1222-1231, 2009.

[19] Frieden, C., *Protein Science*, **16** (11), 2334-2344, 2007.

[20] De Greef, T.F.A., Smulders, M.M.J., Wolffs, M., Schenning, A.P.H.J., Sijbesma, R.P., Meijer, E.W., *Chemical Reviews*, **109** (11), 5687-5754, 2009.

[21] De Gennes, P.G., Prost, J., The Physics of Liquid Crystals, Oxford Science Publishers: Oxford, 1974.

[22] Zhong, C., Wakayama, N.I., *Journal of Crystal Growth*, **226** (2-3), 327-332, 2001.

[23] Kimura, T., *Polymer Journal*, **35** (11), 823, 2003.

[24] Torbet, J., Ronziere, M.C., *Biochemical Journal*, **219** (3), 1057-1059, 1984.

[25] Christianen, P.C.M., Shklyarevskiy, I.O., Boamfa, M.I., Maan, J.C., *Physica B: Condensed Matter*, **346-347**, 255-261, 2004.

[26] Boamfa, M.I., Christianen, P.C.M., Engelkamp, H., Nolte, R.J.M., Maan, J.C., *Advanced Functional Materials*, **14** (3), 261-265, 2004.

[27] Schenning, A.P.H.J., Meijer, E.W., *Chemical Communications*, 3245-3258, 2005.

[28] Hill, J.P., Jin, W., Kosaka, A., Fukushima, T., Ichihara, H., Shimomura, T., Ito, K., Hashizume, T., Ishii, N., Aida, T., *Science*, **304** (5676), 1481-1483, 2004.

[29] Terech, P., Weiss, R.G., *Chemical Reviews*, **97** (8), 3133-3160, 1997.

[30] Shklyarevskiy, I.O., Jonkheijm, P., Christianen, P.C.M., Schenning, A.P.H.J., Del Guerzo, A., Desvergne, J.P., Meijer, E.W., Maan, J.C., *Langmuir*, **21** (6), 2108-2112, 2005.

[31] Maret, G., Dransfeld, K., Biomolecules and Polymers in High Steady Magnetic Fields. In *Strong and Ultrastrong Magnetic Fields and Their Applications*, Herlach, F., Ed. Springer: New York, pp 143-204, 1985.

Chapter 2

Using magnetic birefringence to determine the molecular arrangement of supramolecular nanostructures

Abstract

Supramolecular aggregates can be aligned in solution using a magnetic field. Because of the optical anisotropy of the molecular building blocks, the alignment results in an anisotropic refractive index of the solution parallel and perpendicular to the magnetic field, which enables the determination of the molecular organization within supramolecular aggregates. This chapter describes a model for calculating the magnetic birefringence, using solely the magnetic susceptibilities and optical polarizabilities of the molecules, for any molecular arrangement.

Part of this work has been published in:
Gielen, J.C., Shklyarevskiy, I.O., Schenning, A.P.H.J., Christianen, P.C.M., Maan, J.C., *Science and Technology of Advanced Materials*, **10** (1), 014601, 2009.

Introduction

To gain a better understanding of the self-assembly process, it is important to develop methods by which the molecular arrangement within aggregates can be resolved, preferably in solution. The molecular arrangement is usually determined on a substrate in the solid state, which has the drawback that the molecular structure might be influenced by the underlying substrate or by drying effects of the evaporating solvent [1]. Here, we describe a method to determine the molecular structure in solution using magnetic birefringence. Our method makes use of the fact that the organic molecules used for self-assembly are anisotropic, to achieve directionality in the intermolecular non-covalent interactions [2]. Consequently, the magnetic and optical properties of the molecules are also anisotropic, which enables the magnetic alignment of aggregates, and the measurement of this alignment using birefringence. This chapter describes a model that relates the magnetic birefringence to the molecular structure and shape of the aggregates.

The model is an alternative formulation of Levy's method [3], and describes the magnetic anisotropy in the refractive index of an aggregate solution, accounting for both the form birefringence caused by an anisotropic aggregate shape, as well as the intrinsic birefringence due to anisotropic optical polarizabilities. The only input parameters of our model are the molecular magnetic susceptibility and optical polarizability tensors, as opposed to Levy's model in which the anisotropic refractive index is described in terms of the anisotropic refractive indices of the objects in the mixture. Although the refractive index and the polarizability of an aggregate are related through density, the relationship between the aggregate volume and the number of molecules involved is not always unambiguous, particularly for small aggregates. It is, therefore more convenient to express the refractive index of the mixture in terms of molecular polarizabilities, which are often available in literature and can be readily calculated.

Molecule in a magnetic field

The magnetic moment induced in a molecule in an applied magnetic field depends on the molar magnetic susceptibility $\tilde{\chi}$:

$$\tilde{\chi} = \begin{pmatrix} \chi_{x'x'} & 0 & 0 \\ 0 & \chi_{y'y'} & 0 \\ 0 & 0 & \chi_{z'z'} \end{pmatrix}, \tag{2.1}$$

where the x', y' and z'-axes are the principle axes of the molecule (Figure 2.1).

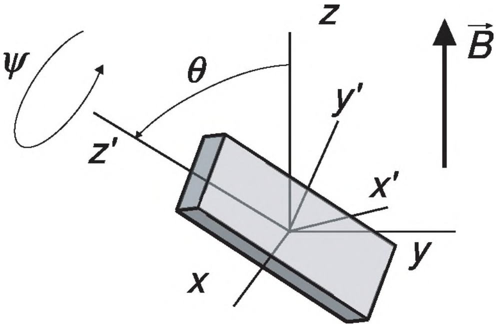

Figure 2.1: *Schematic representation of a molecule in a magnetic field. The (x',y',z') axes represent the principle molecular axes which are rotated over the Euler angles θ and ψ with respect to the lab axes (x,y,z). The magnetic field $\vec{B}$ is directed along the z-axis.*

In general, the diamagnetic susceptibility of an organic molecule is given by the sum of all contributions of the different chemical groups [4]. Since the susceptibility of most chemical groups is known, it is relatively straightforward to calculate the susceptibility of the molecular building blocks. Values of frequently occurring chemical groups are given in Table 2.1, an extensive table can be found in reference [5].

In an external magnetic field B, the induced magnetic moment is

$$\vec{m} = \frac{1}{\mu_0 N_a} \tilde{\chi} \cdot \vec{B}, \tag{2.2}$$

with μ_0 being the permeability of free space and N_a the Avogadro's number. The energy related to the induced moment is given by

$$E = -\int_0^B \vec{m} \cdot d\vec{B}. \tag{2.3}$$

For anisotropic molecules, E depends on the orientation of the molecules with respect to the magnetic field direction.

The magnetic field vector, which is in the positive z-direction, can be transformed to the molecular frame using the Euler transformation matrix [6]. In the molecular frame, $\vec{B}$ is then given by

$$\vec{B} = \begin{pmatrix} B\sin(\psi)\sin(\theta) \\ B\cos(\psi)\sin(\theta) \\ B\cos(\theta) \end{pmatrix}. \tag{2.4}$$

	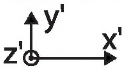 10^{-12} m^3/mol			
Bond/Molecule	$\chi_{x'x'}$	$\chi_{y'y'}$	$\chi_{z'z'}$	*Ref.*
C-C	$\chi_{x'x'}$	$\chi_{x'x'}$+16	$\chi_{x'x'}$+16	[4]
C=C	$\chi_{x'x'}$	$\chi_{x'x'}$-103	$\chi_{x'x'}$-103	[4]
C≡C	$\chi_{x'x'}$	$\chi_{x'x'}$-465	$\chi_{x'x'}$-465	[4]
C=O	$\chi_{x'x'}$	$\chi_{x'x'}$-83	$\chi_{x'x'}$-83	[4]
Benzene	-439	-439	-1189	[5]
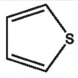	$\chi_{x'x'}$	$\chi_{x'x'}$+4.19	$\chi_{x'x'}$-627	[5]
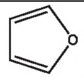	$\chi_{x'x'}$	$\chi_{x'x'}$-36.0	$\chi_{x'x'}$-504	[5]
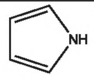	$\chi_{x'x'}$	$\chi_{x'x'}$-65.3	$\chi_{x'x'}$-565	[5]
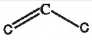	$\chi_{x'x'}$	$\chi_{x'x'}$+59	$\chi_{x'x'}$-50	[5]
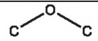	$\chi_{x'x'}$	$\chi_{x'x'}$+49	$\chi_{x'x'}$+82	[5]
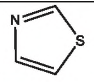	-451	-466	-1056	[5]

Table 2.1: *Experimental principle diamagnetic susceptibilities for the chemical groups needed for the supramolecular aggregates described in this thesis. When only the anisotropy is reported in literature, $\chi_{y'y'}$ and $\chi_{z'z'}$ are expressed in terms of $\chi_{x'x'}$.*

This leads to an expression of the increase in energy due to the magnetic field ΔE as a function of the Euler angles θ and ψ (omitting the terms independent of the molecular orientation)

$$\Delta E = -\frac{B^2}{2\mu_0 N_a}\left[(\chi_{x'x'} - \chi_{y'y'})\sin^2(\psi)\sin^2(\theta) + (\chi_{z'z'} - \chi_{y'y'})\cos^2(\theta)\right] . \quad (2.5)$$

Note that the Euler rotation described by the angle ϕ represents a rotation about the magnetic field axis, that does not affect the magnetic energy of the molecule.

For individual molecules, ΔE is typically very small compared with the thermal energy $k_b T$, and therefore it is not possible to align individual molecules with the static magnetic fields that are currently available (30-45 T). However, for an aggregate consisting of N molecules, the torque on the aggregate can be large enough to overcome the thermal randomization when $N\Delta E(\theta,\phi) \geq k_b T$. In such a case the degree of alignment is determined by a Boltzmann distribution function $f(\theta,\psi)$

$$f(\theta,\psi) = e^{-\frac{N\Delta E(\theta,\psi)}{k_b T}}. \tag{2.6}$$

For ΔE to be comparable to $k_b T$ (with $B = 20$ T and $T = 293$ K, then $k_b T \approx 0.03$ eV and $\Delta E \approx 10^{-6}$ eV per molecule), roughly 10^4 to 10^5 molecules are needed in an aggregate, for a typical molecule consisting of 4 planar phenyl rings ($\Delta\chi = \chi_{z'z'}$-$\chi_{x'x'}$=-3000·10^{-12} m^3/mol).

Shape anisotropy

In addition to the magnetic alignment due to the anisotropy in the magnetic susceptibility, an alternative alignment mechanism exists for large aggregates of anisotropic shape, due to the demagnetization [7]. When a cylindrically symmetric object with isotropic susceptibility $\bar{\chi}$ is placed in a magnetic field $\vec{H}$, a magnetization $\vec{M}$ is induced. At the outer edges of the object, fictuous surface "poles" are formed (see Figure 2.2) producing an internal demagnetizing field $\vec{H}_d$ directed opposite to the magnetization. The demagnetizing field is related to the magnetization via the dimensionless demagnetizing factor D

$$\vec{H}_d = -D\vec{M}. \tag{2.7}$$

The demagnetization causes the object to feel an apparent field $\vec{H}_{app}$

$$\vec{M} = \bar{\chi}\vec{H}_{app} = \bar{\chi}(\vec{H} - D\vec{M}), \tag{2.8}$$

which can be rewritten as

$$\vec{M} = \frac{\bar{\chi}}{1 + D\bar{\chi}}\vec{H} = \chi_{app}\vec{H}. \tag{2.9}$$

For objects embedded in a medium with susceptibility χ_m, the apparent susceptibility χ_{app} becomes [8]

$$\chi_{app} = \frac{1}{\frac{1+\chi_m}{\bar{\chi}-\chi_m} + D} \qquad \text{or} \qquad \chi_{app} = \frac{\bar{\mu} - \mu_m}{\mu_m + D(\bar{\mu} - \mu_m)}, \tag{2.10}$$

when written in terms of permeabilities $\mu_m = \mu_0(1 + \chi_m)$ and $\bar{\mu} = \mu_0(1 + \bar{\chi})$. The susceptibility of the solvent is typically 1 to 2 orders of magnitude smaller than the susceptibility of a supramolecular aggregate.

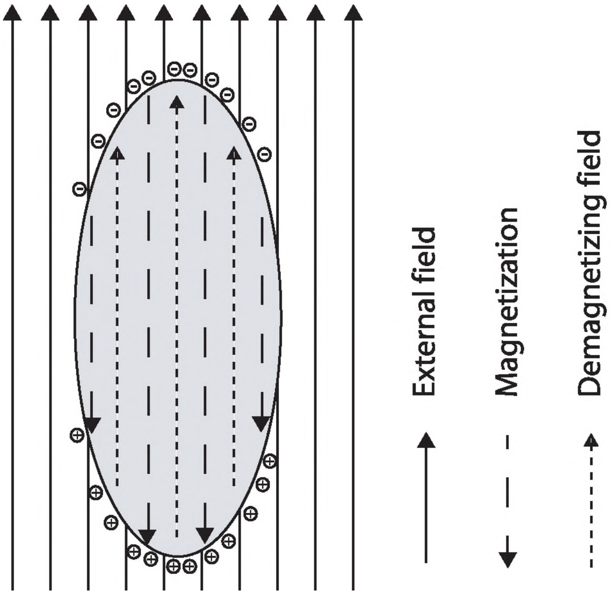

Figure 2.2: *The demagnetizing field for a diamagnetic object oriented with the long axis along the magnetic field. The fictitious surface poles are drawn at the boundaries.*

The demagnetizing factor is a purely geometrical factor, which is different along different axes of the object ($D_{\|}$ along the long axis and $D_{\perp}$ along the short axis), resulting in an apparent anisotropic susceptibility

$$\Delta\chi = \chi_{app,\|} - \chi_{app,\perp} = \frac{\bar{\chi}}{1 + D_{\|}\bar{\chi}} - \frac{\bar{\chi}}{1 + D_{\perp}\bar{\chi}}. \tag{2.11}$$

For ellipsoidally shaped objects, the demagnetizing factor can be calculated analytically [9]. Table 2.2 lists some depolarizing factors for limiting situations. For non-ellipsoidal objects the depolarizing factors need to be calculated numerically.

The anisotropy caused by the demagnetization can induce alignment of large aggregates. However, the energy involved in this process is typically much smaller than the molecular ΔE of equation (2.5), and is therefore neglected for the supramolecular aggregates considered in this thesis. For example, for the case of the thiophene aggregates described in Chapter 4, the anisotropy caused by the demagnetization is four orders of magnitude smaller than the molecular anisotropy.

Object	*Demagnetizing factors*	
Sphere	$D_x = D_y = D_z = 1/3$	
Infinite cylinder	parallel to long axis perpendicular to long axis	$D_{\parallel} = 0$ $D_{\perp} = 0.5$
Infinite plane	parallel to the plane perpendicular to the plane	$D_{\parallel} = 0$ $D_{\perp} = 1$

Table 2.2: *Demagnetizing factors for some limiting configurations.*

Refractive index of aligned aggregates

The magnetic orientation of aggregates leads to a difference in the refractive index of the solution parallel and perpendicular to the magnetic field. We calculate this magnetic birefringence incorporating two contributions: the intrinsic birefringence due to the anisotropic molecular polarizability [10] and the form birefringence caused by an anisotropic aggregate shape [11]. In the following, we limit ourselves to aggregates that are small with respect to the wavelength of light, which allows us to use an electrostatic approximation. We consider the solution as a host dielectric with refractive index n_1 and we describe the aggregates as inclusions in this host medium. The electric field $\vec{E}_0$ applied over the overall system can be expressed in terms of the field $\vec{E}_s$ in the inclusions

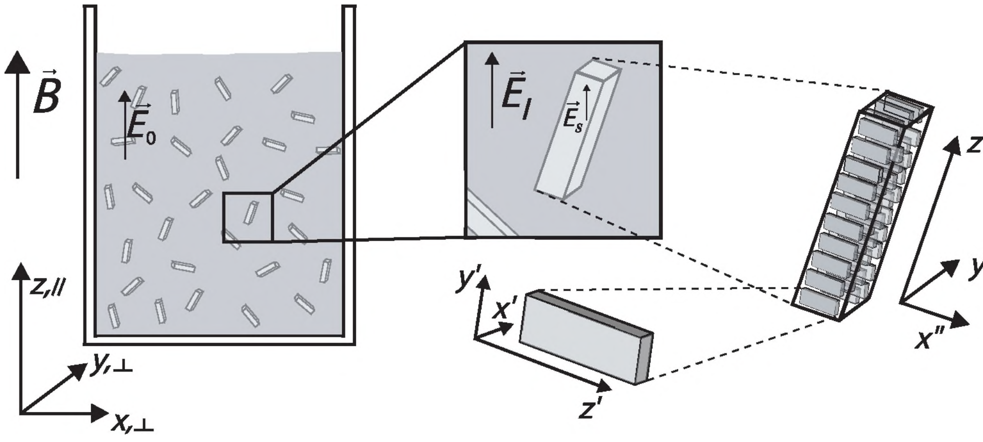

Figure 2.3: *Schematic representation of the aggregates and the electric fields in solution. The (x'', y'', z'') coordinate system represents the aggregate axes. The magnetic field $\vec{B}$ points in the z-direction*

and the field $\vec{E}_l$ in the host medium near a dielectric (Figure 2.3), using the effective medium theory [11]

$$f\left\langle\vec{E}_s\right\rangle+(1-f)\vec{E}_l=\vec{E}_0, \tag{2.12}$$

where f is the volume fraction of the aggregates, and the brackets $< \ldots >$ denote an orientational average.

Similar to the depolarizing field, the effective electric field within the aggregate is lower than the field outside because of the form birefringence: the induced surface charges at an anisotropically shaped object reduce the electric field inhomogeneously. The shorter the aggregate is along a certain direction, the more the field will be reduced. The reduction $\tilde{\kappa}$ describes the ratio between the field inside and outside the inclusion as $\vec{E}_s=\tilde{\kappa}\vec{E}_l$,with

$$\tilde{\kappa}=\begin{pmatrix}\kappa_{a,x''x''} & 0 & 0\\ 0 & \kappa_{a,y''y''} & 0\\ 0 & 0 & \kappa_{a,z''z''}\end{pmatrix} \tag{2.13}$$

and

$$\kappa_{a,ii}=\frac{n_1^2}{d_{a,ii}n_f^2+(1-d_{a,ii})n_1^2}\quad,\qquad i=x'',y'',z'' \tag{2.14}$$

where $d_{a,ii}$ represents the depolarizing coefficients along the different aggregate axes (the axes with double prime indicate the principle axes of the aggregate), and n_f is the average refractive index of the aggregate. Since the form birefringence is usually a small effect, a typical refractive index for conjugated organic molecules of $n_f \approx 1.6-1.7$ [12] [13] can be used without the need to calculate the exact refractive index for the aggregate configuration. The depolarizing coefficients are equal to the demagnetizing factors (Table 2.2).

Equation (2.12) can be rewritten as

$$\vec{E}_l=\frac{\vec{E}_0}{(1-f)+f\langle\tilde{\kappa}\rangle}. \tag{2.15}$$

The denominator term accounts for the influence of an aggregate on the electric field experienced by the other aggregates. If $n_f>n_1$, the denominator term is larger than unity, and the effective field experienced by the aggregates is reduced.

The intrinsic birefringence is described in terms of the aggregate polarizability

$$\tilde{\alpha}=\begin{pmatrix}\alpha_{x''x''} & 0 & 0\\ 0 & \alpha_{y''y''} & 0\\ 0 & 0 & \alpha_{a,z''z''}\end{pmatrix}, \tag{2.16}$$

where $\alpha_{i''i''}$ is the polarizability along the principle axes of the aggregate and is obtained by spatial averaging of the molecular polarizabilities $\alpha_{i'i'}$ over the orientations of the molecules within the aggregate. The magnetic susceptibility of the aggregate $\chi_{i''i''}$ is obtained in a similar fashion.

The dipole moment induced in the aggregate is then

$$\vec{p}_s = \frac{\tilde{\kappa}\tilde{\alpha}\vec{E}_0}{(1-f)+f\langle\tilde{\kappa}\rangle}. \tag{2.17}$$

Since the relation between the applied electric field, the electric displacement $\vec{D}$ and the polarization $\vec{P}$ is given by $<\vec{D}>= n_1^2\vec{E}_0+<\vec{P}>=\epsilon_m\vec{E}_0$, we find, for the dielectric constant of the mixture,

$$\epsilon_m = n_1^2\tilde{I} + \frac{n_1^2 N_{pcm} < \tilde{\kappa}\tilde{\alpha} >}{(1-f)+f\langle\tilde{\kappa}\rangle}, \tag{2.18}$$

with $\tilde{I}$ the identity matrix. This tensor expression for the dielectric constant contains three diagonal components: $\epsilon_{m,zz}$ parallel to the magnetic field direction, and $\epsilon_{m,xx} = \epsilon_{m,yy}$ perpendicular to the magnetic field direction. It includes both the form birefringence via $\tilde{\kappa}$ and the molecular polarizabilities $\tilde{\alpha}$, and also accounts for the fact that the effective electric field is reduced owing to the presence of the aggregates.

The actual magnetic birefringence is now given by the difference of the refractive indices parallel and perpendicular to the magnetic field direction

$$\begin{aligned} \Delta n &= n_{\|,B} - n_{\perp,B} \qquad (2.19) \\ &= \frac{\int_0^{2\pi}\int_0^{\pi}(\sqrt{\epsilon_{m,zz}}-\sqrt{\epsilon_{m,xx}})f(\theta,\psi)\sin(\theta)d\theta d\psi}{\int_0^{2\pi}\int_0^{\pi} f(\theta,\psi)\sin(\theta)d\theta d\psi}. \qquad (2.20) \end{aligned}$$

Theoretical examples

We illustrate the role of the two components of the birefringence, the form and the intrinsic birefringence, by two theoretical examples. In the first case, we consider a cylindrically symmetric situation where $\chi_{x''x''} = \chi_{y''y''} \ll \chi_{z''z''}$ and $\alpha_{x''x''} = \alpha_{y''y''} < \alpha_{z''z''}$, and we apply these parameters respectively to a cylindrical aggregate, a spherical aggregate and a disc-shaped aggregate. Figure 2.4 shows the resulting birefringence together with a schematic picture of the aggregate in the high-field-limit orientation. In this situation, the aggregates align with their z''-axis, which is the axis of highest polarizability, parallel to the magnetic field. For the cylindrical aggregate, the birefringence is enhanced by the form birefringence compared with the spherical aggregate, since the effective polarizabilities $\alpha_{x''x''}$ and $\alpha_{y''y''}$ are reduced due to the depolarization effect. The disc-shaped aggregate exhibits a reduced value of the birefringence because, now, the polarizability $\alpha_{z''z''}$ along the symmetry axis is diminished by the form birefringence.

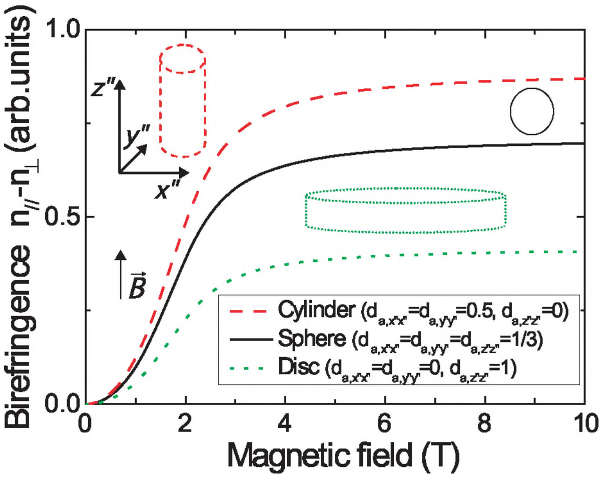

Figure 2.4: *Influence of the shape of the supramolecular aggregate on the magnetic field induced birefringence. The corresponding depolarizing coefficients $d_{a,i"i"}$ are given in the figure legend. The aggregate shapes are drawn schematically in the energetically most favourable orientation when the magnetic field points upwards. The parameters used for the calculations are* $\chi_{x''x''} = \chi_{y''y''} = 4\chi_{z''z''} = -4000 \times 10^{-12}$ *m*^{3}*mol*$^{-1}$, $\alpha_{x''x''} = \alpha_{y''y''} = 0.5\alpha_{z''z''} =$ *200 au, C=10*$^{-3}$ *M, f=10*$^{-4}$, $n_1 = 1.4$, $n_f = 1.6$, $N = 2 \times 10^6$ *and T = 293 K.*

To illustrate the intrinsic birefringence, we consider disc-shaped aggregates composed of molecules with susceptibilities $\chi_{x'x'}$, $\chi_{y'y'}$ and $\chi_{z'z'}$ and polarizabilities $\alpha_{x'x'}$, $\alpha_{y'y'}$ and $\alpha_{z'z'}$ using typical parameters for π-conjugated oligomer molecules: $\chi_{x'x'} \approx \chi_{y'y'} >> \chi_{z'z'}$ and $\alpha_{x'x'} > \alpha_{y'y'} > \alpha_{z'z'}$. The magnetic birefringence depends on the way the molecules are oriented within the aggregates. Figure 2.5 shows three simple configurations: a linear arrangement (top right panel, red solid line), a radial arrangement (middle right panel, green dashed line) and a herringbone arrangement (bottom right panel, blue dotted line). Because of the molecular orientation within the aggregate, we find $\alpha_{x''x''} = \alpha_{y''y''} = 0.5\alpha_{y'y'} + 0.5\alpha_{z'z'}$ and $\alpha_{z''z''} = \alpha_{x'x'}$ for the linear configuration, $\alpha_{x''x''} = \alpha_{y''y''} = 0.5\alpha_{x'x'} + 0.5\alpha_{z'z'}$ and $\alpha_{z''z''} = \alpha_{y'y'}$ for the radial configuration, and $\alpha_{x''x''} = \alpha_{z'z'}\cos^2(\eta) + \alpha_{x'x'}\sin^2(\eta)$, $\alpha_{y''y''} = \alpha_{z'z'}\sin^2(\eta) + \alpha_{x'x'}\cos^2(\eta)$ and $\alpha_{z''z''} = \alpha_{y'y'}$ for the herringbone configuration, where η is the herringbone angle of the molecules with the y''-axis. For the aggregate susceptibilities $\chi_{i''i''}$ we find similar expressions in terms of molecular susceptibilities $\chi_{i'i'}$. All three configurations align with their symmetry axis along the magnetic field, with the molecular z'-axis perpendicular to the magnetic field. For the linear configuration, we find a positive birefringence because the molecules align with their highest polarizability axis (x') parallel to the magnetic field. For the radial arrangement, the molecular y'-axis is parallel to the magnetic field, resulting in a negative birefringence. The absolute value of the birefringence is lower than that in the linear case because the molecular x'-axis is allowed to rotate about the magnetic field axis. The herringbone arrangement results in a two-step alignment process that gives rise to the peculiar

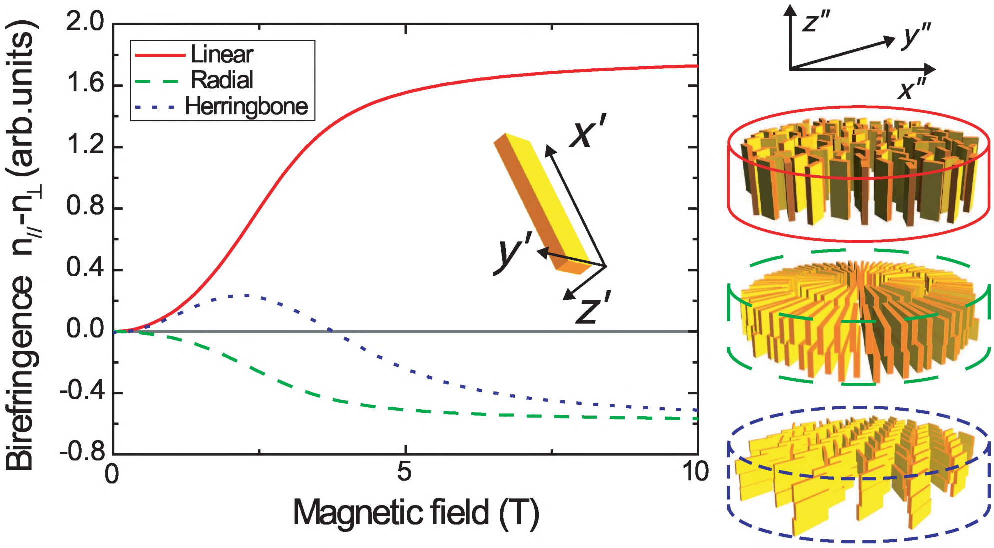

Figure 2.5: *Theoretical magnetic birefringence curves for disc shaped aggregates. Both the shape of the curve and the saturation value strongly depend on the molecular orientation within the aggregate. The three situations correspond to a linear (solid red line), radial (dashed green line) and herringbone (dotted blue line) arrangement perspectively. The parameters used for the calculations are* $\chi_{x'x'} = \chi_{y'y'} = -1000 \times 10^{-12}$ *m*^{3}*mol*$^{-1}$, $\chi_{z'z'} = -4000 \times 10^{-12}$ *m*^{3}*mol*$^{-1}$, $\alpha_{x'x'}$ *=700 au,* $\alpha_{y'y'}$*=400 au,* $\alpha_{z'z'}$ *=100 au,* C*=10*$^{-3}$ *M,* f*=10*$^{-4}$, n_1*=1.4,* n_f*=1.6,* $N = 2 \times 10^6$, d_{xx}*=*d_{yy}*=0,* d_{zz}*=1,* T*=293 K and herringbone angle* η*=65 degrees.*

shape of the birefringence curve. In high fields, the birefringence is equal to the radial aggregate, because, in both cases, the molecules align with the y'-axis parallel to the magnetic field. However, the initial birefringence is positive since the orientation with the x''-axis parallel to the magnetic field is slightly more favorable than the y''-axis being parallel to B. This two step alignment process is caused by an anisotropy in the magnetic susceptibility along the x''-axis and y''-axis, and clearly demonstrates the high sensitivity of magnetic birefringence for the internal molecular arrangement of supramolecular aggregates.

Experimental example

We have recently reported the formation of spherical structures built of α,α'-linked sexithiophene (**T6**) molecules with chiral oligo(ethyleneoxide) side chains (see also Chapter 4) [14]. The spherical aggregates were prepared by solving **T6** molecules in tetrahydrofuran, and subsequent injection into isopropanol. It was found that changing the solvent from isopropanol to decanol while keep-

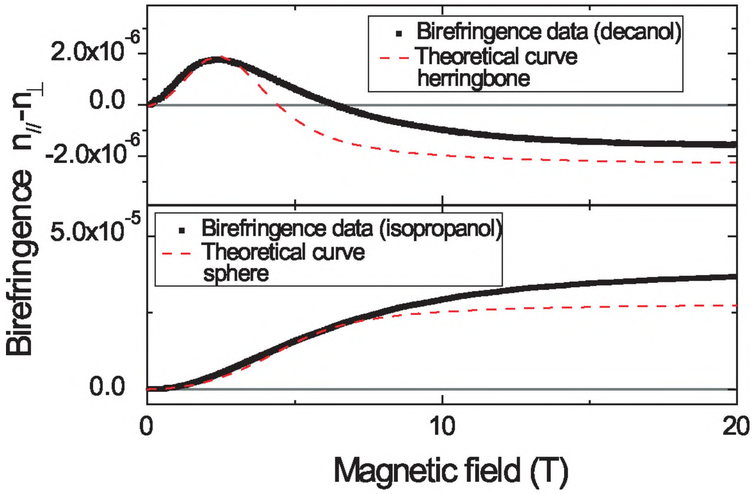

Figure 2.6: *Magnetic field induced birefringence of* ***T6*** *aggregates and the theoretical prediction for two different solvents. The difference in alignment indicates a different internal molecular arrangement. The parameters used for the calculations are* $\chi_{x'x'} = \chi_{x'x'} = -3063 \times 10^{-12}$ $m^3 mol^{-1}$, $\chi_{x'x'} = -6813 \times 10^{-12}$ $m^3 mol^{-1}$, $\alpha_{x'x'}$ *=772 au,* $\alpha_{y'y'}$ *=313 au,* $\alpha_{z'z'}$ *=93 au,* C=8.24×10^{-4} *M,* f=4.3×10^{-4}, n_1=1.4, n_f=1.6, $N_{isopropanol}$=5×10^5 , $N_{decanol}$=1.5×10^5, T=293 *K and herringbone angle* η=62°.

ing all other experimental conditions the same greatly influenced the shape, size and sign of the magnetic birefringence curves (Figure 2.6). These results suggest that the internal structure of the aggregates strongly depends on the solvent. The birefringence signal of the **T6**/isopropanol solution is very large and positive, whereas the **T6**/decanol exhibits a very small signal that changes from positive to negative at around a magnetic field strength of $B = 3$ T.

It is beyond the scope of this chapter to include elasticity in the calculation for the birefringence of the spherical aggregates in isopropanol [15]. Instead, we approximate the maximum birefringence for this case by assuming that all **T6** molecules are oriented with their long axis parallel to the magnetic field. This corresponds to the limiting situation of a completely deformed sphere. In this case, we find the maximum calculated birefringence of 3×10^{-5} at 20T, which is close to the experimental value of 3.7×10^{-5}, when using diamagnetic susceptibilities from the addition scheme [5] and the polarizabilities given by Champagne et al [16]. As was shown before, a birefringence signal that changes sign, as was observed for the decanol solution, only occurs for a very specific combination of aggregate polarizabilities and susceptibilities (Figure 2.6). The measured birefringence is well described by a herringbone structure in a cylindrical aggregate, which is probably the most widely encountered structure for linear conjugated oligomers [17]. Additional experiments are required to verify the internal structure, but the birefringence results can exclude many possible configurations and puts serious constraints on the structure.

Approximation for a low degree of alignment

For low magnetic fields or small aggregates, the birefringence depends quadratically on the magnetic field. In the case of a saturating birefringence, the size of the aggregates can easily be obtained by fitting the shape of the curve. In the quadratic regime, we have to rely on the actual value of the birefringence to obtain the aggregate size. To this end, the assumption is made that there are two populations: a number of molecules per unit volume $N_{pcm}(T)$ is incorporated in aggregates with one specific size N, the rest of the molecules is molecularly dissolved and their contribution to the birefringence can be neglected. Using two Taylor expansions to approximate equation (2.20) ($e^x \approx 1 + x$ and $\sqrt{1+x} \approx 1 + \frac{1}{2}x$), the birefringence can be written as

$$\begin{aligned}
\Delta n &\approx \frac{n_1 N_{pcm}(T) N B^2}{60 \mu_0 N_a k_b T} \left[\alpha_{x''x''} \kappa_{x''x''} \left(2\chi_{x''x''} - \chi_{y''y''} - \chi_{z''z''} \right) + \right. && (2.21) \\
&+ \alpha_{y''y''} \kappa_{y''y''} \left(2\chi_{y''y''} - \chi_{z''z''} - \chi_{x''x''} \right) && (2.22) \\
&+ \left. \alpha_{z''z''} \kappa_{z''z''} \left(2\chi_{z''z''} - \chi_{x''x''} - \chi_{y''y''} \right) \right] . && (2.23)
\end{aligned}$$

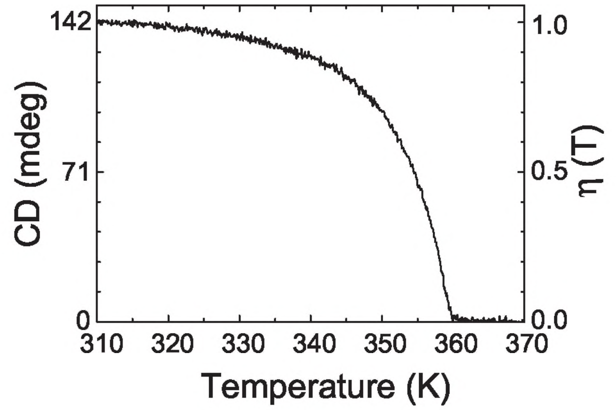

Figure 2.7: *Temperature dependent CD signal, measured at* $\lambda = 400$ *nm, of a 1 mg/ml OPV4 solution in dodecane (see Chapter 6). The left axis shows the value of the CD signal, the right axis the fraction of molecules incorporated in an aggregate.*

For cylinder-symmetric aggregates, this expression further simplifies to:

$$\Delta n \approx \frac{n_1 N_{pcm}(T) N B^2 \Delta\alpha \Delta\chi}{30 \mu_0 N_a k_b T} \tag{2.24}$$

where $\Delta\alpha = \kappa_{\|}\alpha_{\|} - \kappa_{\perp}\alpha_{\perp}$ and $\Delta\chi = \chi_{\|} - \chi_{\perp}$. This expression relates the birefringence to the aggregate size in the case of small aggregtes or low magnetic field strengths. Equation (2.24) shows that the birefringence is proportional to the number of molecules per unit volume in the aggregated state. When all molecules are incorporated in aggregates, N_{pcm} is equal to the concentration. However, in a temperature dependent experiment, this is usually not the case for all temperatures. It is then required to measure $N_{pcm}(T)$ to interpret the birefringence measurements.

For chiral supramolecular aggregates, circular dichroism (CD) is the most convenient method. CD is the difference in absorption of left- and right handed circularly polarized light. At the wavelength of aggregate absorption, individual monomers do not show a CD effect, only molecules in aggregates contribute to the CD signal. A typical temperature dependent CD signal is shown in Figure 2.7. Multiplying $\eta(T)$ with the concentration yields $N_{pcm}(T)$, which leaves the aggregate size N as the only fitting parameter for the birefringence data. For non-chiral molecules one has to rely on the changes in the UV/vis absorbance spectrum. However, monomers typically have a non-zero absorbance at the monitored wavelength, making this technique less accurate than the CD method.

Flexible aggregates

The theory so far is about rigid aggregates. Flexible aggregates, however, appear shorter in a birefringence measurement than they really are. The extent of this shortening depends on the ratio between the aggregate length L and the persistence length l_p. In the quadratic regime ($\Delta n \propto B^2$) the relation between the measured birefringence Δn and the birefringence of a rigid rod Δn_{rigid} is given by [18]

$$\Delta n = \Delta n_{rigid} \times \frac{2}{9}\left[\frac{3l_p}{L} - \frac{l_p^2}{L^2}\left(1 - \exp\left(-\frac{3L}{l_p}\right)\right)\right]. \tag{2.25}$$

The bracketed term tends to $\frac{3l_p}{L}$ for $L \gg l_p$, and $\Delta n_{rigid} \propto L$ for a rigid linear aggregate, which means that the maximum observed aggregate size is $\frac{2}{3}$ of the persistence length. After the quadratic regime, the field is strong enough to deform the flexible chain, and the equation no longer holds.

Experimental setup

Figure 2.8 shows the setup used to measure the magnetic field induced birefringence. The cuvet with the solution to be measured is placed between crossed polarizers oriented at $\pm 45^o$ with respect to the magnetic field. Monochromatic light is produced by a HeNe laser (Melles Griot, 1mW output, λ=632.8 nm), modulated by a photo-elastic modulator (PEM, PEM-90 Hinds Instruments) with a frequency $f = \Omega/2\pi$ = 50kHz and a maximum retardation of A_0=0.383 waves. The light transmitted through the second polarizer is guided with an optical fiber (Thorlabs, multimode fiber) to a photodetector (Thorlabs, PDA55). This setup measures the retardation δ rather than the birefringence Δn, that are related through the relation

$$\delta = \frac{2\pi d \Delta n}{\lambda}, \tag{2.26}$$

where d is the cuvet thickness. The output intensity seen by the detector is given by [19]

$$I(t) \propto 1 - \cos(\delta)\cos(A_0\cos(\Omega t)) + \sin(\delta)\sin(A_0\cos(\Omega t)). \tag{2.27}$$

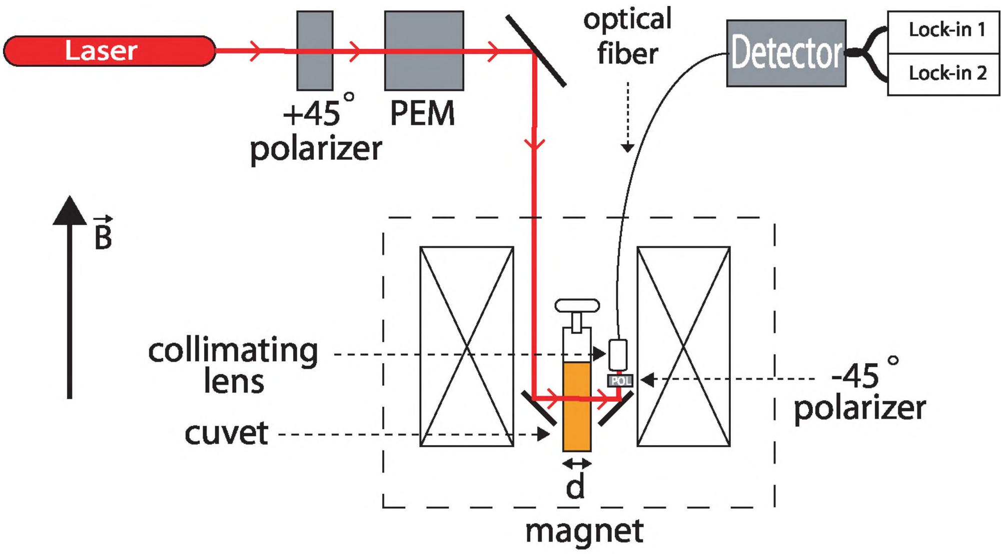

Figure 2.8: *Schematic representation of the setup to measure magnetic field induced birefringence inside a 20T bitter magnet. The arrow indicates the magnetic field direction. The thickness of the cuvet is indicated by d.*

A Fourier series expansion gives

$$I(t) \approx \underbrace{1-\cos(\delta)J_0(A_0)}_{V_{DC}} + \underbrace{2\sin(\delta)J_1(A_0)}_{V_{1f}}\cos(\Omega t) + \underbrace{2\cos(\delta)J_2(A_0)}_{V_{2f}}\cos(2\Omega t) + \dots, \tag{2.28}$$

yielding three terms: a DC-term and a first and second harmonic term. The retardation of the PEM was chosen such that $J_0(A_0) = 0$ to make the DC signal independent of the retardation. The retardation can then be obtained by dividing the second harmonic and the first harmonic amplitude with the proper scaling factors

$$\delta = \arctan\left(\frac{J_2(A_0)V_{1f}}{J_1(A_0)V_{2f}}\right). \tag{2.29}$$

Even though the field dependent background birefringence with this setup, caused by the mirrors and windows, was relatively high (0.2 radians), the noise was relatively low (10^{-3} radians), yielding an experimental resolution of $\Delta n \sim 2 \times 10^{-8}$. The sign of the birefringence is also measured, yielding information on the molecular orientation within the magnetic field.

References

[1] Van Hameren, R., Schön, P., Van Buul, A.M., Hoogboom, J., Lazarenko, S.V., Gerritsen, J.W., Engelkamp, H., Christianen, P.C.M., Heus, H.A., Maan, J.C., Rasing, T., Speller, S., Rowan, A.E., Elemans, J.A.A.W., Nolte, R.J.M., *Science*, **314** (5804), 1433-1436, 2006.

[2] Hoeben, F.J.M., Jonkheijm, P., Meijer, E.W., Schenning, A.P.H.J., *Chemical Reviews*, **105** (4), 1491-1546, 2005.

[3] Levy, O., *Physical Review E*, **66** (1), 011404, 2002.

[4] Maret, G., Dransfeld, K., Biomolecules and Polymers in High Steady Magnetic Fields. In Strong and Ultrastrong Magnetic Fields and Their Applications, Herlach, F., Ed. Springer: New York, pp 143-204, 1985.

[5] Gupta, R.R., Diamagnetische Suszeptibilität (Landolt Börnstein. Gruppe II, Atom- und Molekularphysik vol. 16), Springer, Berlin, 1986.

[6] Goldstein, H., Poole, C., Safko, J., Classical Mechanics (3rd ed), Addison Wesley, Reading, 2002.

[7] Craig, D., Magnetism. Principles and Applications, Chichester, 1995.

[8] Svoboda, J., *Magnetic and electrical separation*, **4**, 223-239, 1993.

[9] Osborn, J.A., *Physical Review*, **67** (11-12), 351, 1945.

[10] Buckingham, A.D., Pople, J.A., *Proceedings of the Physical Society of London Section B*, **69** (11), 1133-1138, 1956.

[11] Bragg, W.L., Pippard, A.B., *Acta Crystallographica*, **6** (11-1), 865-867, 1953.

[12] Tammer, M., Monkman, A.P., *Advanced Materials*, **14** (3), 210-212, 2002.

[13] Takazawa, K., *Journal of Physical Chemistry C*, **111** (24), 8671-8676, 2007.

[14] Shklyarevskiy, I.O., Jonkheijm, P., Christianen, P.C.M., Schenning, A.P. H.J., Meijer, E.W., Henze, O., Kilbinger, A.F.M., Feast, W.J., Del Guerzo, A., Desvergne, J.P., Maan, J.C., *Journal of the American Chemical Society*, **127** (4), 1112-1113, 2005.

[15] Manyuhina, O.V., Shklyarevskiy, I.O., Jonkheijm, P., Christianen, P.C.M., Fasolino, A., Katsnelson, M.I., Schenning, A.P.H.J., Meijer, E.W., Henze, O., Kilbinger, A.F.M., Feast, W.J., Maan, J.C., *Physical Review Letters*, **98** (14), 146101-4, 2007.

[16] Champagne, B., Mosley, D.H., Andre, J.M., *Journal of Chemical Physics*, **100** (3), 2034-2043, 1994.

[17] Gavezzotti, A., Filippini, G., *Synthetic Metals*, **40** (2), 257-266, 1991.

[18] Appell, J., Porte, G., Poggi, Y., *Journal of Colloid and Interface Science*, **87** (2), 492-499, 1982.

[19] Kemp, J.C., Polarized light and its interaction with modulated devices - A Methodology review-, HINDS International, Inc.: Hillsboro, 1987.

Chapter 3

Light scattering of supramolecular aggregates in solution

Abstract

Laser light scattering provides a non-invasive technique to determine the size and shape of supramolecular aggregates in solution. This chapter describes the experimental setup and principles of static- and dynamic light scattering, together with some experimental examples. In a magnetic field, the orientational distribution function of the aggregates changes and thereby the diffusivity. We discuss the consequences of this, and show that this improves the accuracy of light scattering measurements in the case of anisotropically shaped aggregates.

Part of this work has been published in:
Jakobs, R.T.M., Van Herrikhuyzen, J., Gielen, J.C., Christianen, P.C.M., Meskers, S.C.J., Schenning, A.P.H.J., *J. Mat. Chem.*, **18** (29), 3438-3441,2008
Janssen, P.G.A., Jabbari-Farouji, S., Surin, M., Vila, X., Gielen, J.C., De Greef, T.F.A., Vos, M.R.J., Bomans, P.H.H., Sommerdijk, N.A.J.M., Christianen, P.C.M., Leclère, P., Lazzaroni, R., Van der Schoot, P., Meijer, E.W., Schenning, A.P.H.J., *J. Am. Chem. Soc.*, **131** (3), 1222-1231, 2009
Matmour, R., De Cat, I., George, S.J., Adriaens, W., Leclère, P., Bomans, P.H.H., Sommerdijk, N.A.J.M., Gielen, J.C., Christianen, P.C.M., Heldens, J.T., van Hest, J.C.M., Löwik, D.W.P.M., De Feyter, S., Meijer, E.W., Schenning, A.P.H.J., *J. Am. Chem. Soc.*, **130** (44), 14576-14583, 2008.

Introduction

When laser light passes through a solution with aggregates, most of the light is transmitted. In the previous chapter, we described how magnetic birefringence is measured by the polarization change of the transmitted light when the aggregates have a preferred orientation. However, a small part of the laser light is scattered, because of the different refractive indices of aggregates and solvent. The electric field of the laser induces an oscillating polarization, which then serves as a secondary source of light, causing the scattering. The angular dependence, the polarization and the intensity of the scattered light depend on the size, shape, orientation and relative positions of the aggregates. Therefore, light scattering provides a non-perturbative probe to obtain information on aggregates in solution. In this chapter, we shortly describe the basic principles of static- and dynamic light scattering, we give examples of light scattering experiments on supramolecular aggregates, and we discuss the possibility of increasing the accuracy of these methods using magnetic alignment.

Throughout this thesis, light scattering is mostly used as an additional technique. In Chapters 4 and 7 it is used in a qualitative manner, to determine the temperature range where aggregates are formed. The high concentrations there hinder the use of light scattering for size determination. In Chapter 6, DLS is used to measure the temperature dependent aggregate size quantitatively.

Experiment

The experimental setup to measure light scattering is schematically shown in Figure 3.1 (a). The laser light is brought to the scattering setup by an optical fiber, which enabled the use of different lasers without the need to re-align the setup. The fiber output is sent through a (vertically oriented) polarizer and focused into a cuvet with the aggregate solution, mounted in the scattering cell. The scattered light (vertically polarized) is collected by an optical fiber with a pigtail collimator lens, mounted on a rotator to vary the scattering angle θ. The fiber is connected to a single photon detector, to measure the number and arrival times of the scattered photons.

Figure 3.1 (b) shows a photo of the scattering cell. An insulated (white) bath is mounted on a z-stage, with the cuvet in the center. The bath is filled with a refractive index matching fluid (ethylene glycol) to prevent backscattering of the laser light at the cuvet wall. The movable detector arm with the polarizer and the detection fiber is shown on the right, the insulated tubes on the left are used for temperature control in the bath. A temperature sensor (not shown on the photo) is placed in the bath next to the cuvet.

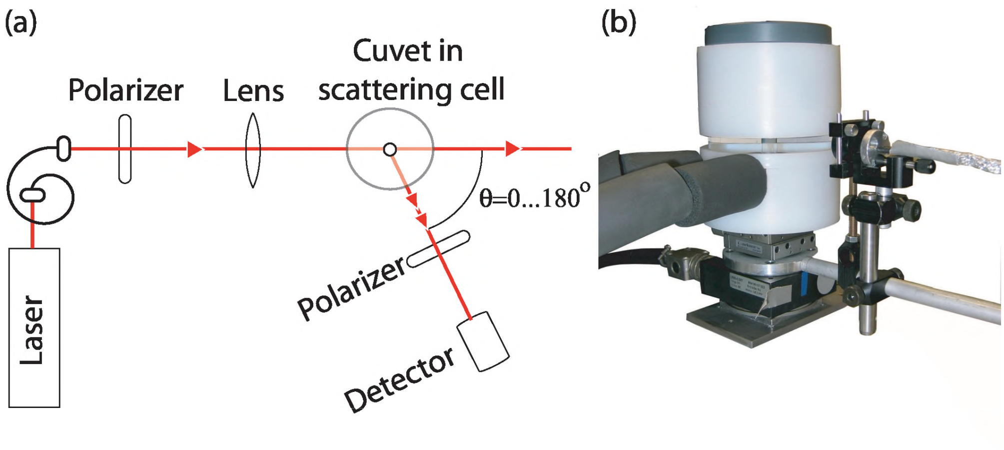

Figure 3.1: *(a) Schematic representation of the light scattering setup. The polarized light is focused into the cuvet, which is mounted in a scattering cell. The scattered light is detected at a range of angles. The polarization is in the direction perpendicular to the image plane. (b) Photo of the scattering cell. The cuvet is in the center of the white bath, surrounded by a refractive index matching fluid.*

For a successful measurement there are some important aspects in the sample preparation. First of all, the sample needs to be very *clean*. The slightest amount of impurities will hamper the measurement, especially when dust particles are involved, which are typically much larger than the aggregates under investigation. In some cases, solutions can be filtered using an HPLC PTFE syringe filter with a pore size of ~0.2-0.5 μm to remove impurities. The sample should not *absorb* at the laser frequency because of attenuation of the incident and scattered light and sample heating. Finally, the sample should not be *too concentrated*. The theory presented here assumes freely moving aggregates at low density. For higher concentrations, interactions between the aggregates will affect the scattering signal, multiple scattering may occur, and the presence of close neighboring particles can hinder a free movement [1].

Static light scattering (SLS)

In a static light scattering experiment, the angular dependence of the intensity of the scattered light is measured. For particles very small compared to the wavelength of light, the particles can be treated as single oscillating dipoles. The so called *Rayleigh regime* gives an accurate description as long as $a \ll \lambda/2\pi$ and $|m|a \ll \lambda/2\pi$, with a the particle size, $m = \frac{n_{particle}}{n_{solvent}}$ the relative refractive index of the particles in the solvent, and λ the wavelength of the laser light. For an incoming polarization perpendicular to the plane formed by the incident and scattered beam, the scattering intensity is constant for all observation angles. The intensity scales with the square of the particle volume, but is independent of the particle shape. Therefore, this regime is not very useful for measurements on the shape of aggregates.

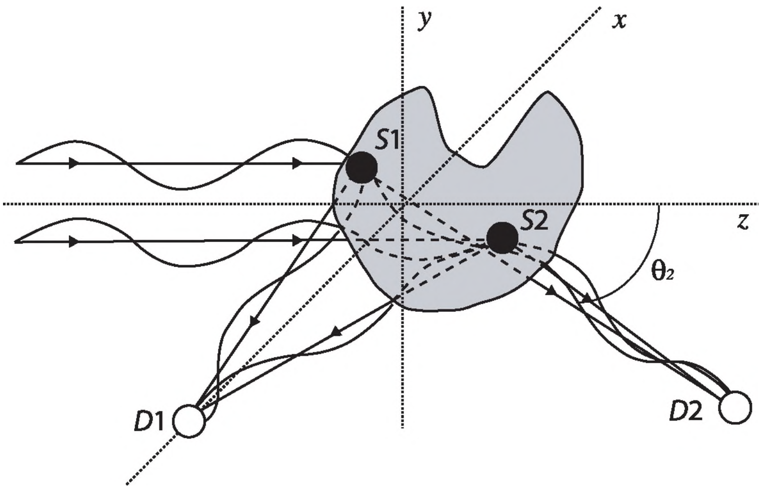

Figure 3.2: *Schematic representation showing the path difference for two scattering waves from points $S1$ and $S2$ (at arbitrary positions within the particle) for two detector positions $D1$ and $D2$, which are both in the xz-plane. The scattering angle θ is defined as the angle between the z-axis and the direction of the detector, as indicated by θ_2 for detector $D2$. θ_1 is equal to $\pi/2$ (not indicated in the figure). The polarization of the light is in the y-direction.*

For larger particles, the intraparticle interference introduces an angular dependence of the scattering intensity (*Rayleigh-Debye* regime). Figure 3.2 shows the incident and scattered light for a particle with an arbitrary shape. The

Shape	*Form factor*
Solid sphere $X = kR$	$P(X) = \left[\frac{3}{X^3}\left(\sin(X) - X\cos(X)\right)\right]^2$
Cylinder $X = kL\cos(\beta)$ $Y = kR\sin(\beta)$	$P(kL) = \int_0^{\pi/2} \frac{\pi}{X}\left[\frac{2J_{\frac{1}{2}}(X/2)J_1(Y)}{Y}\right]^2 \sin(\beta)d\beta$
Disc $X = kR$	$P(X) = \frac{2}{X^2}\left[1 - \frac{1}{X}J_1(2X)\right]$

Table 3.1: *Form factor for different particle shapes. R is the radius and L the length of the particle [2–4] .*

particle can be divided into fictitious small volume elements (like $S1$ and $S2$), which are polarized by the incident light, making the particle behave like a collection of oscillating dipoles. The light observed by the detector is the sum of the contributions from the individual volume elements. The radiation from each volume element has a different phase, making the intensity seen by the detector (looking at angle θ) depend on the shape and size of the particle.

The angular dependence of the scattering intensity is contained in the form factor $P(k)$, where k $= |\vec{k}| = \frac{4\pi n_{solvent}}{\lambda}\sin(\frac{\theta}{2})$ is the scattering vector. $P(k)$ can be calculated analytically for some particle shapes using the Rayleigh-Debye approach, which is valid as long as $4\pi a(m-1)/\lambda \ll 1$ and $|m-1| \ll 1$. The contributions of the volume elements are summed and averaged over all orientations of the particle

$$P(k) = \left\langle \frac{1}{V_p} \int \exp(i\vec{k} \cdot \vec{r'})dV_p \right\rangle_{orientations} \quad , \tag{3.1}$$

where $\vec{r'}$ is the vector to the volume element within the particle, and V_p the particle volume. Table 3.1 gives form factors for frequently occurring particle shapes. An extensive list can be found in reference [3].

Figure 3.3 shows the form factor for three spherical particles of different size and a cylindrical particle as a function of the scattering vector. For a small particle like the R = 10 nm sphere, which falls within the Rayleigh regime, the scattered intensity is almost independent of the scattering vector. For larger particles, there is an angular dependence, with a strong scattering in the forward direction where θ and $|\vec{k}|$ are small. For such particles, static light scattering can be a useful tool to determine the particle shape and size. For particles too large for the Rayleigh-Debye approach, the angular dependence of the scattering intensity can only be calculated analytically for spherical particles (using Mie-theory). For other shapes, numerical techniques have to be used [5].

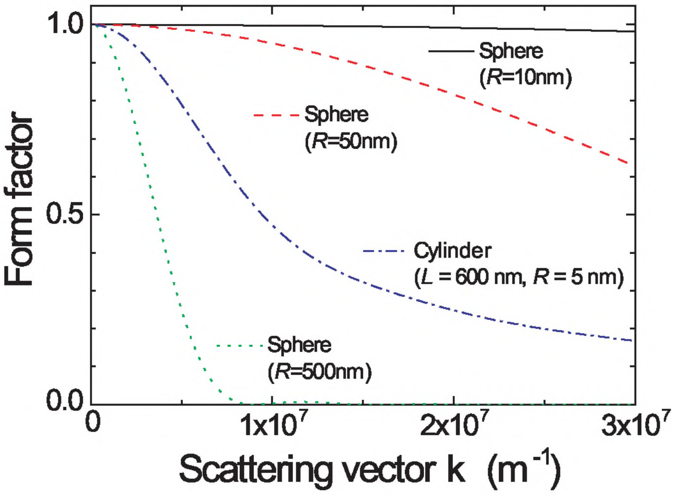

Figure 3.3: *Form factors for particles of different shapes and sizes. Three different spherical particles (R=10nm, solid black line, R=50nm, dashed red line, R=500nm, dotted green line), and a cylindrical particle (L=600nm, R=5 nm, dash-dotted blue line).*

Dynamic light scattering (DLS)

The time averaged scattering intensity for a solution of monodisperse particles is given by the form factor. However, the instantaneous intensity fluctuates due to interference between the scattering of different particles within the scattering volume, that move with respect to each other because of Brownian motion (schematically shown in Figure 3.4). When the particle with index j moves, the phase of the scattered light from that particle $\phi_j = \vec{k} \cdot \vec{r}_j$ changes, and thereby the intensity at the detector. The velocity of a particle depends on its shape and size, which determine the translational diffusion coefficient D_t. A large particle will diffuse slower than a small one, just as a disc will diffuse faster than a sphere with the same radius. The diffusion coefficients for some different shapes are listed in Table 3.2. Sometimes the hydrodynamic radius R_h is used to express the size of non-spherical scattering particles. R_h is the radius of a spherical particle that has the same diffusion coefficient as the non-spherical particle.

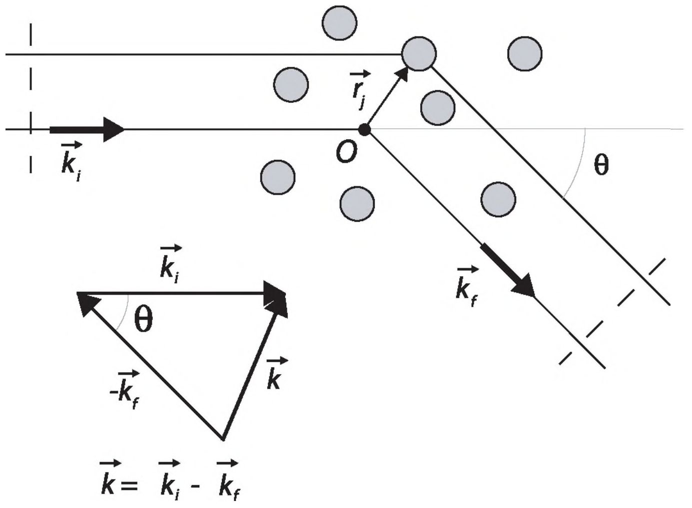

Figure 3.4: *Schematic representation of the scattering by a collection of small particles within the scattering volume. The particle with index j will scatter light with a phase ϕ_j. The wave vector $\vec{k}$ depends on the detection angle θ. Scattering from solvent molecules is neglected.*

The higher the velocity, the shorter the time scale of the intensity fluctuations. This time scale can be measured by calculating the second order autocorrelation function $g^2(\tau)$ of the intensity vs. time data

$$g^2(\tau) = \frac{\langle I(t)I(t+\tau)\rangle}{\langle I(t)\rangle^2}, \tag{3.2}$$

where τ is the delay time. The Siegert equation relates the second order autocorrelation function with the first order autocorrelation function $g^1(\tau)$ as follows [6]

$$g^2(\tau) = 1 + \beta|g^1(\tau)|^2, \tag{3.3}$$

where β is a correction factor of order unity, which accounts for the spatial integration of the detector which are unavoidable in an experiment.

Shape	*Translational diffusion coefficient*
Sphere R =radius	$D_t = \frac{k_b T}{6\pi\eta R}$ [6] $R_h = R$
Cylinder L=length R=radius	$D_t = \frac{k_b T}{3\pi\eta L}\left(\ln(p) + \nu\right)$ $\nu = 0.312 + \frac{0.565}{p^2} - \frac{0.100}{p^2}$ $p = \frac{L}{d}$ [7] $R_h = \frac{L}{2}\left(\ln(p) + \nu\right)^{-1}$
Disc r=radius t=thickness	$D_t = \frac{k_b T}{9\pi\eta r}\left(\sqrt{1 + \left(\frac{t}{2r}\right)^2} + \frac{2r}{t}\ln\left(\frac{t}{2r} + \sqrt{1 + \left(\frac{t}{2r}\right)^2}\right) - \frac{t}{2r}\right)$ [8] $R_h = \frac{3}{2}r\left(\sqrt{1 + \left(\frac{t}{2r}\right)^2} + \frac{2r}{t}\ln\left(\frac{t}{2r} + \sqrt{1 + \left(\frac{t}{2r}\right)^2}\right) - \frac{t}{2r}\right)^{-1}$

Table 3.2: *Diffusion coefficients and hydrodynamic radii for spherical, cylindrical and disc-shaped particles. η is the solvent viscosity, k_b Boltzmann's constant and T the temperature.*

For monodisperse samples, fitting $g^1(\tau)$ with an exponential function directly gives the diffusion coefficient

$$g^1(\tau) = \exp(-\Gamma\tau) = \exp(-D_t k^2 \tau) \tag{3.4}$$

with Γ the mean decay rate. For an accurate measurement, the correlation function is measured for several scattering vectors. The slope of the typical correlation time versus k^2 gives D_t. If the aggregate shape is known, D_t gives the size and vice versa.

An example of a correlation function is shown in Figure 3.5, which was measured on a solution of monodisperse polystyrene spheres ($R \approx 50$ nm). For short τ the correlation function is very high. As τ increases, the correlation between $I(t)$ and $I(t+\tau)$ decreases until the two values are completely independent. Fitting yields a diffusion coefficient of 4.95×10^{-12} m^2/s (solid line in Figure 3.5), which corresponds to a particle radius of 49 ± 2 nm.

In addition to translational motion, rotation of anisotropic particles causes intensity fluctuations. The relative contributions of the translational- and rotational movements to the correlation time depend on the particle properties and the scattering vector [9]. To measure pure translational motion, DLS can be measured at small scattering vectors where the rotational component is negligible.

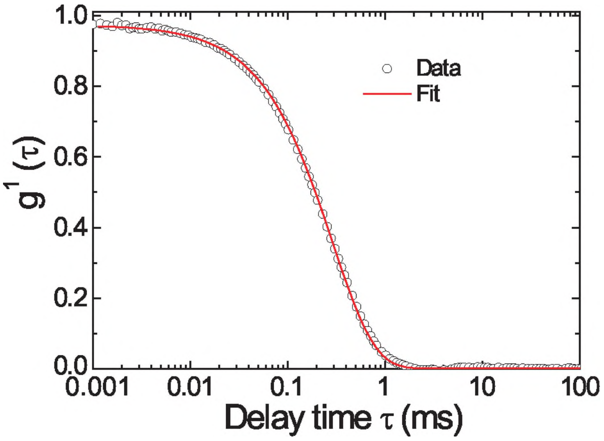

Figure 3.5: *First order autocorrelation function for a solution of monodisperse spherical particles (R_{cal} = 51 ± 2 nm), measured at* $k = 1.87 \times 10^7$ m^{-1}. *The high correlation for short delay times decreases to zero correlation at long delay times. The solid line is a single exponential fit giving* $R = 49\pm$ *2 nm.*

When the aggregate size is polydisperse, the correlation function is not a single exponential, but consists of a distribution of decay rates. In this case the data is usually analyzed in terms of the moments (or cumulants) of the decay rate distribution [10,11]. An alternative is a numerical inversion of the data with a CONTIN analysis [12,13]. However, because the scattered intensity is weighted by the form factor and the mass of the scattering particles, the size distribution determined with these techniques has a negative skew and depends strongly on the scattering angle. This effect is significant for larger and more polydisperse particle sizes. To overcome this problem, the distribution measured with DLS needs to be converted to a number weighted distribution, which is independent of the scattering angle [14,15].

Experimental examples

Figure 3.6 shows an example of a light scattering experiment on thin discs made of amphiphilic gold nanoparticles ("janus" particles) (more information and a detailed description of the experimental setup can be found in reference [16]). Two different organic ligands are connected to small gold nanoparticles (~ 4 nm), and for a specific ratio of the two ligand types, these particles cluster together forming disc shaped objects, as was shown by TEM (see insets Figure

3.6), SEM and AFM. The SLS curve (Figure 3.6 (a)) shows a strong angular dependence, consistent with the presence of monodisperse disc-shaped objects with a radius $R = (1.8 \pm 0.5) \times 10^2$ nm. The small angle DLS results (Figure 3.6 (b)) give $D_t = (1.7 \pm 0.2) \times 10^{-12}$ m^2/s, corresponding to a disc radius of roughly 150 nm. For higher scattering vectors, the relation between Γ and k^2 is no longer linear, which is probably caused by the contribution of rotational motion.

There is quite a good agreement between the sizes found with light scattering and TEM. Especially since the experiments were performed at different moments on different solutions. The light scattering experiments also confirm the shape of the objects. The SLS curve could also be described by spherical objects, but the corresponding dimensions did not agree with the DLS and TEM experiments [16]. Thus, the combination of SLS with DLS conclusively determines the particle shape and size.

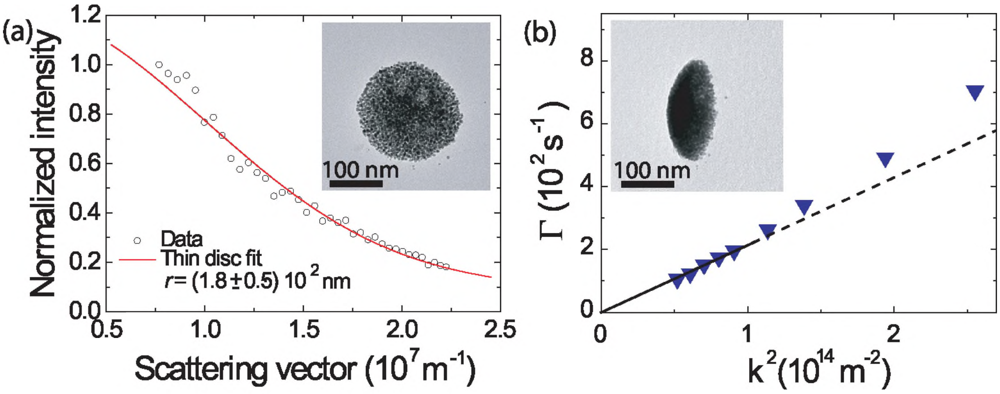

Figure 3.6: *Light scattering data on janus nanoparticles [16]. (a) Static light scattering data with a fit of a thin disc, giving a radius of* $(1.8 \pm 0.5) \times 10^2$ *nm. (b) Dynamic light scattering data. The solid line is a fit of the decay times* Γ *at small scattering vectors, giving* $D_t = (1.7 \pm 0.2) \times 10^{-12}$ *m*^{2}*/s. Insets show TEM images on a 200 mesh carbon coated copper grid.*

Figure 3.7 shows an example of a DLS experiment on a polydisperse system [17]. Two different naphthalene guest molecules $G1$ and $G2$ can bind to the DNA backbone (Figure 3.7 (a)). A CONTIN analysis was performed to measure the aggregate size (distribution) for the two different systems. For $G2$, the intensity distribution has a peak around 4 nm, which means that most of the scattered light is caused by aggregates with $R_h = 4$ nm. This size is consistent with the guest molecules occupying all binding sites on the DNA. Because of the small size, the objects are Rayleigh scatterers, the intensity distribution is almost identical to the number distribution. For $G1$, the objects are much larger, suggesting that the aggregates further assemble into larger structures, as was observed with cryo-TEM as well. The intensity distribution slightly overestimates the average aggregate size, due to the effect described above. Nevertheless a clear difference is observed between the aggregation behavior of the two systems.

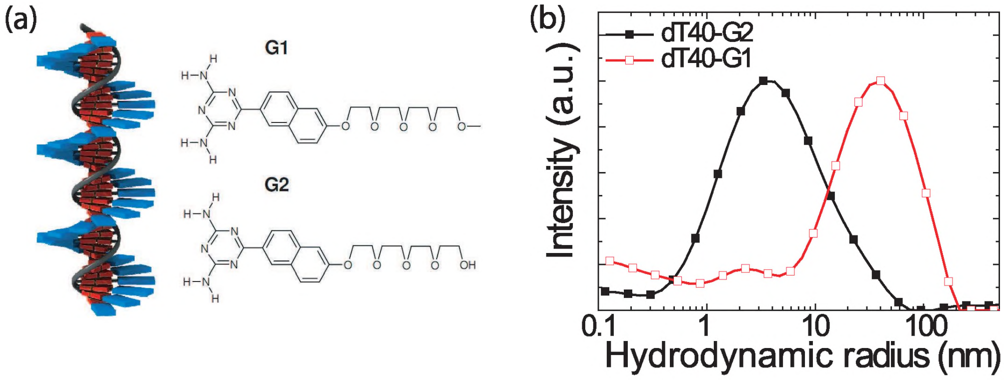

Figure 3.7: *(a) Schematic representation of the assembly of guest molecules G1 and G2 to the DNA template [17]. (b) Intensity weighted size distributions for the two guests attached to a DNA template, forming complexes of different size.*

Figure 3.8 (a) shows an SLS experiment on cylindrical aggregates made of OPV-peptide molecules in water ($C = 10^{-4}$ M) [18]. The peptide group, which is attached to the end of the OPV molecule (see inset), can be used to influence the helical arrangement of the OPV segments. The fit (solid line) indicates the formation of cylindrical aggregates with a length of half a micrometer and a radius of almost 100 nm. However, a cryo-TEM measurement on individual aggregates confirms the cylindrial shape, but the diameter is found to be ~10 nm (Figure 3.8 (b)). Most probably, the cylindrical aggregates cluster together in solution. This was also observed by AFM (Figure 3.8 (c)), which shows a densely packed network of fibers in which the single fibers have a diameter of 10 nm. Usually, the advantage of solution techniques like light scattering or magnetic birefringence is that aggregates can be investigated in their native environment, as compared to scanning probe techniques performed op drop-cast samples. In that case, the evaporation of the solvent often leads to a concentration increase, a changing aggregate shape or clustering [19]. However, in the present case the aggregates most probably already cluster in solution. This example shows that in characterizing supramolecular aggregates, it is often necessary to use several complementary techniques, and one cannot rely on light scattering alone. More examples of light scattering experiments on supramolecular systems can be found in references [20–22].

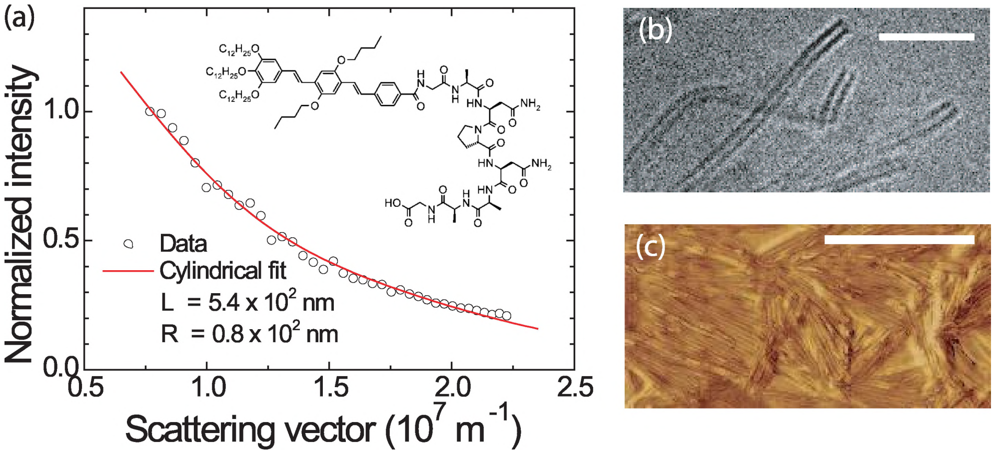

Figure 3.8: *(a) SLS measurement on OPV-peptide aggregates [18]. The data can be described by a cylindrical aggregate shape with a length of half a micrometer and a radius of 80 nm. Inset: schematic representation of the OPV-peptide molecule. (b) Cryo-TEM image of a* 10^{-5} *M solution in water. The scale bar is 50 nm. (c) Tapping mode AFM image of a* 10^{-5} *M solution in water, dropcast on a glass substrate. The scale bar is* $1\mu m$.

Light scattering of aligned aggregates

The scattering of (anisotropic) particles changes when there is a preferred orientation. The idea of exploiting this, either by using flow or electromagnetic fields, is not new in itself (see section 10.4 of reference [3]). However, with the strong magnetic fields available nowadays, light scattering on magnetically aligned samples can be a valuable tool for studying the formation and properties of supramolecular aggregates.

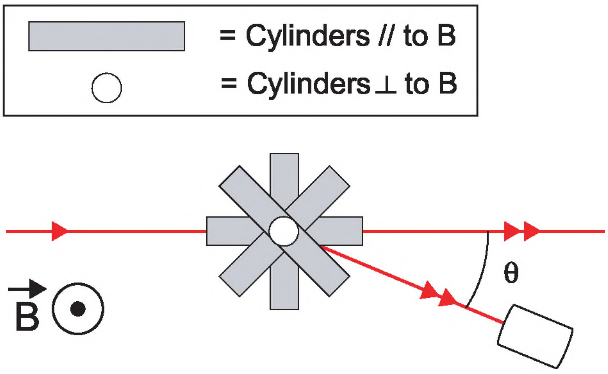

Figure 3.9: *Schematic representation of a light scattering experiment on magnetically oriented aggregates (field direction is out of the figure plane). The situation of alignment parallel to the field is depicted by the white cylinder (seen from the top in the centre of the figure), the perpendicular alignment by the grey cylinders. The cylinders can rotate about the magnetic field axis. The polarization of the light is directed out of the figure plane.*

Static light scattering (SLS)

The form factor is calculated by averaging over the orientations of the aggregates (equation 3.1). Without magnetic field, all orientations have equal probability. In a magnetic field, the orientational distribution function is given by equation 2.6. The preferred orientation drastically changes the form factor. Two limiting situations for thin cylindrical aggregates are schematically depicted in Figure 3.9. The grey (white) cylinders indicate aggregates aligned perpendicular (parallel) to the magnetic field. Figure 3.10 (a) shows the intensity as a function of scattering angle for the two situations compared to the isotropic situation. The (monodisperse) length of the cylinders is 500 nm, the wavelength of the laser light is 600 nm. The curves are normalized at $\theta = 0$ to compare the angular dependence.

The isotropic situation (black solid line) shows the typical behavior for such large objects, with a strong forward scattering. However, when the cylinders align parallel to the magnetic field (dashed red line), the angular dependence of the scattering intensity disappears. On the other hand, for cylinders aligned perpendicular to the magnetic field (dotted green line), the forward scattering is even stronger. The lines are calculated for a monodisperse cylinder length and complete alignment, but a size- and orientational distribution function can easily be incorporated. In an experiment, an increasing magnetic field will lead

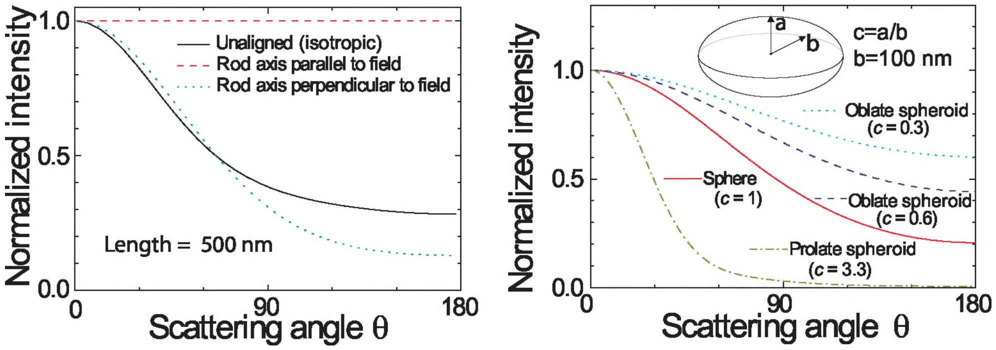

Figure 3.10: *(a) Theoretical scattering intensity as a function of scattering angle for unaligned cylinders (black solid line), cylinders aligned parallel to B (red dashed line) and cylinders aligned perpendicular to B (green dotted line). (b) Theoretical scattering intensity for a sphere (solid red line), two oblate spheroids with different aspect ratios (blue dashed line and blue dotted line) and a prolate spheroid (olive dash-dotted line). The aspect ratio c is defined as the ratio of the radii a and b, where b is fixed at 100 nm (see inset). Both calculations have used* λ*=632.8 nm and* $n_{solvent}$ *= 1.33.*

to an increasing alignment, and the isotropic curve is transformed to one of the aligned curves. Such a big change can resolve possible ambiguities in the interpretation of the isotropic scattering.

A deformation of aggregates can also be observed by performing light scattering in a magnetic field. Recently it was found that spherical sexithiophene nanocapsules can be deformed to oblate spheroids in a magnetic field [23, 24]. Figure 3.10 (b) shows the scattering intensity as a function of the scattering angle for different spheroids, characterized by the aspect ratio $c = \frac{a}{b}$ of their two radii a and b (b is fixed at 100 nm, $c = 1$ is a sphere). For the thiophene nanocapsules, the spheres were transformed to oblate spheroids with an aspect ratio of $c \sim 0.2$ at $B = 20$ T. As the sphere is deformed by the magnetic field, the angular dependence of the scattering intensity strongly changes, indicating that the deformation process can be measured with SLS.

Dynamic light scattering (DLS)

The scattering intensity fluctuates because of particle motion (ignoring rotational motion), since the phase of the scattered light from a particle depends on the dot product between its position vector and the scattering vector. Therefore, a movement perpendicular to the scattering vector does not cause an intensity change. For the case of the cylinders aligned parallel to the magnetic field (Figure 3.9), only the movement perpendicular to the magnetic field is probed. The diffusion coefficient for a cylindrical aggregate in Table 3.2 is the average of the diffusion coefficients for lengthwise and sidewise motion: $D_t^{||}$ and $D_t^{\perp}$ respectively [7]. For cylinders aligned parallel to the field, only $D_t^{\perp}$ is observed, for the perpendicular alignment a combination is observed, but with a different ratio than for the unaligned case. Magnetic alignment therefore allows for the measurement of the two individual components of the diffusion coefficient, leading to a more accurate particle characterization. For larger scattering vectors, D_t is a combination of a translational part and a rotational part. In a magnetic field, when all aggregates are completely aligned, part of the rotational motion is suppressed, leaving only the translational part. This is particularly interesting for large anisotropically shaped aggregates.

References

[1] Kaszuba, M., Connah, M.T., McNeil-Watson, F.K., Nobbmann, U., *Particle & Particle Systems Characterization*, **24** (3), 159-162, 2007.

[2] Schmitz, K.S., An introduction to dynamic light scattering by macromolecules, Academic Press, Boston, 1990.

[3] Kerker, M., The scattering of light - and other electromagnetic radiation, Academic Press, New York, 1969.

[4] Johnson, C.A., Gabriel, D.A., Laser light scattering, Dover publications, New York, 1981.

[5] Van de Hulst, H.C., Light scattering by small particles, Dover publications, New York, 1981.

[6] Berne, B.J., Pecora, R., Dynamic light scattering:with applications to chemistry, biology, and physics, Wiley-Interscience, New York, 1976.

[7] Tirado, M.M., Martinez, C.L., De la Torre, J.G., *The Journal of Chemical Physics*, **81** (4), 2047-2052, 1984.

[8] Mazer, N.A., Benedek, G.B., Carey, M.C., *Biochemistry*, **19** (4), 601-615, 1980.

[9] Aragon, S.R., Pecora, R., *The Journal of Chemical Physics*, **66** (6), 2506-2516, 1977.

[10] Koppel, D.E., *The Journal of Chemical Physics*, **57** (11), 4814-4820, 1972.

[11] Frisken, B.J., *Journal of Applied Optics*, **40** (24), 4087-4091, 2001.

[12] Provencher, S.W., *Computer Physics Communications*, **27** (3), 213-227, 1982.

[13] Provencher, S.W., *Computer Physics Communications*, **27** (3), 229-242, 1982.

[14] Pencer, J., Hallett, F.R., *Langmuir*, **19** (18), 7488-7497, 2003.

[15] Patty, P.J., Frisken, B.J., *Applied Optics*, **45** (10), 2209-2216, 2006.

[16] Jakobs, R.T.M., Van Herrikhuyzen, J., Gielen, J.C., Christianen, P.C.M., Meskers, S.C.J., Schenning, A.P.H.J., *Journal of Materials Chemistry*, **18** (29), 3438-3441, 2008.

[17] Janssen, P.G.A., Jabbari-Farouji, S., Surin, M., Vila, X., Gielen, J.C., De Greef, T.F.A., Vos, M.R.J., Bomans, P.H.H., Sommerdijk, N.A.J.M., Christianen, P.C.M., Leclère, P., Lazzaroni, R., Van der Schoot, P., Meijer, E.W., Schenning, A.P.H.J., *Journal of the American Chemical Society*, **131** (3), 1222-1231, 2009.

[18] Matmour, R., De Cat, I., George, S.J., Adriaens, W., Leclère, P., Bomans, P.H.H., Sommerdijk, N.A.J.M., Gielen, J.C., Christianen, P.C.M., Heldens, J.T., van Hest, J.C.M., Löwik, D.W.P.M., De Feyter, S., Meijer, E.W., Schenning, A.P.H.J., *Journal of the American Chemical Society*, **130** (44), 14576-14583, 2008.

[19] Palermo, V., Palma, M., Tomovic, Z., Watson, M.D., Mullen, K., Samori, P., *Synthetic Metals*, **147** (1-3), 117-121, 2004.

[20] Van Herrikhuyzen, J., Portale, G., Gielen, J.C., Christianen, P.C.M., Sommerdijk, N.A.J.M., Meskers, S.C.J., Schenning, A.P.H.J., *Chemical Communications*, 697-699, 2008.

[21] Janssen, P.G.A., Jonkheijm, P., Thordarson, P., Gielen, J.C., Christianen, P.C.M., Van Dongen, J.L.J., Meijer, E.W., Schenning, A.P.H.J., *Journal of Materials Chemistry*, **17** (25), 2654-2660, 2007.

[22] Lakhwani, G., Gielen, J., Kemerink, M., Christianen, P.C.M., Janssen, R.A.J., Meskers, S.C.J., *The Journal of Physical Chemistry B*, **113** (43), 14047-14051, 2009.

[23] Shklyarevskiy, I.O., Jonkheijm, P., Christianen, P.C.M., Schenning, A.P.H.J., Meijer, E.W., Henze, O., Kilbinger, A.F.M., Feast, W.J., Del Guerzo, A., Desvergne, J.P., Maan, J.C., *Journal of the American Chemical Society*, **127** (4), 1112-1113, 2005.

[24] Manyuhina, O.V., Shklyarevskiy, I.O., Jonkheijm, P., Christianen, P.C.M., Fasolino, A., Katsnelson, M.I., Schenning, A.P.H.J., Meijer, E.W., Henze, O., Kilbinger, A.F.M., Feast, W.J., Maan, J.C., *Physical Review Letters*, **98** (14), 146101-4, 2007.

Chapter 4

Molecular organization of cylindrical sexithiophene aggregates measured by X-ray scattering and magnetic alignment

Abstract

We have determined the internal organization of elongated sexithiophene aggregates in solution by combining small-angle X-ray scattering and magnetic birefringence experiments. The different aggregate axes can be probed independently by performing the experiments on magnetically aligned aggregates. We have found multiwalled cylindrical aggregates consisting of radially oriented sexithiophene molecules with $\pi-\pi$-stacking in the tangential direction, a structure that is considerably different from those previously found in other solvents. The aggregate morphology can thus be tuned by using different solvents, which offers the attractive perspective to steer chemical self-assembly toward nanostructures with desired functionalities, especially in combination with the alignment in a magnetic field.

This work has been published in:
Gielen, J.C., Wolffs, M., Portale, G., Bras, W., Henze, O., Kilbinger, A.F.M., Feast, W.J., Maan, J.C., Schenning, A.P.H.J., Christianen, P.C.M., *Langmuir*, **25** (3), 1272-1276, 2009.

Introduction

Chemical self-assembly of organic molecules into larger aggregates is a promising approach for constructing potentially functional nanostructures. In principle, the large variety of molecular building blocks permits the fabrication of aggregates with a large variation in composition, shape, and functionality [1–5]. In many cases, however, the precise internal molecular arrangement of the nanostructures is unknown, which hampers the development of a deeper understanding of the structure-property relationship, required to steer the self-assembly process toward molecular nanostructures with desired functionalities. In particular, it is important to measure the molecular arrangement of aggregates in the solution in which they are formed. Solution experiments provide a stable environment with well-defined intermolecular interactions, where solvent and temperature dependencies [6–10] can be readily investigated, without spurious effects that can be present when aggregates are characterized after deposition on a substrate, such as molecule-substrate interactions and solvent evaporation [11,12].

To this end, we determined the molecular structure of sexithiophene self-assemblies in a solution of *o*-dichlorobenzene (ODCB) and *n*-butanol. This oligothiophene molecule is interesting as an organic semiconductor material, and a detailed understanding of the ordering is needed to develop protocols for the formation of well-defined supramolecular structures for use in future devices, such as field-effect transistors [13]. We follow an approach that is inspired by studies on biological structures [14,15], which combines the virtues of small-angle X-ray scattering (SAXS) and linear birefringence with magnetic orientation. SAXS is very powerful for resolving internal aggregate structures. Techniques like ^{1}H-NMR [16], circular dichroism, UV/vis absorbance, and fluorescence [9,10,17] mainly probe short-range interactions. On the other hand, techniques such as light scattering (see Chapter 3) [18] and cryo-transmission electron microscopy [19] probe length scales too large to determine the molecular arrangement. To unravel the directionality of the ordering, we performed SAXS and birefringence measurements on magnetically aligned sexithiophene aggregates. We found cylindrical aggregates in which sexithiophene molecules are arranged in a radially symmetric orientation with $\pi-\pi$-stacking in the tangential direction of the cylinder. The techniques used to resolve this structure can be generally applied to any supramolecular aggregate made of π-conjugated molecules.

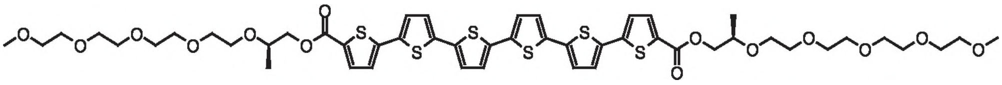

Figure 4.1: *Molecular structure of **T6**.*

Sample preparation

The sexithiophene (**T6**) molecules comprise a π-conjugated α, α'-linked sexithiophene derivative carrying chiral oligo(ethyleneoxide) side chains [10] (Figure 4.1). **T6** forms aggregates in protic polar solvents, with morphologies ranging from spherical structures [20], needles [21], and rodlike helical assemblies to flat “crêpes” [22], where the morphology and resulting properties depend on the solvent and fabrication method used [9,10]. By application of recycling gel permeation chromatography, we were able to purify **T6** to better than 99.9 mol % [21]. The combination of the purified material and the solvent mixture of ODCB and butanol, the boiling points of which are both higher than the aggregation temperature T_{aggr} for the concentration used, allowed us to study the aggregate formation and melting in a reversible way [21].

Like all molecules used for self-assembly, sexithiophene has an anisotropic chemical structure to exploit the directionality in the intermolecular interactions. Such anisotropic molecules are very suitable for magnetic orientation due to their large anisotropy in the magnetic susceptibility [23]. For example, aromatic moieties such as benzene and thiophene tend to align with the aromatic plane parallel to the field, which can be used to orient supramolecular aggregates in solution up to a high degree [24–27]. Furthermore, due to the optical anisotropy of the molecular building blocks, the alignment of the nanostructures leads to a strong linear birefringence. This magnetic birefringence is a sensitive probe for the molecular organization, and the magnetic field strength required for a certain degree of alignment measures the number of molecules per aggregate [28].

To prepare the aggregates, 1 mg of freshly purified **T6** was dissolved in a mixture of 100 μl of ODCB and 1 ml of butanol. To make sure that all pre-existing aggregates were dissolved, the sample was heated to 353 K for at least 0.5 h, before it was slowly cooled to room temperature (cooling rate below 60 K/h) to avoid kinetic effects. Light scattering was used to verify that all molecules were dissolved above T_{aggr} (320 K). At 10 different temperatures below T_{aggr}, the magnetic birefringence was measured in magnetic fields (B) up to 20 T, using a temperature controlled (± 0.1 K) 2 mm thick optical cell. SAXS experiments were performed, only at room temperature, at BM26B at the European Synchrotron Radiation Facility (ESRF) in Grenoble using an X-ray photon energy of 10 keV in combination with a 2D multiwire gas filled detector [29]. In this case, a magnetic field of B = 4 T (1.7 T) was applied perpendicular (parallel) to the X-ray beam.

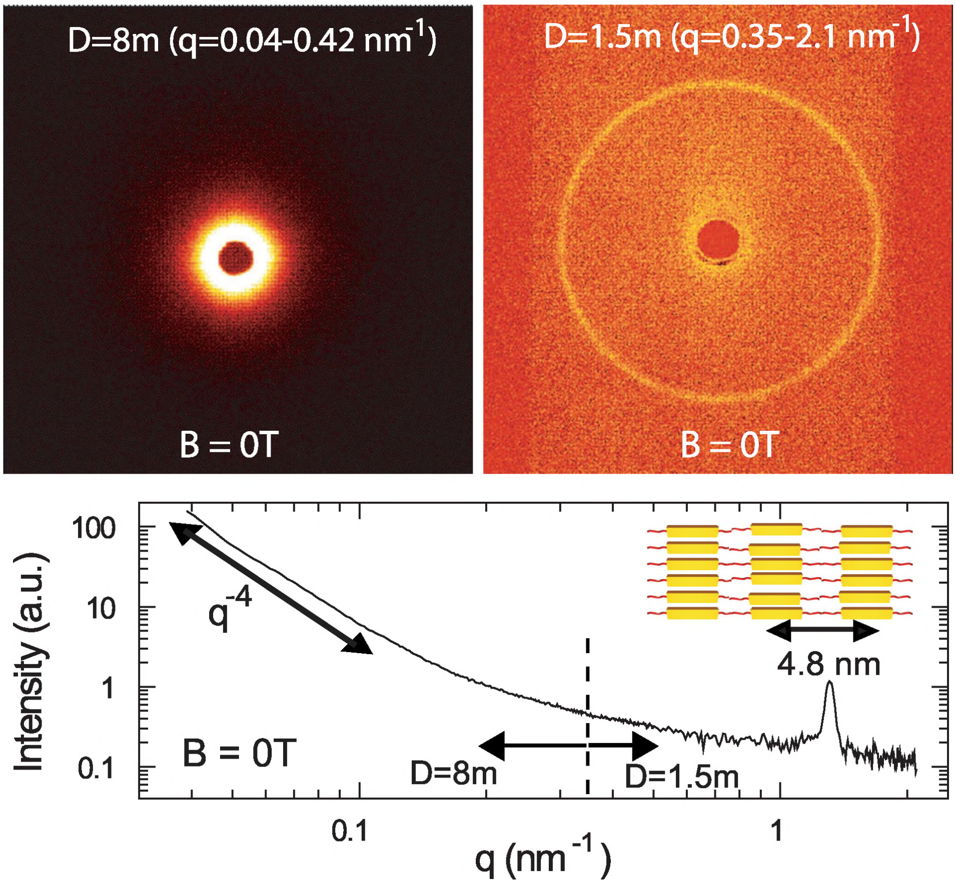

Figure 4.2: *SAXS results of unaligned **T6** aggregates (magnetic field B = 0). Top panels show SAXS images recorded at two different detector distances (D=8 and 1.5 m), with different scattering vector q ranges probing different length scales. Lower panel shows the resulting cross section. The bright ring at q= 1.3 nm^{-1} indicates a typical period of 4.8 nm between two **T6** molecules, as indicated in the inset.*

Small Angle X-ray Scattering (SAXS)

The 1D SAXS profile of the nonaligned sample at B= 0 T displays a q^{-4} slope at small scattering vectors and a sharp peak at q = 1.3 nm^{-1} (Figure 4.2). The initial q^{-4} slope indicates that the molecules self-assemble in large aggregates characterized by a sharp interface between aggregate and solvent, but contains no information on the shape, since the aggregates are too large. The peak at q = 1.3 nm^{-1} corresponds to a typical periodicity of 4.8 nm, consistent with **T6** molecules organized in a head-to-tail fashion (see inset lower panel Figure 4.2).

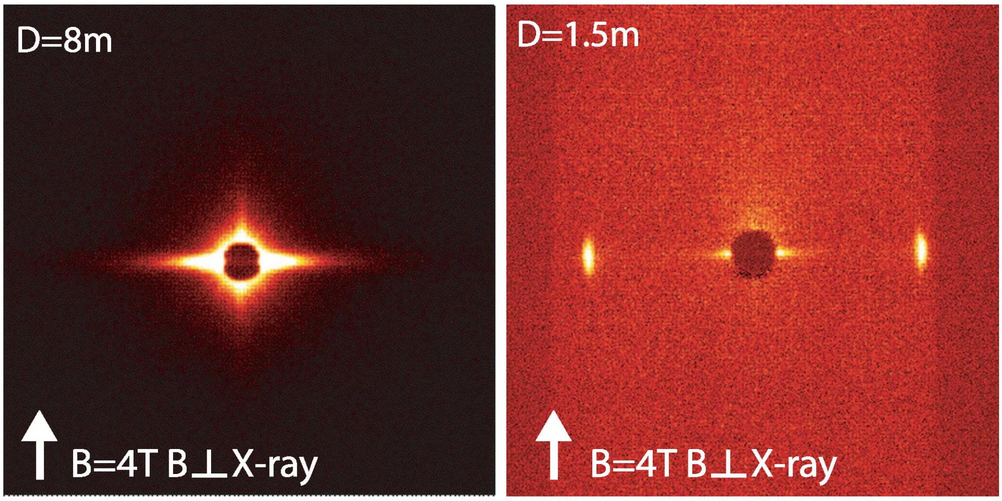

Figure 4.3: *SAXS results with B = 4 T perpendicular to the X-ray beam.*

Figure 4.3 shows SAXS results of **T6** aggregates measured with the X-ray beam perpendicular to a magnetic field of 4 T. The scattered ring at q = 1.3 nm^{-1}, observed with D = 1.5 m to probe the intermolecular distances, is reduced to two bright spots in the direction perpendicular to the magnetic field, due to the magnetic alignment of the **T6** aggregates. The azimuthal width of these spots (Figure 4.4) is inversely proportional to the degree of alignment and saturates at B = 4 T where the alignment is almost complete. The SAXS data taken with D = 8 m (left panel of Figure 4.3) probes the overall shape and reveals a strongly anisotropic scattering pattern, indicating the presence of aligned aggregates with a high shape anisotropy. The observed results indicate that the aggregate dimension along B is larger than that perpendicular to B. Below, we will refer to these dimensions as the long and short axes, respectively.

For B parallel to the X-ray beam (Figure 4.5), the situation is remarkably different. For both detector distances, a radially symmetric scattering pattern is visible, which implies that the long axes of the **T6** aggregates are aligned parallel to the X-ray beam. In spite of the substantial magnetic orientation at $B = 1.7$ T, the rotational freedom of the aggregates about the B-axis leads to the observation of a ring. The striking dependence of the scattering patterns on the relative orientation of the X-ray beam and magnetic field direction highlights the directional sensitivity of our method, and leads to the conclusion that the 4.8 nm periodicity within the aggregates is only present along their short axes.

Magnetic alignment

We also measured the ordering and size of the **T6** aggregates with magnetic birefringence (Figure 4.6) using the setup described in Chapter 2. The sample was contained in a 5mm optical cell (Hellma) with a water-based temperature controller (± 0.1 °C). The magnetic birefringence was measured by slowly sweeping the magnetic field between 0 and 20T. The small birefringence of the pure solvent caused by the experimental setup was used as a background.

For all temperatures above T_{aggr} = 320 K, the birefringence is zero at all magnetic fields, because all molecules are dissolved and no aggregates are present. Below T_{aggr}, the magnetic birefringence increases quadratically with

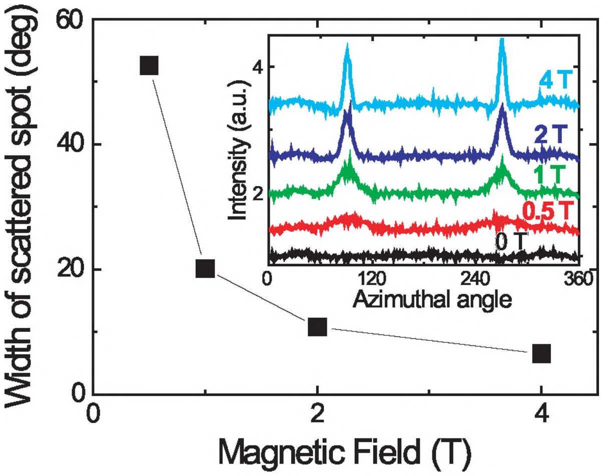

Figure 4.4: *Magnetic field dependence dependence of the azimuthal width of the scattered X-ray beam (B $\perp$ X-ray), which is inversely proportional to the degree of alignment. Inset: azimuthal intensity at q = 1.3 nm^{-1} as a function of B.*

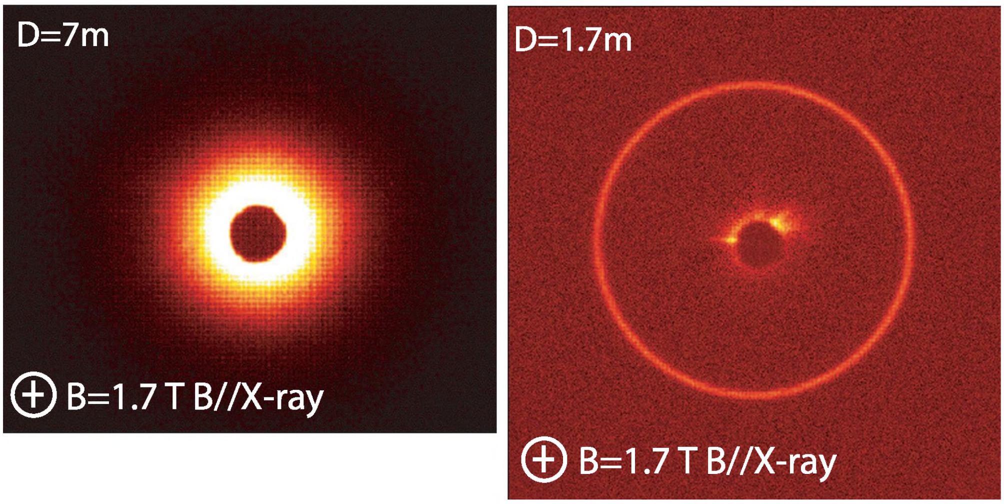

Figure 4.5: *SAXS results with $B = 1.7$ T parallel to the X-ray beam.*

the applied field and saturates at higher fields. With decreasing temperature, the value of the birefringence increases, whereas the field strength needed to saturate the signal decreases, as indicated by the arrows. The first effect is caused by an increasing number of molecules in the aggregated state, yielding higher birefringence values. The second effect is related to an increasing average size of the aggregates, which means that it takes a lower magnetic field to accomplish full alignment (lowering of saturation field). Note that at room temperature the birefringence saturates around 4 T, fully consistent with the X-ray data (Figure 4.4). Fitting the saturation field (lines in Figure 4.6) leads to a reliable estimation of the number of molecules per aggregate for each temperature (inset Figure 4.6). Slightly below the aggregation temperature, the size of the **T6** aggregates sharply increases, until it saturates at lower temperatures to about 8×10^6 molecules per aggregate. In a separate birefringence experiment, it was verified that the aggregation process yielded identical results with or without a magnetic field to make sure that the short periods of exposure to the magnetic field in the birefringence measurements did not influence the aggregation itself.

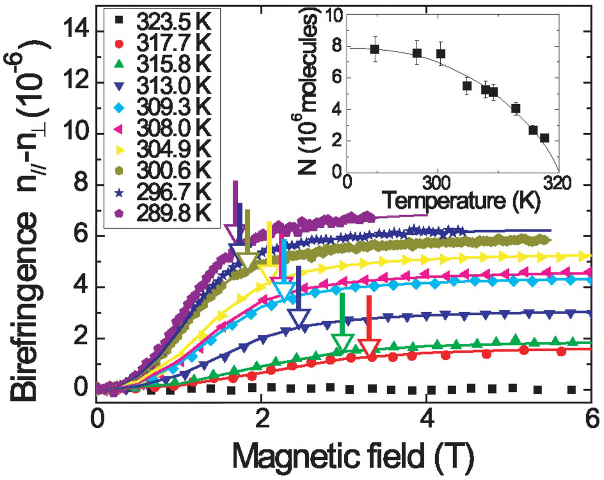

Figure 4.6: *Magnetic birefringence ($n_{//B} - n_{\perp B}$) as a function of magnetic field B for different temperatures. Arrows indicate the point where the birefringence is at 80 % of the saturation value. Solid lines are fits to the data to obtain the aggregate size (expressed in terms of number of molecules per aggregate) shown in the inset. The line in the inset is a guide to the eye.*

Organization

Combining the SAXS and birefringence results conclusively determines the internal structure of the **T6** aggregates. The two bright spots in the SAXS data of aligned aggregates (Figure 4.3) indicate **T6** molecules in a 4.8 nm distance head-to-tail arrangement along its short axis, similar to a lamellar structure, a herringbone structure, or a radial structure. More complicated structures would lead to additional scattering peaks which are not observed. Figure 4.7 shows a schematic representation of the structures with their theoretical alignment behavior in a strong magnetic field. The schematic structures presented here are idealized situations and do not account for a possible helicity caused by the chiral nature of the molecules.

The radial structure is the only proposed structure that is consistent with both the SAXS and birefringence data. It consists of **T6** molecules that are radially oriented with a tangential $\pi - \pi$-stacking, where the tail-to-tail molecular packing occurs only along the short aggregate axis. It necessarily aligns with its long axis along the magnetic field, when all thiophene planes are parallel to B, yielding the anisotropic scattering patterns presented in Figure 4.3. It is also consistent with the birefringence curve, which is a single S-shaped curve that

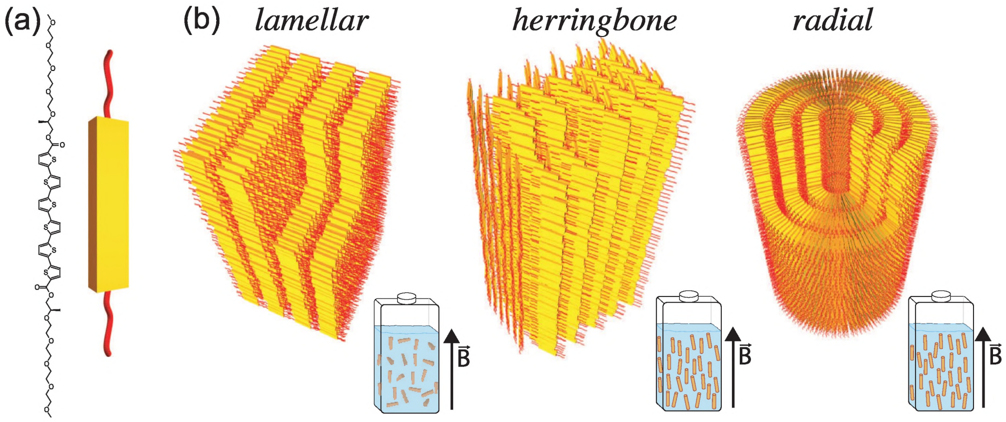

Figure 4.7: *Schematic representations of possible aggregate structures. (a) Molecular structure and schematic representation of **T6**. (b) Three possible **T6** aggregate structures with their energetically most favorable orientation in a strong magnetic field B. Lamellar structure: due to the rotational degrees of freedom, there is seemingly no alignment. Herringbone structure: two stage alignment, but at high B the cylinders align parallel to the field. Radial structure: alignment with the long axis along B.*

is typical for aggregates with a cylindrically symmetric susceptibility (see also Chapter 2) [28]. In contrast, the lamellar structure can align both with its long and short axis along the magnetic field, as long as the planes of the thiophene rings are parallel to the magnetic field [23]. Since the X-ray data reveal only alignment parallel to the magnetic field, this structure can be ruled out. A herringbone structure orients in two-steps: at low magnetic fields, it aligns like the lamellar structure, but in the end it will align with its long axis parallel to the magnetic field, unless the herringbone angle is exactly 45^o by coincidence. Such a two-step alignment process is compatible neither with the birefringence data nor with the SAXS data, where only alignment parallel to the magnetic field was observed in the B = 0-4 T range.

Figure 4.7 (b) shows a schematic representation of the radial structure with three concentric layers of thiophene molecules. To estimate the real number of layers, we need to know the aggregate diameter, the aspect ratio or the aggregate length. Since the aggregates cannot be observed in solution with an optical microscope, the maximum length is of the order of a micrometer. Since the number of molecules per aggregate is about 8×10^6, we expect for an aggregate of 1 μm length a radius of roughly 50 nm, meaning that the true number of thiophene layers will probably be of the order of 10.

Although it is difficult to accurately quantify the birefringence of aggregates in solution, the calculated birefringence of the radial structure shows a good agreement with the birefringence data in Figure 4.6, with a reasonable set of values for the magnetic susceptibility χ and optical polarizability α of **T6** [30]. Using $\alpha_{xx} = 770$ au, $\alpha_{yy} = 400$ au, and $\alpha_{zz} = 95$ au, we are able to explain the absolute value of the birefringence to within a factor of 2 (black line in Figure 4.8). The measured saturation value of the birefringence (6×10^{-6}) is relatively low because, even at high magnetic fields, the cylinders are allowed to rotate about the magnetic field axis, reducing the signal compared to the situation where all **T6** molecules align with their long axis along the field direction. Indeed, the birefringence of aligned radial aggregates is 1 order of magnitude smaller than the calculated [28] and observed [20] maximum birefringence (3×10^{-5}) for deformed spherical aggregates of **T6**.

Aging of the solution

The results described so far have been obtained on aggregates prepared immediately after purification. In such a fresh solution, the aggregates consist of about 8×10^6 molecules at room temperature, which is too small to be observed

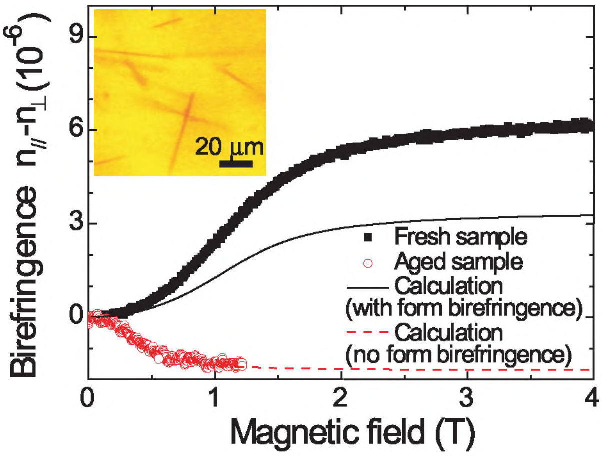

Figure 4.8: *Magnetic birefringence of an aged (6 months) (circles) and fresh solution (squares). Solid and dashed lines are calculated curves for small and large cylinders, respectively. Inset shows a microscope image of an aged solution (6 months after purification) of **T6** cylinders with lengths exceeding 20 µm.*

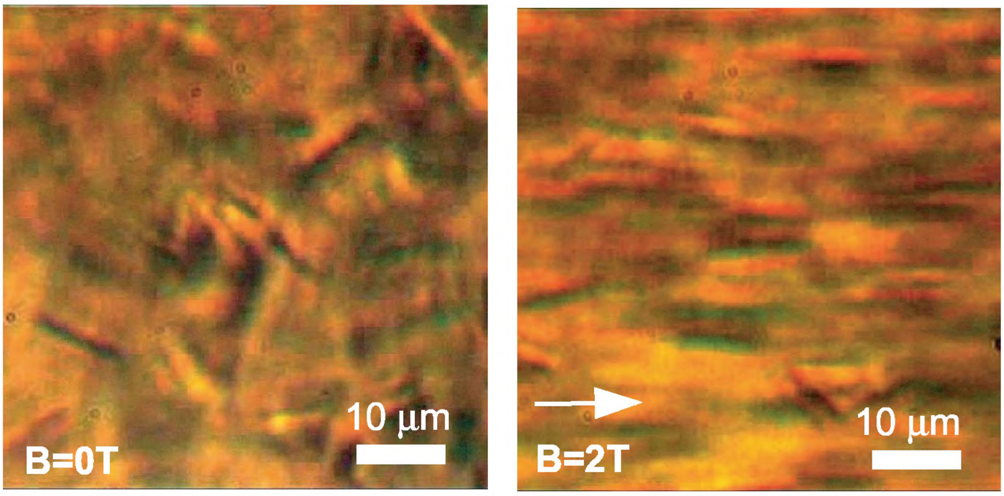

Figure 4.9: *Microscope images of* ***T6*** *aggregates in an aged solution (3 months after purification), showing large cylindrical aggregates. Left image shows the random oriented cylinders at $B = 0$ T, right image shows completely aligned cylinders in a magnetic field of 2 T.*

in solution with an optical microscope. After storage of **T6** molecules in solution in a dark environment for a few months, we found that the aggregate size increases considerably to several micrometers (Figure 4.9), even though the sample was heated and cooled in exactly the same way as the fresh sample. This aging process continues for more than 6 months, with continuously increasing aggregate size (inset of Figure 4.8). The origin of this aging effect is probably associated with a degrading purity of the **T6** compound, which is extensively discussed elsewhere [21]. Here, we merely focus on the consequences for the magnetic alignment (Figure 4.8). The birefringence signal is considerably reduced in amplitude, the sign is reversed, and the field for complete alignment is significantly lowered to $B = 1$ T, which is consistent with the enhanced size. The alignment direction of such an aged sample was verified with a home-built optical microscope in a 2 T magnet (Figure 4.9) to be, again, parallel to the magnetic field. The change of sign of the birefringence signal upon aging of the sample can be readily explained. Assuming that the internal structure of the aggregates remains unchanged, this change of sign is due to the growing of the aggregates and the influence of form birefringence [31]. A dielectric object, with an anisotropic shape and dimensions small compared to the wavelength of the laser light, is more easily polarized along its long dimension than its short dimensions, causing a birefringent effect when all the objects are aligned (page

16 of Chapter 2). We do not know the exact aggregate size in a fresh sample, but 8×10^6 molecules (inset of Figure 4.6) take approximately the same volume as a sphere with a radius of 150 nm, which is much smaller than the laser wavelength of 632.8 nm. So, it is expected that form birefringence plays an important role there. In the aged sample, the aggregate size is several micrometers. On this length scale, the contribution of the form birefringence can be neglected, causing the birefringence to decrease and even change sign (Figure 4.8).

Conclusion

In conclusion, we demonstrated that a combination of X-ray scattering and magnetic fields is a powerful tool to investigate the internal structure of supramolecular aggregates in solution. We applied this combination to the aggregation process of sexithiophene molecules in butanol/ODCB. We found that the **T6** molecules pack in a cylindrically shaped aggregate with the long molecular axis pointing in the radial direction and a $\pi-\pi$-stacking in the tangential direction. Comparing this result with previous work demonstrates that the aggregate morphology can be tuned by using different solvents, which opens the way to study the relationship between the aggregate structure and its properties.

References

[1] Lehn, J.-M., *Proceedings of the National Academy of Sciences USA*, **99** (8), 4763-4768, 2002. (And other articles in this issue of PNAS.)

[2] Lehn, J.-M., *Science*, **295** (5564), 2400-2403, 2002. (And other articles in this issue of Science.)

[3] Hoeben, F.J.M., Jonkheijm, P., Meijer, E.W., Schenning, A.P.H.J., *Chemical Reviews*, **105** (4), 1491-1546, 2005. (And other articles in this issue Chemical Reviews.)

[4] Elemans, J.A.A.W., Rowan, A.E., Nolte, R.J.M., *Journal of Materials Chemistry*, **13** (11), 2661-2670, 2003.

[5] Ryu, J.-H., Hong, D.-J., Lee, M., *Chemical Communications*, (9), 1043-1054, 2008.

[6] Jonkheijm, P., Van der Schoot, P., Schenning, A.P.H.J., Meijer, E.W., *Science*, **313** (5783), 80-83, 2006.

[7] Goto, H., Okamoto, Y., Yashima, E., *Macromolecules*, **35** (12), 4590-4601, 2002.

[8] Lohr, A., Gress, T., Deppisch, M., Knoll, M., Würthner, F., *Synthesis*, 3073-3082, 2007.

[9] Xia, C., Locklin, J., Youk, J.H., Fulghum, T., Advincula, R.C., *Langmuir*, **18** (3), 955-957, 2001.

[10] Henze, O., Feast, W.J., Gardebien, F., Jonkheijm, P., Lazzaroni, R., Leclere, P., Meijer, E.W., Schenning, A.P.H.J., *Journal of the American Chemical Society*, **128** (17), 5923-5929, 2006.

[11] De Feyter, S., Gesquiere, A., De Schryver, F.C., Keller, U., Mullen, K., *Chemistry of Materials*, **14** (3), 989-997, 2002.

[12] Palermo, V., Palma, M., Tomovic, Z., Watson, M.D., Mullen, K., Samori, P., *Synthetic Metals*, **147** (1-3), 117-121, 2004.

[13] Meijer, E.W., Schenning, A.P.H.J., *Nature*, **419** (6905), 353-354, 2002.

[14] Bras, W., Diakun, G.P., Diaz, J.F., Maret, G., Kramer, H., Bordas, J., Medrano, F.J., *Biophysical Journal*, **74** (3), 1509-1521, 1998.

[15] Freyssinet, J.M., Torbet, J., Hudry-Clergeon, G., Maret, G., *Proceedings of the National Academy of Sciences of the United States of America*, **80** (6), 1616-1620, 1983.

[16] Schenning, A.P.H.J., Jonkheijm, P., Peeters, E., Meijer, E.W., *Journal of the American Chemical Society*, **123** (3), 409-416, 2001.

[17] Smulders, M.M.J., Schenning, A.P.H.J., Meijer, E.W., *Journal of the American Chemical Society*, **130** (2), 606-611, 2008.

[18] Micali, N., Villari, V., Castriciano, M.A., Romeo, A., Monsu Scolaro, L., *Journal of Physical Chemistry B*, **110** (16), 8289-8295, 2006.

[19] Vinson, P.K., Bellare, J.R., Davis, H.T., Miller, W.G., Scriven, L.E., *Journal of Colloid and Interface Science*, **142** (1), 74-91, 1991.

[20] Shklyarevskiy, I.O., Jonkheijm, P., Christianen, P.C.M., Schenning, A.P.H.J., Meijer, E.W., Henze, O., Kilbinger, A.F.M., Feast, W.J., Del Guerzo, A., Desvergne, J.P., Maan, J.C., *Journal of the American Chemical Society*, **127** (4), 1112-1113, 2005.

[21] Wolffs, M., Korevaar, P.A., Jonkheijm, P., Henze, O., Feast, W.J., Schenning, A.P.H.J., Meijer, E.W., *Chemical Communications*, 4613-4615, 2008.

[22] Leclère, P., Surin, M., Lazzaroni, R., Kilbinger, A.F.M., Henze, O., Jonkheijm, P., Biscarini, F., Cavallini, M., Feast, W.J., Meijer, E.W., Schenning, A.P.H.J., *Journal of Materials Chemistry*, **14** (13), 1959-1963, 2004.

[23] Maret, G., Dransfeld, K., Biomolecules and Polymers in High Steady Magnetic Fields. In Strong and Ultrastrong Magnetic Fields and Their Applications, Herlach, F., Ed. Springer: New York, 1985; pp 143-204.

[24] Christianen, P.C.M., Shklyarevskiy, I.O., Boamfa, M.I., Maan, J.C., *Physica B: Condensed Matter*, **346-347**, 255-261, 2004.

[25] Kitahama, Y., Kimura, Y., Takazawa, K., *Langmuir*, **22** (18), 7600-7604, 2006.

[26] Shklyarevskiy, I.O., Jonkheijm, P., Stutzmann, N., Wasserberg, D., Wondergem, H.J., Christianen, P.C.M., Schenning, A.P.H.J., De Leeuw, D.M., Tomovic, Z., Wu, J.S., Mullen, K., Maan, J.C., *Journal of the American Chemical Society*, **127** (46), 16233-16237, 2005.

[27] Shklyarevskiy, I.O., Christianen, P.C.M., Aret, E., Meekes, H., Vlieg, E., Deroover, G., Callant, P., Van Meervelt, L., Maan, J.C., *Journal of Physical Chemistry B*, **108** (42), 16386-16391, 2004.

[28] Gielen, J.C., Shklyarevskiy, I.O., Schenning, A.P.H.J., Christianen, P.C. M., Maan, J.C., *Science and Technology of Advanced Materials*, **10** (1), 014601, 2009.

[29] Bras, W., Dolbnya, I.P., Detollenaere, D., Van Tol, R., Malfois, M., Greaves, G.N., Ryan, A.J., Heeley, E., *Journal of Applied Crystallography*, **36**, 791-794, 2003.

[30] Champagne, B., Mosley, D.H., Andre, J.M., *Journal of Chemical Physics*, **100** (3), 2034-2043, 1994.

[31] Bragg, W.L., Pippard, A.B., *Acta Crystallographica*, **6** (11-1), 865-867, 1953.

[32] Horowitz, G., Romdhane, S., Bouchriha, H., Delannoy, P., Monge, J.-L., Kouki, F., Valat, P., *Synthetic Metals*, **90** (3), 187-192, 1997.

Chapter 5

Magnetic field induced rigidification of thiacyanine nanofibers

Abstract

Using fluorescence microscopy, we have observed that application of a 2 T magnetic field transforms flexible thiacyanine nanofibers into straight rigid rods. To investigate the origin of this reversible change in flexibility, we have characterized the magnetic properties of the fibers using a complementary set of techniques, including magnetic birefringence, polarized absorbance and small angle X-ray scattering. We have found that the fibers have a 6-8 nm diameter with a brickwork internal molecular arrangement and that they can be completely aligned in fields in excess of 15 T. The rigidification of the fibers is attributed to a field induced change in the internal structure, rather than by the simple magnetic alignment of fiber segments.

A manuscript with this work is in preparation:
Gielen, J.C., Takazawa, K., Shklyarevskiy, I.O., Portale, G., Bras, W., Maan, J.C., Christianen, P.C.M.

Introduction

The fabrication of functional organic nanostructures using small organic molecules as building blocks is a topic of great current interest. A large variety in aggregate morphologies have been reported, ranging from spheres and cylinders to sheets and tubes [1–5], all with their own properties and functionality. Different morphologies are typically caused by the chemical structure of the molecular building blocks in combination with the environmental conditions like solvent or pH [6, 7]. In some cases, however, the aggregate morphology can be changed by external influences, for instance by light, electric fields or magnetic fields [8–10]. Such externally induced morphology transitions can in principle be fully reversible, which is particularly interesting for applications, since that allows to tune material properties at will.

A special class of molecular aggregates are cyanine aggregates, characterized by a strong change in the optical properties upon aggregation [11]. The internal organization of the aggregates varies strongly, depending on the exact chemical structure of the cyanine molecules [12]. Recent studies on aggregates of thiacyanine dye molecules have shown the formation of fiber shaped aggregates in aqueous solutions, and the possibility to change the fiber morphology by several irreversible external influences like irradiation with light and the addition of NaCl [13]. Because of the application of cyanine aggregates in photographic sensitizers and the use as optical waveguides [14, 15], most studies have focused on tuning the optical properties. The internal structure, and the processes responsible for the morphology change in the case of the thiacyanine fibers, remain mostly unclear.

In this chapter, we describe the extraordinary behavior of thiacyanine fibers in a magnetic field. In a relatively low magnetic field of 2 T, the fiber morphology changes from flexible to rigid. Upon removing the field, the fibers return to the original flexible state, making it a fully reversible change. To identify the mechanism of rigidification, we have combined magnetic birefringence, polarized absorbance and small-angle X-ray scattering (SAXS) to determine the internal structure of the fibers, exploiting the alignment of the fibers in strong magnetic fields. We have found that the fibers have a diameter of only a few nanometers, and that they consist of a simple brickwork arrangement of thiacyanine molecules, with the long molecular axis parallel to the long fiber axis. We provide evidence that the magnetic field induced rigidification is not related to a mere magnetic alignment of segments of the fiber, but that it is caused by a change in the internal molecular arrangement. We will discuss possible mechanisms of this change, and we anticipate that the low field needed for this change in rigidity enables the application in, for instance, the tuning of the solvent viscosity [16].

Sample preparation

Sample solutions were prepared by mixing a 6.8×10^{-5} M solution of 5,5'-dichloro-3,3'-disulfopropyl thiacyanine sodium salt in water (Hayashibara, Figure 5.1 (a)) with an aqueous NaCl solution (5.1 mM) in a volume ratio of 9:1, yielding a thiacyanine concentration of 6.1×10^{-5} M. Within an hour after mixing, the solution becomes opalescent and the molecules self-assemble into fibers with a typical length of 10-30 μm (Figure 5.2 (a)). Upon aggregation, the optical absorbance is strongly increased and red-shifted, characteristic for J-aggregates [11,12,17], with a maximum absorbance at $\lambda = 464$ nm (see Figure 5.1 (b)).

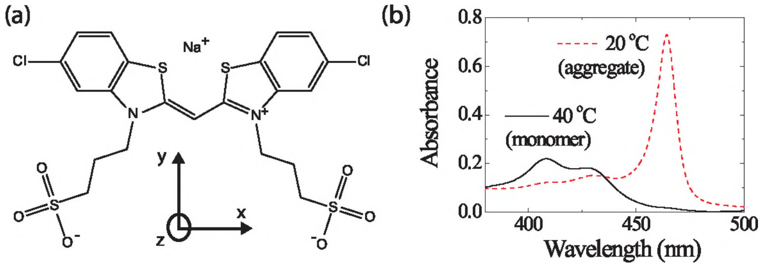

Figure 5.1: *(a) Schematic representation of the thiacyanine molecule with a coordinate system to indicate the different molecular axes. (b) Absorbance spectra of thiacyanine solution. At high temperatures (40°C, black solid line) all molecules are dissolved. At room temperature (red dashed line), the absorbance is strongly enhanced and red-shifted by the aggregation.*

Experimental details

To observe the shape of individual fibers in a magnetic field, fluorescence microscopy (FM) measurements were performed in a superconducting magnet (Japan Magnet Technology, 100 mm bore) using an intensified CCD camera (C8780, Hamamatsu), a 20× microscope objective and an imaging lens (f.l.=800 mm), yielding a sample view of 144×108 μm. An Ar-ion laser was used as excitation source ($\lambda = 488$ nm), in combination with a long pass filter to eliminate the excitation laser.

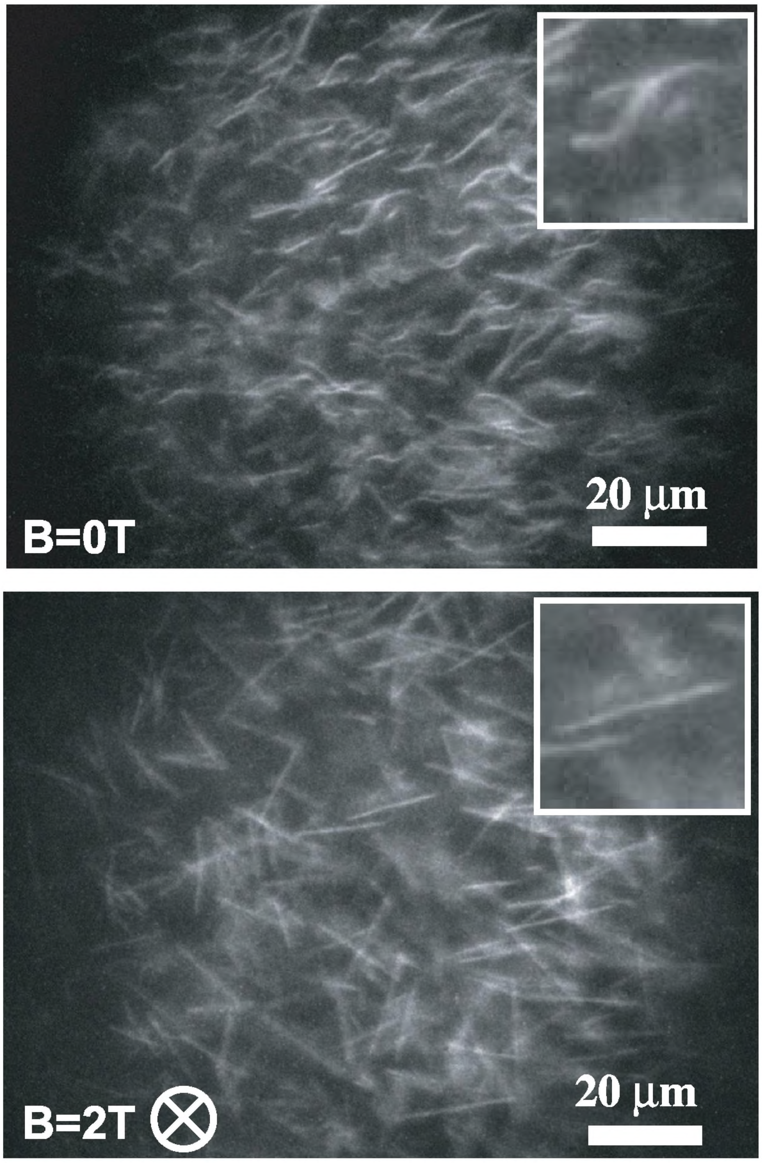

Figure 5.2: *Fluorescence microscopy images of thiacyanine fibers. The viewing direction is parallel to the magnetic field. Insets show close ups of individual fibers. (a) Without a magnetic field. (b) In a magnetic field of 2 T.*

The polarized absorbance was measured using a temperature controlled (T

= 20 °C) 1 mm thick optical cell (Helma), mounted in a 20 T Bitter magnet. Light of a halogen-deuterium source (Avantes) was sent through the optical cell, a lens and a detection polarizer (Glan Thompson), after which it was guided to a spectrometer (Ocean optics, SD2000) with an optical fiber (3M, multimode fiber, 600μm diameter). A full absorbance spectrum was measured for magnetic field values between 0 and 20 T and analyzed at λ = 464 nm. Magnetic birefringence was measured at $T = 20$°C with the setup described in Chapter 2 using a 2 mm thick optical cell (Helma).

SAXS measurements were performed at the Dutch-Belgian BM26B beamline (DUBBLE) at the ESRF in Grenoble (France). An X-ray photon energy of 12 keV and an 8 m sample-to-detector distance were used, yielding a q range of 0.005 $\text{Å}^{-1} < q <$ 0.07 Å^{-1}. The positions of the diffracted peaks from standard silver behenate and rat tail collagen samples were used to calibrate the experimental q-range. The images were recorded using a 2D multiwire gas filled detector. A superconducting magnet was used to expose the sample to magnetic fields up to 6.5 T. For a better signal to noise ratio, the concentration of the thiacyanine solution was increased to 6.8×10^{-4} M for the SAXS measurements.

All techniques were applied at room temperature to fibers in solution to avoid effects that can be present when aggregates are characterized after deposition on a substrate, such as molecule-substrate interactions, aggregate growth due to an increasing monomer concentration or collapsing of the aggregates [10,18,19].

Results

Fiber rigidification

Figure 5.2 shows fluorescence microscopy images of the thiacyanine fibers at B = 0 T and 2 T. Without a magnetic field, the fibers are flexible, as seen by their movement in real time movies. Most remarkably, the flexibility disappears in a magnetic field of only 2 T, and the fibers appear as rigid rods in the FM movie (Figure 5.2 (b)). The rigidification is fully reversible, decreasing the field strength restores the flexibility, and was observed both looking parallel and perpendicular to the magnetic field direction (only the parallel viewing direction is shown in Figure 5.2). During the process of rigidification, the fiber length is unchanged and there are no signs of fiber bundling.

To gain a better understanding of the rigidification process, we have investigated the behavior of the thiacyanine fibers in strong magnetic fields using a set of complementary techniques. We have exploited the fact that, typically, cyanine aggregates can be readily aligned in strong magnetic fields [12,20]. We have used SAXS to investigate the overall magnetic alignment of the fibers, and to obtain information on the fiber thickness. We have used magnetic birefringence and polarized absorbance to determine the molecular orientation in the fibers. This combination of techniques can reveal the internal organization of the fibers, and thereby clarify the rigidification mechanism.

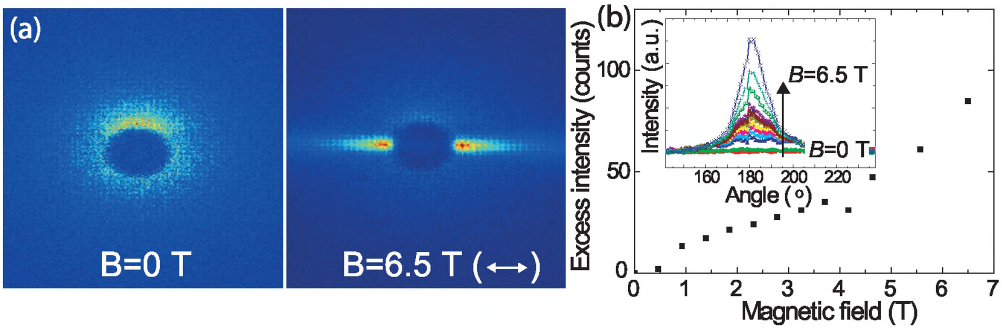

Figure 5.3: *SAXS results. (a) SAXS images at $B = 0$ T and $B = 6.5$ T. The random orientation of the aggregates in the absence of a magnetic field, causing the isotropic scattering pattern, is turned to an anisotropic image by the fiber alignment in a magnetic field. The magnetic field is in the horizontal direction. (b) Scattering intensity in the horizontal direction as a function of magnetic field strength. The scattering without magnetic field is used as a background. Inset shows a full azimuthal scan from which the intensities were determined.*

SAXS

Figure 5.3 (a) shows two SAXS images, with and without applied magnetic field respectively. Without a magnetic field, the random orientation of the aggregates gives an isotropic scattering pattern. In a magnetic field of 6.5 T, we observe a strongly anisotropic scattering pattern, indicative of a significant degree of magnetic alignment. At the q-range used, the X-ray scattering is primarily sensitive to the alignment of the fiber as a whole (*vide infra*). The enhanced intensity in the horizontal direction (along the magnetic field) demonstrates that the fibers align with their long axis perpendicular to the magnetic field.

To determine the degree of alignment, we measured the scattering intensity in the horizontal direction as a function of magnetic field (180° and 360° in the inset of Figure 5.3 (b)). To obtain a zero background signal, we subtracted the zero field intensity. This excess intensity is related to the fraction of fibers oriented with their long axis perpendicular to the magnetic field direction. Between 0 and 6.5 T, the degree of alignment continuously increases. At 6.5 T, there is no sign of saturation, indicating that 6.5 T is not enough to obtain complete alignment.

Figure 5.4 shows the X-ray scattering intensity as a function of q without magnetic field, obtained by integrating the intensity in the 2D image (Figure 5.3 (a))over the azimuthal angle. When plotting $\log(I(q)q)$ vs q^2 (Guinier plot, see inset), the slope for low q values is given by $-\frac{R_c^2}{2}$, with R_c the cross section of the scatterers. Assuming a cylindrical structure, the radius r is given by $r = R_c\sqrt{2}$, yielding $r =$ 6-8 nm [21].

Unfortunately, the integrated SAXS intensity does not show clear peaks to determine the intermolecular distances, nor did any peaks arise when a magnetic field was applied. Most probably, the intermolecular distances within the experimentally accessible range (~1-20 nm) are not so sharply defined and monodisperse, nor in the flexible fibers, nor in the rigid rods[1].

To summarize, from the SAXS data we conclude that the thiacyanine molecules form rodlike aggregates with a radius of 6-8 nm. The fibers align perpendicularly to the magnetic field direction and 6.5 T is not enough to completely align the fibers.

Magnetic birefringence and polarized absorbance

The normalized magnetic birefringence of the thiacyanine solution is shown by the red circles in Figure 5.5. Initially, the application of a magnetic field gives an increase in the birefringence. The birefringence has a maximum at 2 T, beyond which it decreases, changing sign at about 6 T, and saturates around 20 T.

The two alignment steps are also observed in the polarized absorbance measurements. Figure 5.6 (a) shows the full absorbance spectra of the fibers in water for the different polarizations at B = 2.5 T and B = 20 T. Figure 5.6 (b) shows the absorbance at λ = 464 nm as a function of magnetic field for both polarizations. Initially, the parallel (perpendicular) absorbance increases (decreases), reaching a maximum (minimum) around 3 T. For stronger fields, the trend reverses and the absorbance of the two polarizations cross around 6 T. Around 20 T, both signals saturate, with the perpendicular absorbance much stronger than the parallel absorbance. The magnetic field does not cause a

---

[1] A previous SAXS study on similar molecules gave intermolecular distances of the order of $10^1 - 10^2$ nm, but in that case the concentration was much higher and the aggregates did not have a fiber shape [22].

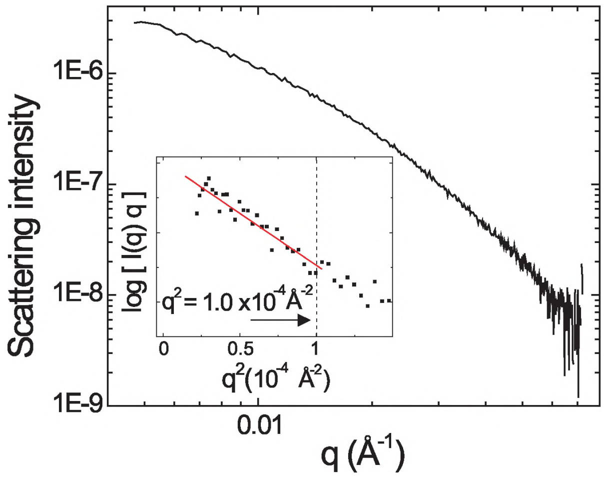

Figure 5.4: *Integrated SAXS intensity of thiacyanine fibers in solution. Inset shows a Guinier plot, with a linear fit of the data in the range of* 2×10^{-5} *Å*$^{-2}$ $< q^{-2} < 1 \times 10^{-4}$ *Å*$^{-2}$*, from which the fiber radius was determined to be 6-8 nm.*

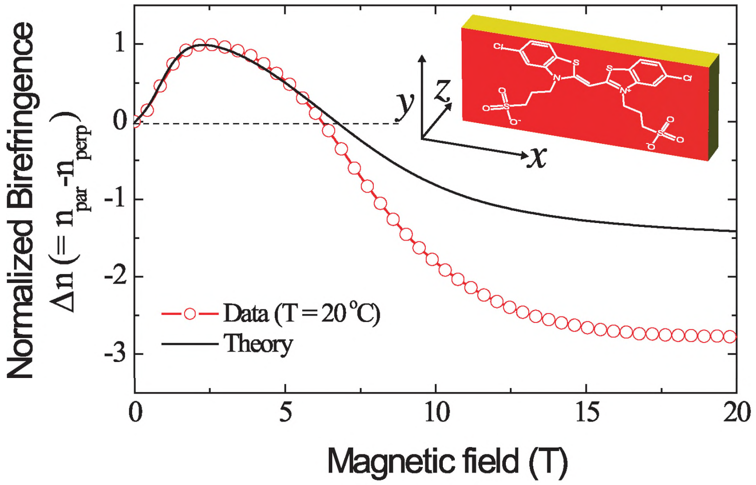

Figure 5.5: *Magnetic birefringence of the thiacyanine fibers (circles), solid line shows the calculation described in the text. Inset shows a schematic representation of the thiacyanine molecules with the principle molecular axes.*

significant shift in the absorbance spectrum, indicating that the intermolecular distances responsible for the strong absorbance peak are almost unchanged.

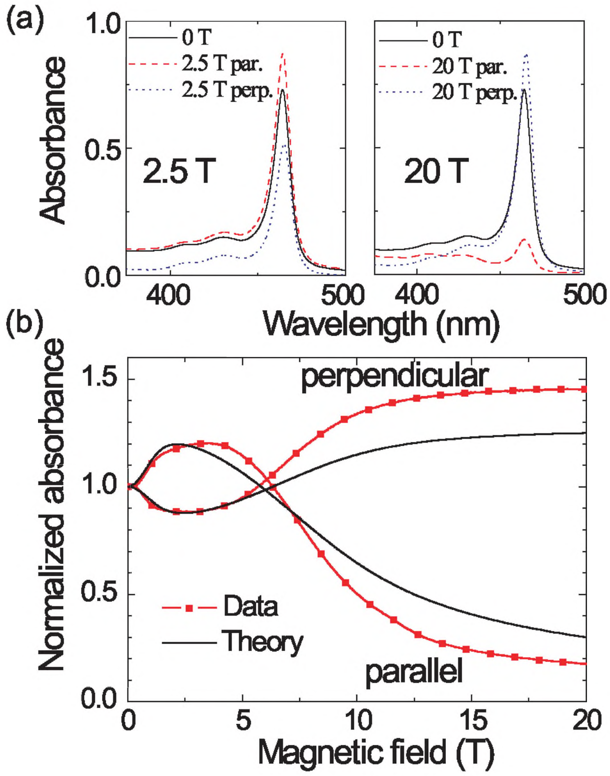

Figure 5.6: *Polarized absorbance of a thiacyanine solution in a magnetic field. (a) Full absorbance spectra at B=2.5T and B=20 T, unpolarized (black solid line), parallel polarization (red dashed line) and perpendicular polarization (blue dotted line). (b) Magnetic field dependence of the absorbance of light with a polarization parallel and perpendicular to the magnetic field respectively, monitored at λ=464 nm. The absorbance is normalized at the zero-field value.*

Discussion

Molecular organization

Based on the birefringence-, polarized absorbance- and SAXS measurements, and using the fact that the thiacyanine molecules form a J-aggregate, we propose the brickwork organization shown in Figure 5.7. The structure shown is a schematic representation, the SAXS results indicate that the intermolecular distances are not so sharply defined. The thiacyanine molecules are oriented with the molecular x-axis along the long fiber axis (consistent with the observation

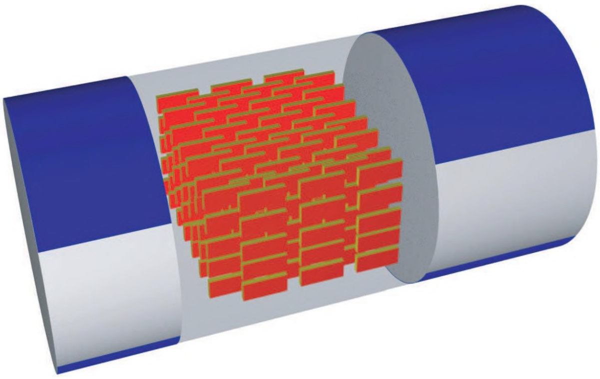

Figure 5.7: *Schematic representation of the proposed molecular organization of the thiacyanine fibers. The molecular x-axis is directed along the long axis of the fiber. The two different short axes of the fiber are marked with a dark and light color.*

by Yao et al. [23]), and the y- and z-axis along the two short axes respectively (for a definition of the molecular axes, see inset of Figure 5.5). As we will show below, this arrangement perfectly explains all the experimental results.

First of all we can understand the birefringence and polarized absorbance data over the entire magnetic field range, using the molecular diamagnetic susceptibilities and polarizabilities of the thiacyanine building blocks. The molecular principle magnetic susceptibilities were calculated by summing the susceptibilities of the individual chemical groups ($\chi_{xx} = -2.1\times10^{-9}$, $\chi_{yy} = -2.05\times10^{-9}$ and $\chi_{zz} = -4.8 \times 10^{-9}$ m^3/mol) [24, 25]. Polarizabilities were obtained by an AM1/MOPAC calculation ($\alpha_{xx} = 4.1 \times 10^2$ au, $\alpha_{yy} = 2.7 \times 10^2$ au and $\alpha_{zz} = 2.1 \times 10^2$ au). It is known that the aggregation might change the polarizabilities, but as long as the anisotropy does not change too much, the normalized birefringence will not change.

The best fit for the birefringence data (solid line in Figure 5.5) is obtained with an aggregate size of $N = 5.5\times10^6$ molecules. Using an estimated molecular volume of ~0.6 nm^3, based on the molecular dimensions, and taking the radius from the SAXS measurements, this N corresponds to a fiber length of $2\times10^1\,\mu$m, consistent with the observed length in the FM images.

The expected polarized absorbance of the proposed structure was calculated by taking the projection of the molecular dipole moment to the different polarization axes, averaged over a Boltzmann distribution (equation 2.6 on page 13). The dipole moment was assumed to be along the x-axis of the molecule. Again, the theoretically expected curve based on the organization shown in Figure 5.7

(solid black line in Figure 5.6 (b)) qualitatively describes the data very well. The best fit was obtained by taking $N = 4.4 \times 10^6$ molecules, comparable to the value used for the theoretical birefringence curve.

From these dependencies we can derive the molecular orientation in a magnetic field. Without magnetic field (Figure 5.8 (a) top), there is no alignment and therefore no birefringence or polarized absorbance. At intermediate fields (Figure 5.8 (b) top), just after the rigidification, only the orientation of the molecular z-axis parallel to the magnetic field is energetically unfavorable, due to the large negative value for χ_{zz}. The molecules are still able to rotate about the magnetic field axis with the cyanine plane along the field direction. On average, this results in a positive Δn and an enhanced (reduced) absorbance of light with a parallel (perpendicular) polarization. At higher fields (Figure 5.8 (c) top), a second orientation step occurs due to the difference between χ_{xx} and χ_{yy}, and all molecules align with the molecular y-axis along the magnetic field, resulting in a change in sign of both Δn and the polarized absorbance. As explained in Chapter 2 (page 20), a two step alignment process gives valuable information on the precise orientation of the thiacyanine molecules in all magnetic fields.

With this field dependent molecular orientation, and the proposed structure of Figure 5.7, we can explain the overall alignment as well. At 2 T, after the first alignment step, there is seemingly no alignment, because there are still fibers with the long axis along the field direction (Figure 5.8 (b) bottom). Only one fiber orientation, with the light face of the cylinder pointing in the magnetic field direction, is energetically forbidden. This gives a small net orientation (of fibers perpendicular to the magnetic field), causing an increase in the SAXS signal along the magnetic field direction (Figure 5.3 (b)). At higher fields, the second alignment step fully orients the fibers perpendicularly to the magnetic field (Figure 5.8 (c) bottom). The birefringence and polarized absorbance measurements show that this second step is almost saturated at 20 T (Figures 5.5 and 5.6 (b)), which is consistent with the fact that the anisotropy in the SAXS did not saturate at 6.5 T.

Flexible to rigid transition

The most intuitive explanation for the magnetic field induced change in flexibility is a simple magnetic alignment of the different segments of the fiber. Without a magnetic field, different fiber segments are able to change their orientation with respect to each other, because of thermal motion. In a strong magnetic field, each fiber segment has a fixed orientation relative to the field axis when the magnetic orientational energy exceeds the thermal energy, leading to an apparent rigidification of the fiber.

However, there are two reasons why such a simple magnetic alignment mechanism cannot be the cause of the rigidification. First, Figure 5.2 (b) shows the microscope view parallel to the magnetic field. The magnetic orientational energy of a fiber segment is independent of a rotation about the magnetic field axis. Therefore, the fibers should be flexible in this viewing angle if the rigidification is a simple alignment effect (Figure 5.9 (a)). Only with a viewing angle perpendicular to the magnetic field direction, the fibers appear rigid, if alignment is the cause of the change in flexibility (Figure 5.9 (b)). Instead, we observe rigid fibers looking from both directions. Second, considering the small thickness of the fibers (6 – 8 nm), the number of molecules per segment

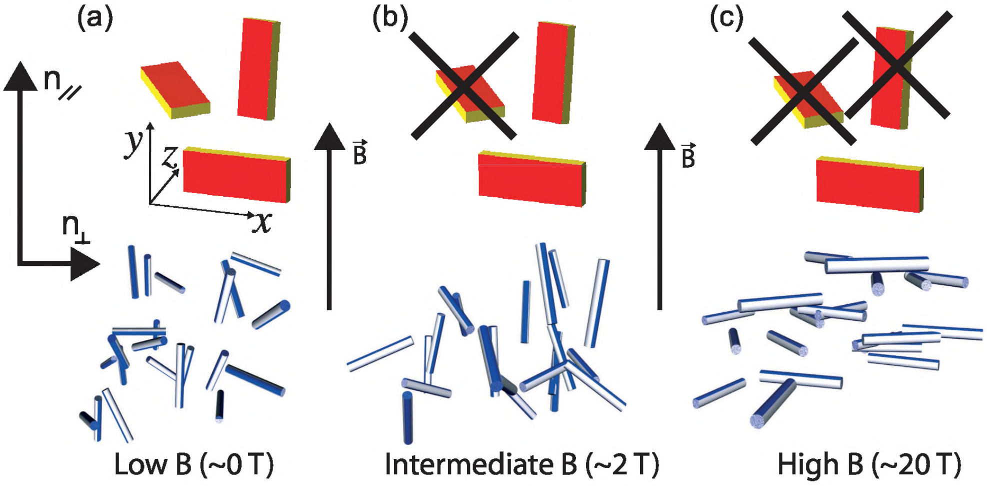

Figure 5.8: *Schematic representation of the magnetic alignment of the molecules within the fibers (top) and the fibers as a whole (bottom). A dark and light face are used to indicate the two different short axes of the fibers. At low fields (a), all molecular orientations have equal probability. The fibers are oriented randomly and all fiber axes can be in the magnetic field direction (long axis, dark short axis and light short axis). At intermediate fields (b), the orientation with the molecular z-axis along the magnetic field direction is energetically unfavorable. For the fibers, there is apparently no alignment, but it is energetically unfavorable to have the light face pointing in the magnetic field direction. At high fields (c), all molecules orient with the molecular y-axis along the magnetic field direction, and all fibers are aligned perpendicularly to the magnetic field with the dark face pointing in the magnetic field direction. The arrows on the left indicate the parallel and perpendicular directions used for birefringence and polarized absorbance measurements.*

is too low to overcome the thermal randomization and to align the segments at such low magnetic field strengths. Even for the fiber as a whole, the degree of alignment at 2 T is very low and fields in excess of 15 T are needed to reach complete alignment.

We attribute the fiber rigidification process to a subtle, magnetic field induced, change in the internal molecular arrangement of the nanofibers. The actual molecular structure of an aggregate is the result of a minimization of its total free energy, with as most important contribution the internal energy due to the intermolecular interactions. It is well known that different cyanine dyes can form different aggregate structures [12]. Furthermore, some cyanine dyes can form different types of aggregates depending on the experimental conditions, such as temperature, concentration and solvent, analogous to polymorphism in crystal growth. In particular, we assume that the free energies of the internal organizations belonging to the flexible and rigid thiacyanine nanofibers studied here are almost identical, given the fact that a transition can be induced by small effects like irradiation with light, aging, or addition of NaCl [13]. We propose that in our experiment a similar structural transition is induced by the application of a magnetic field, which is triggered by a lower magnetic energy of the rigid nanorods relative to the flexible fibers. In addition, also a reduced elastic energy, that is, a smaller fiber bending energy, could play a role, favoring rigid over flexible nanofibers [26,27]. The change in fiber flexibility occurs at a relative low field of 2 T, and coincides with the first magnetic alignment step observed by magnetic birefringence and polarized absorbance. In fact, the observation of this first alignment step demonstrates that indeed the orientational

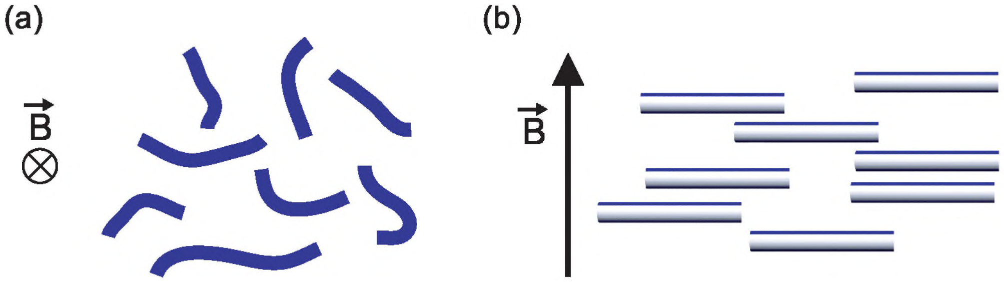

Figure 5.9: *Expected microscope views if the rigidification is an alignment effect. (a) For the viewing direction parallel to the magnetic field, the fibers appear flexible, because the magnetic energy of a molecule is independent of a rotation about the magnetic field axis. (b) For the viewing direction perpendicular to the magnetic field, the fibers look rigid.*

magnetic energy is sufficiently large at low fields to be comparable to the thermal energy and most probably also to the differences in internal energy of the different nanofiber structures. We note that the proposed change in internal fiber structure is too subtle to be visible as a shift in the UV-vis absorbance spectrum. Further experimental and theoretical work is needed to elucidate the precise nature of the field induced change in the flexibility of thiacyanine nanofibers.

Conclusion

We have observed a fully reversible change in the flexibility of thiacyanine aggregates in a magnetic field of only 2 T. To our knowledge, this is the first time that such a magnetic field induced morphology transition has been observed for a supramolecular aggregate at such low fields. Using a combination of fluorescence microscopy, magnetic birefringence, polarized absorption and SAXS, we have determined the internal structure, and we have found a simple brickwork arrangement of the thiacyanine molecules in the fiber. We conclude that the rigidification has to be caused by a structural change of the internal organization, since it cannot be explained by a simple magnetic alignment of fiber segments. Further studies on the relation between the internal organization, external factors like NaCl concentration and magnetic field strength, and the flexibility are important to fully understand the flexibility change.

References

[1] Jiang, L., Hughes, R.C., Sasaki, D.Y., *Chemical Communications*, 1028-1029, 2004.

[2] Hoeben, F.J.M., Shklyarevskiy, I.O., Pouderoijen, M.J., Engelkamp, H., Schenning, A.P.H.J., Christianen, P.C.M., Maan, J.C., Meijer, E.W., *Angewandte Chemie-International Edition*, **45** (8), 1232-1236, 2006.

[3] Elemans, J.A.A.W., Rowan, A.E., Nolte, R.J.M., *Journal of Materials Chemistry*, **13** (11), 2661-2670, 2003.

[4] Ikeda, M., Nobori, T., Schmutz, M., Lehn, J.M., *Chemistry - A European Journal*, **11** (2), 662-668, 2005.

[5] Wang, Z., Medforth, C.J., Shelnutt, J.A., *Journal of the American Chemical Society*, **126** (49), 15954-15955, 2004.

[6] Xia, C., Locklin, J., Youk, J.H., Fulghum, T., Advincula, R.C., *Langmuir*, **18** (3), 955-957, 2001.

[7] Wang, W., Lu, W., Jiang, L., *The Journal of Physical Chemistry B*, **112** (5), 1409-1413, 2008.

[8] Zhou, W., Li, Y., Zhu, D., *Chemistry - An Asian Journal*, **2** (2), 222-229, 2007.

[9] Yoshio, M., Shoji, Y., Tochigi, Y., Nishikawa, Y., Kato, T., *Journal of the American Chemical Society*, **131** (19), 6763-6767, 2009.

[10] Shklyarevskiy, I.O., Jonkheijm, P., Christianen, P.C.M., Schenning, A.P. H.J., Meijer, E.W., Henze, O., Kilbinger, A.F.M., Feast, W.J., Del Guerzo, A., Desvergne, J.P., Maan, J.C., *Journal of the American Chemical Society*, **127** (4), 1112-1113, 2005.

[11] Kobayashi, T., ed., J-Aggregates, Singapore, 1996.

[12] Shklyarevskiy, I.O., Christianen, P.C.M., Aret, E., Meekes, H., Vlieg, E., Deroover, G., Callant, P., Van Meervelt, L., Maan, J.C., *Journal of Physical Chemistry B*, **108** (42), 16386-16391, 2004.

[13] Yao, H., *Annual Reports on the Progress of Chemistry Section C: Physical Chemistry*, **100**, 99-148, 2004.

[14] Sturmer, D. M., Heseltine, D.W., The Theory of the Photographic Process, 4th ed., James, T. H., Ed.; Macmillan: New York, 1977, Chapter 8, and references therein.

[15] Takazawa, K., *Journal of Physical Chemistry C*, **111** (24), 8671-8676, 2007.

[16] Riseman, J., Kirkwood, J.G., *The Journal of Chemical Physics*, **18** (4), 512-516, 1950.

[17] Jelly, E.E., *Nature*, **138**, 1009-1010, 1936.

[18] Palermo, V., Palma, M., Tomovic, Z., Watson, M.D., Mullen, K., Samori, P., *Synthetic Metals*, **147** (1-3), 117-121, 2004.

[19] Cates, M.E., Candau, S.J., *Journal of Physics: Condensed Matter*, **2** (33), 6869, 1990.

[20] Shklyarevskiy, I.O., Boamfa, M.I., Christianen, P.C.M., Touhari, F., Van Kempen, H., Deroover, G., Callant, P., Maan, J.C., *Journal of Chemical Physics*, **116** (19), 8407-8410, 2002.

[21] Guinier, A., Fournet, G., Yudowitch K.L., Small Angle Scattering of X-rays, Wiley, New York, 1955.

[22] Harrison, W.J., Mateer, D.L., Tiddy, G.J.T., *Journal of Physical Chemistry*, **100** (6), 2310-2321, 1996.

[23] Yao, H., Domoto, K., Isohashi, T., Kimura, K., *Langmuir*, **21** (3), 1067-1073, 2005.

[24] Maret, G., Dransfeld, K., Biomolecules and Polymers in High Steady Magnetic Fields. In Strong and Ultrastrong Magnetic Fields and Their Applications, Herlach, F., Ed. Springer: New York, 1985; pp 143-204.

[25] Gupta, R.R., Diamagnetische Suszeptibilität (Landolt Börnstein. Gruppe II, Atom- und Molekularphysik vol. 16), Springer, Berlin, 1986.

[26] Maïssa, P., Lansac, Y., Fried, F., *Polymer*, **37** (11), 2039-2047, 1996.

[27] Jones, R.A.L., Soft Condensed Matter, Oxford University Press, Oxford, 2002.

Chapter 6

Full characterization of the cooperative growth of oligo(p-phenylene-vinylene) nanofibers in solution

Abstract

We have investigated the growth of self-assembled oligo (p-phenylene-vinylene) nanofibers using a complementary set of techniques: atomic force microscopy, dynamic light scattering, magnetic birefringence and circular dichroism spectroscopy. We have determined the temperature dependent length of the chiral fibers in solution and compared it to different growth mechanisms, and we have determined the relevant thermodynamic parameters for this highly cooperative growth process. This shows that a number of techniques is required to characterize the aggregation process over a large concentration range.

A manuscript with this work is in preparation:
Gielen, J.C., Smulders, M.M.J., George, S.J., Jonkheijm, P., Byelov, D., Van der Schoot, Maan, J.C., Meijer, E.W., Schenning, A.P.H.J., Christianen, P.C.M., *in preparation.*

Introduction

The spontaneous self-assembly of organic molecules into larger nanostructures has proven to be a successful strategy for the development of functional materials with a great variety in morphology [1–3]. While the potential of self-assembly is clear, the mechanisms of the formation processes remain often poorly understood. Understanding and developing a mathematical description of these processes and identifying the responsible molecular interactions, allows for the development of functional nanostructures of increasing complexity [4].

There are several growth mechanisms for linear supramolecular aggregates, each with its own physical characteristics. We consider a thermally induced growth, where there is a critical temperature T_p below which the aggregate size changes rapidly. We can distinguish a non-cooperative, isodesmic growth and a cooperative nucleation-elongation growth[1]. For the first mechanism, the strength of the noncovalent interactions between monomers and aggregates, and thereby the association constant, is independent of the aggregate size (Figure 6.1 (a)). Examples of isodesmic behavior are the aggregation of perylene bisimide dyes and porphyrin assemblies [5, 6]. In a cooperative process, the aggregate growth occurs in two stages, each with its own association constant (Figure 6.1 (b)). A recent example of a cooperative growth process is the formation of aggregates of chiral discotic molecules [7]. Whether a system behaves isodesmic or cooperative depends on electronic, structural or hydrophobic effects [8].

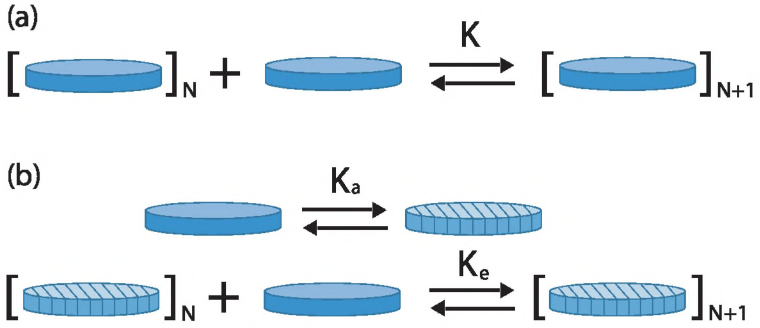

Figure 6.1: *Schematic representation of the models discussed in the text. (a) Isodesmic model with one association constant for the addition of a monomer to a stack. (b) Nucleation growth model, with one association constant for the activation, and one association constant for the growth of the aggregate.*

---

[1] A third mechanism can be considered for systems where ring-closure can occur: the two ends of the linear aggregate connect to each other.

To identify the growth mechanism by which molecules self-assemble, it is important to accurately measure the aggregate size as a function of temperature. We have used dynamic light scattering (DLS) and magnetic birefringence (Δn) to directly measure the growth of oligo (p-phenylene- vinylene) (OPV) aggregates. These aggregates are ideal for our purpose for several reasons. First, the OPV molecules form highly ordered one-dimensional molecular fibers that can be structurally characterized by atomic force microscopy (AFM) [10–12], of which the growth can be compared to the different growth mechanisms described above. Second, the molecules form chiral aggregates, resulting in a circular dichroism (CD) signal to probe the aggregation process. Third, the molecules have strong optical and magnetic anisotropies, which is a prerequisite for magnetic birefringence measurements.

DLS is a common technique for characterizing micellar growth [13], and magnetic birefringence is frequently used in our group to analyze supramolecular self-assemblies. For the interpretation of these results on supramolecular aggregates, knowledge of the fibers persistence length and the fraction of aggregated material at each temperature is a prerequisite. These quantities were measured by AFM and CD respectively. In contrast to the use of mere spectroscopic techniques, we can study highly concentrated solutions with this set of techniques, we can distinguish the situation of a small number of large aggregates from a large number of small aggregates (see Figure 6.2 (c) and (d)), and we can unravel different processes giving rise to the same spectroscopic changes [9]. This allowed us to accurately determine the thermodynamic parameters for the cooperative growth process of the OPV molecules.

OPV fibers

The molecular building blocks comprise oligo (p-phenylenevinylene) derivatives with chiral side chains (OPV3 and OPV4, structures shown in Figure 6.2 (a)). In apolar solvents, OPV dimers are formed via the self-complementary quadruple ureido-s-triazine hydrogen bonding units. These dimers reversibly self-assemble into cylindrical helical stacks due to $\pi - \pi$-interactions of the phenylenevinylene backbone (Figure 6.2 (b)). Small angle neutron scattering experiments showed that the diameter d of the chiral stacks are d_{OPV3}=5 nm and d_{OPV4}=6 nm [10] respectively, which corresponds to the length of a dimer.

These fibers can be transferred to a solid support by drop-casting [11]. Figure 6.3 (a) shows a typical AFM image of OPV4 fibers made by drop-casting a 1.3×10^{-5} M solution in heptane on a HOPG substrate. The fibers are not clustered [14] and ring-closure is not observed. Because of the effects of solvent evaporation and molecule-substrate interactions, AFM is not suited for measuring the temperature dependent aggregate size quantitatively, but it is useful for visualization and determination of the fiber properties. Figure 6.3 (b) shows a length histogram of the fibers, showing an exponential distribution ($P(L) = \frac{1}{\bar{L}}\exp(-\frac{L}{\bar{L}})$) with an average length $\bar{L} = 2.6 \times 10^2$ nm. Such a distribution is theoretically predicted for both the isodesmic and the cooperative growth model [15].

Measuring the contour length and end-to-end distance of 65 free laying fibers, showed that the fibers were equilibrated on the surface (Figure 6.3 (c))

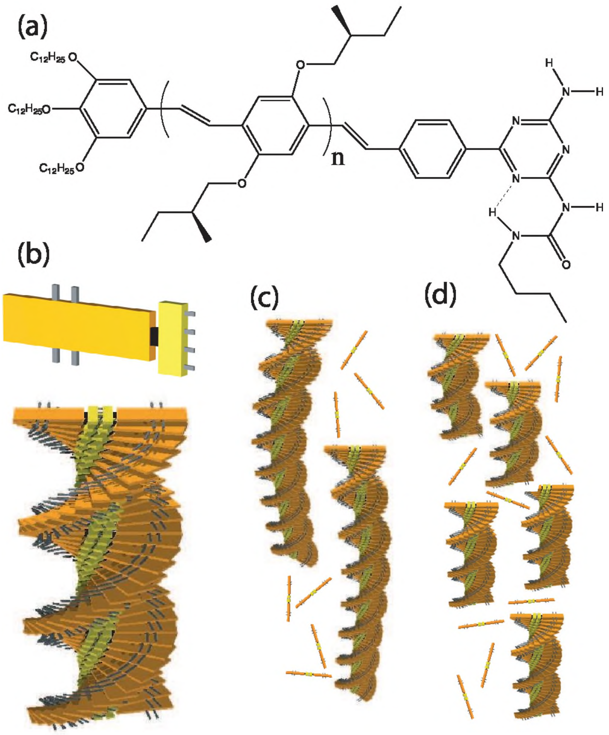

Figure 6.2: *(a) Molecular structure of the oligo(p-phenylenevinylene) molecules. For OPV3 n=1 and for OPV4 n=2. (b) Schematic representation of the organization of the monomers in a fiber. Two monomers form a dimer by hydrogen bonding, which form a chiral stack. (c) and (d) Schematic representation of a solution with a small number of large fibers versus a larger number of smaller fibers, which cannot be distinguished based on the fraction of aggregated material only. Individual dimers are drawn to indicate the belance between monomers and aggregates.*

[16], yielding a persistence length $l_p = 3.5 \times 10^2$ nm [17]. For the OPV3 fibers, we expect a comparable but slightly smaller value for l_p, due to the reduced π-conjugated area. The persistence length is an important parameter for the interpretation of magnetic birefringence measurements on flexible fibers (see page 23 of Chapter 2).

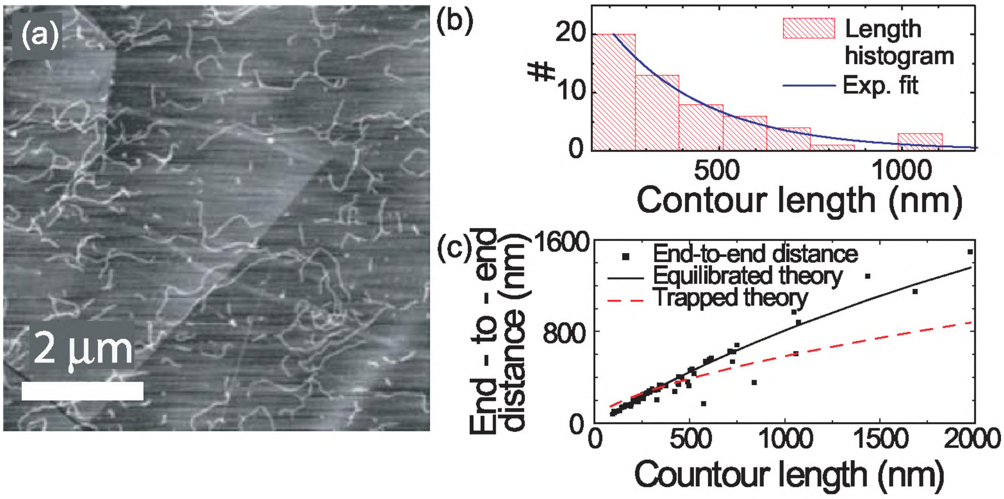

Figure 6.3: *(a) AFM image of OPV4 fibers on HOPG made by drop-casting a* 1.3×10^{-5} *M solution in heptane. (b) Histogram showing the aggregate length distribution of 65 free laying fibers from the image of part a. Solid line is an exponential distribution with a typical length of* 2.6×10^2 *nm. Due to the image resolution, fibers smaller than 150 nm were difficult to measure, and were therefore ignored in the analysis. (c) Measured end-to-end distance versus contour length for the 65 fibers from the AFM analysis, compared to the theoretical curves for equilibrated (solid black line) and trapped (dashed red line) fibers.*

Experimental details

The aggregate growth experiments were performed in solution at a concentration of 1mg/ml in dodecane ($C_{OPV3} = 8.9 \times 10^{-4}$ M, $C_{OPV4} = 6.7 \times 10^{-4}$ M). Solutions were heated and filtered using Alltech HPLC PTFE syringe filters with a pore size of 0.45 μm. UV-vis absorbance measurements before and after filtering showed that the concentration did not change.

For all measurements, the sample was heated to 20 K above the aggregation temperature for 15 minutes to dissolve all existing aggregates. Then the sample was slowly cooled to room temperature, to observe the aggregates in the thermodynamically equilibrated state/size. For the CD measurements, the cooling rate was 1 K/min. For the DLS and birefringence experiments the effective cooling rate was even lower because of the time needed for the measurement at every temperature (never exceeding 1 K/min between consecutive measurements). Measurements with the different techniques were performed on the same physical solution within one week time, to rule out possible degradation of the sample.

Circular dichroism spectra were recorded on a Jasco J-815 spectropolarimeter, equipped with a Peltier temperature controller (PFD-425S). The CD signal was measured at one monitoring wavelength every 0.1 K during cooling. CD, being a background free method, is preferred over UV-vis absorbance to measure the fraction of aggregated molecules. Because of the strong absorbance a thin cuvet was used with an optical path length of 1 mm.

The DLS measurements were performed with a computerized homemade goniometer in the angular range of 30 to 90 degrees (an extensive description of the scattering setup can be found in Chapter 3). The cuvet (Hellma, 10 mm diameter) was submerged in a glycol bath to avoid reflections from the cuvet walls. The incident beam was produced by a dye laser operating at 597 nm. The scattered light was captured using a single mode optical fiber with a collimating lens in combination with an ALV/SO-SIPD single photon detector. The detector output was sent to an ALV-5000/E multiple tau digital correlator, using a typical acquisition time of 100s. A temperature controller was used to stabilize the temperature within 0.1 K during the measurements.

The magnetic field induced birefringence was measured with the setup described in Chapter 2. The sample was contained in a 5 mm optical cell (Hellma) with a water-based temperature controller (± 0.1 °C). The magnetic birefringence was measured by slowly sweeping the magnetic field between 0 and 20 T. The small birefringence of the pure solvent, caused by the experimental setup, was used as a background.

Results

Figure 6.4 (a) shows the *circular dichroism* spectra for the aggregated state of the OPV derivatives at room temperature, with a bisignated Cotton effect caused by the helical arrangement of the transition dipoles of the OPV molecules. The aggregation was monitored at wavelengths λ_{mon} in the wing of the CD peaks ($\lambda_{mon,OPV3} = 325$ nm and $\lambda_{mon,OPV4} = 400$ nm, indicated by the ar-

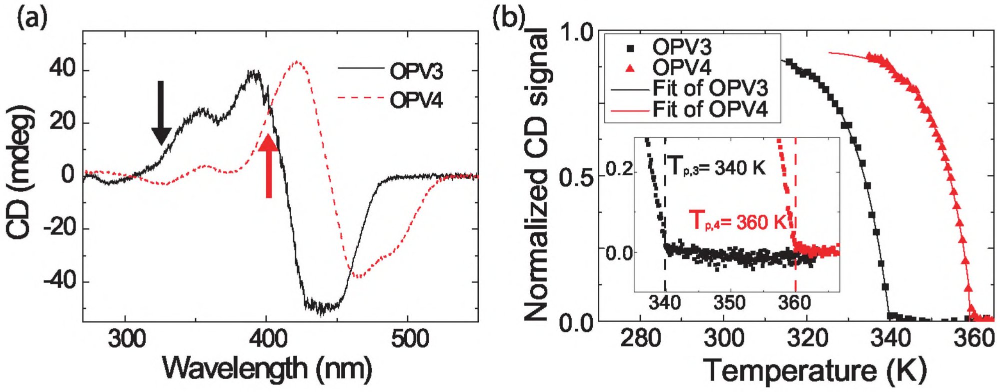

Figure 6.4: *(a) CD spectra of the OPV aggregates in dodecane at room temperature. The arrows indicate the monitoring wavelengths* ($\lambda_{mon,OPV3}$ = 325 *nm and* $\lambda_{mon,OPV4}$ = 400 *nm). (b) Temperature dependent CD signal at the monitoring wavelengths. Solid lines indicate the theoretical fits, yielding* $h_{p,OPV3} = 120 \pm 6$ *kJ/mol and* $h_{p,OPV4} = 144 \pm 6$ *kJ/mol. Inset shows the sharp onset of the CD signal at* T_p *(indicated by the dashed line).*

rows), because of the high concentration and the strong absorbance. Since only molecules in chiral aggregates contribute to the signal, CD probes the fraction of helically aggregated material η. Because of the high concentrations and the relatively small aggregate size, knowledge of η is essential to extract the average aggregate length from the light scattering and magnetic birefringence data (see Chapter 2).

Figure 6.4 (b) shows the normalized increase of the CD signals at λ_{mon} with decreasing temperature. A zero CD signal above the elongation temperature ($T_{p,OPV3}$ = 340 K and $T_{p,OPV4}$ = 360 K) demonstrates the absence of (chiral) aggregates. Below T_p, the CD signals abruptly increase with decreasing temperature, and saturate when all monomers are incorporated in chiral aggregates.

Dynamic light scattering was used as a direct probe of the aggregate length. For several temperatures below T_p, the intensity correlation functions were measured for different scattering vectors q (see Figure 6.5 for an example). For the small scattering vectors (q_{min}= 7.7 μm^{-1} and q_{max}=15 μm^{-1}) the correlation functions were fitted using a cumulant analysis [18] (solid lines in Figure 6.5), allowing the determination of the mean decay rate as a function of q^2 (inset of Figure 6.5). The slope gives the translational diffusion coefficient (top part of Figure 6.6). Above T_p, there is only scattering from monomers and solvent. Be-

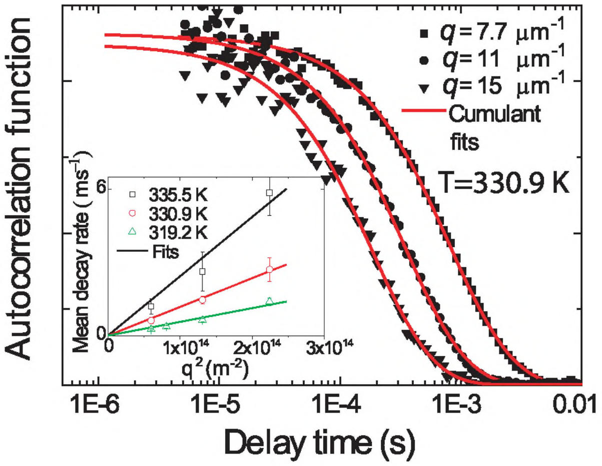

Figure 6.5: *Correlation functions for the OPV3 sample at 330.9 K measured at a scattering angle of 30° (squares), 45° (circles) and 60° (triangles) (scattering vectors q=7.7, 11, and 15 μm^{-1}). Solid lines are the cumulant fits. Inset shows the decay rates obtained by the cumulant analysis of the small angle measurements for three different temperatures. A linear fit (solid lines) is used to obtain the diffusion coefficient.*

low T_p, the scattering intensity increases and the diffusion coefficient decreases due to the aggregate growth (see Chapter 3).

The standard expression for the diffusion coefficient D_t for a cylindrical aggregate of length L at infinite dilution is given in units of m^2s^{-1} by [19]

$$D_t = \frac{k_b T}{3\pi\eta_s L}\left(\ln(\frac{L}{d}) + 0.312 + \frac{0.565d}{L} - \frac{0.050d^2}{L^2}\right), \tag{6.1}$$

with η_s the solvent viscosity in units of $kgm^{-1}s^{-1}$ and d the aggregate diameter. This equation is almost exact for $L/d < 30$, but its error is smaller than the experimental error far beyond this regime. The aggregate length L is related to the aggregate size N by the intermolecular distance in the aggregate ($L = \frac{N}{2} \times 0.35$ nm).

Because of the shape of the fibers and the high concentration used, the structure factor relates the apparent diffusion coefficient D_{app} to D_t with the volume fraction of aggregates ϕ and the weight-averaged aspect ratio $\bar{A} = \frac{\bar{L}}{d}$ [20]

$$D_{app} = D_t\left(1 + 2\phi\bar{A}\right), \tag{6.2}$$

where ϕ was estimated assuming a similar density for the OPV molecules in dodecane as the solvent itself, resulting in $\phi = 1.33 \times 10^{-3}$ for both compounds.

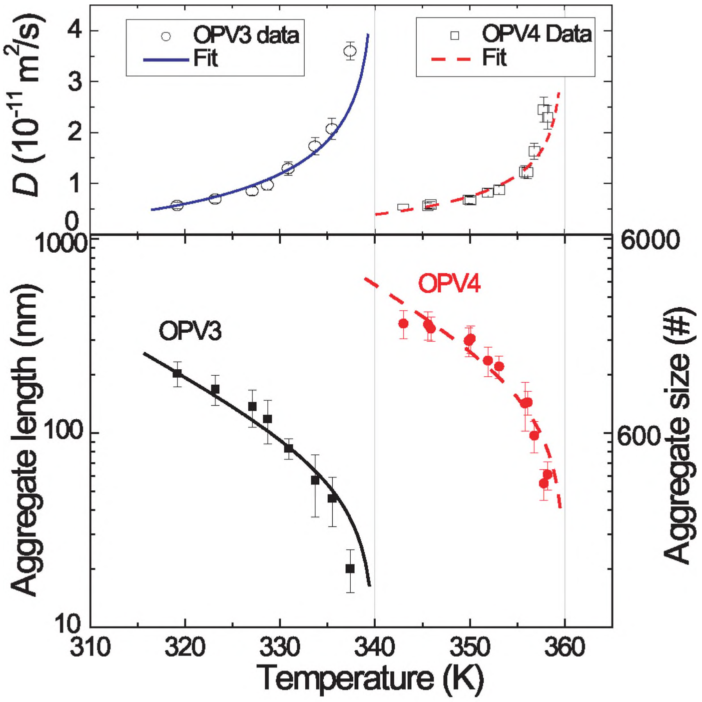

Figure 6.6: *Light scattering data. Top part: Diffusion coefficients as a function of temperature for OPV3 (circles) and OPV4 aggregates (squares). Lines show the diffusion coefficients corresponding to the fit of the data in the bottom part, obtained using the polymerization enthalpy obtained from the CD data. Bottom part: The corresponding average aggregate length for OPV3 (black squares) and OPV4 (red circles). Lines are the fits to obtain K_a. The grey vertical lines are positioned at the elongation temperatures.*

The bracketed term causes the diffusion coefficient to saturate for large L, since $D_t \propto \frac{1}{A}$. This reduces the sensitivity of DLS at low temperatures, when the aggregates are long. With these equations, the diffusion coefficients measured by DLS were converted to an average aggregate length (symbols in bottom part of Figure 6.6) by taking the z-average of D_{app} over an exponential size distribution [21]. At temperatures just below T_p, the aggregates are small with a length below 50 nm. Cooling causes an abrupt growth, almost to the micrometer regime, within a temperature range of only 20-30 K.

Magnetic birefringence gives an additional, independent method to determine the aggregate size. The diamagnetic anisotropy of the OPV molecules and the high degree of order within the chiral fibers cause the aggregates to align

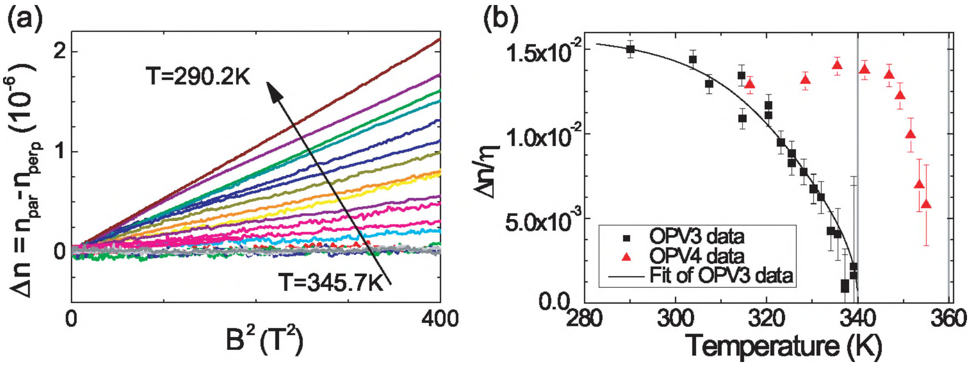

Figure 6.7: *(a) Magnetic field induced birefringence in the OPV3 solution. The birefringence is linearly proportional to the square of the magnetic field, the slope increases with decreasing temperature due to an increasing aggregate size and an increasing η. (b) Slope of the birefringence curve divided by η as a function of temperature. This gives the relative size of the aggregates. The solid line is a theoretical fit yielding $K_{a,OPV3} = 3 \pm 2 \times 10^{-6}$. For the OPV4, artifacts give a decrease of the birefringence at low temperatures (see text). The vertical lines indicate the elongation temperatures.*

perpendicularly to the magnetic field, with the conjugated plane of the OPV molecule parallel to the field. The longer the fibers, the easier the thermal randomization can be overcome, and the better the aggregates align, which leads to the size dependence of this method.

The magnetic field induced alignment is measured as linear birefringence Δn, shown for the OPV3 in Figure 6.7 (a) as a function of the square of the magnetic field. Above T_p, Δn is zero, because there are no ordered aggregates of considerable size. Below T_p, the magnetic alignment of the fibers causes Δn to increase linearly with B^2, indicating that the alignment is far from saturation because of the relatively small number of molecules per aggregate. With decreasing temperature, the slope of the $\Delta n(B^2)$ curve increases due to the growth of the fibers and the increase in the fraction of aggregated molecules η. Quantitatively, the slope is proportional to the number of molecules in an aggregate N, η, and the anisotropies in the polarizabilities $\Delta\alpha$ and magnetic susceptibilities $\Delta\chi$ (see page 22 of Chapter 2). Figure 6.7 (b) shows the slope of the $\Delta n(B^2)$ divided by η, which gives the relative length of the aggregates as observed with magnetic birefringence. For an absolute length, accurate values for the anisotropies ($\Delta\alpha$ and $\Delta\chi$) are required.

Because of the fiber flexibility, the length observed with magnetic birefringence is smaller than the actual length of the fiber. For short fibers, this effect is very small, but for fibers much larger than l_p, an increase of the length will give only a small increase of the birefringence. With the persistence length, and equation 2.25 on page 23, the relative *observed* lengths from the birefringence can be transformed to relative *fiber* lengths.

Discussion

The strong increase of the aggregate size below T_p, as observed with DLS and Δn, and the rapid increase of η observed with CD, confirms the cooperative growth process as was observed before for OPV solutions at lower concentrations [22]. An isodesmic process would have shown a more moderate growth. Figure 6.1 (b) shows a typical example of a cooperative growth process, where a monomer is activated, allowing for a stack to grow. Although there are other types of nucleated assembly mechanisms, they are practically difficult to distinguish. Therefore we use the mathematically simplest one [15], which was modified using first order approximations of the association constants [23], leaving only two parameters to characterize the entire growth: the enthalpy of the addition of a monomer h_p, and the equilibrium constant of activation at the elongation temperature $K_a(T = T_p)$, further referred to as K_a. The elongation temperature T_p can be easily identified as the temperature below which the aggregates rapidly grow. Other theoretical descriptions of cooperative growth mechanisms with more parameters require more independent techniques since, for instance, different sets of parameters can give comparable spectroscopic signals [24,25].

To extract h_p and K_a from the data, we have used the following procedure: we have fitted the fraction of aggregated material, measured by CD, to obtain h_p. Then, we fitted the lengths obtained with light scattering and birefringence with only K_a as fitting parameter, using h_p and η from the CD. In principle, the light scattering and birefringence experiments can give both h_p and K_a. However, our two step approach with the CD data gives more accurate results, since we can determine each parameter with an independent technique. For some other systems and less concentrated solutions, spectroscopic signals like CD or UV-vis absorbance can be directly related to the aggregate size, assuming a certain growth model. However, for highly cooperative systems and high concentrations, the abrupt change in the spectroscopic signal hampers an accurate determination of the association constants and thereby the aggregate length, particularly in the case absorbing samples [7].

We have fitted $\eta(T)$ below the elongation temperature T_p using the expression of the modified cooperative growth model [23]

$$\eta(T) = 1 - \exp\left(\frac{h_p}{k_b T_p^2}(T - T_p)\right) \qquad (T < T_p) \tag{6.3}$$

with k_b Boltzmann's constant. h_p is the only fitting parameter (solid lines in Figure 6.4 (b)), T_p was determined manually from the onset of the CD signal. Only the temperature regime 25 K below T_p was fitted, because in this regime the aggregates are relatively small, and the influence of linear dichroism (LD) is negligible [26]. For both data sets we obtain excellent fits, yielding $h_{p,OPV3} = 120 \pm 6$ kJ/mol and $h_{p,OPV4} = 144 \pm 6$ kJ/mol.

Within the same model, the temperature dependent average length is given by

$$\bar{N} = \frac{1}{2} + \frac{1}{2}\sqrt{1 + \frac{4\eta \exp(\frac{-h_p(T-T_p)}{K_b T_p^2})}{K_a(T = T_p)}}. \tag{6.4}$$

It was assumed that the activation enthalpy is small compared to h_p [27]. With η and h_p from the CD, and the length measured with DLS and magnetic birefringence, the missing parameter $K_a(T = T_p)$ can be determined with two independent techniques.

Only the DLS data in the temperature range of 15-20 K below T_p were fitted (lines in the bottom part of Figure 6.6, the corresponding theoretical diffusion coefficients are given by the lines in the top part). For lower temperatures, the fibers become so long they start overlapping, which hampers the diffusion. The values giving the best fits are $K_{a,OPV3} = 8 \pm 3 \times 10^{-6}$ and $K_{a,OPV4} = 1.2 \pm 0.3 \times 10^{-6}$.

For the OPV3 aggregates, fitting the relative lengths obtained with magnetic birefringence gave $K_{a,OPV3} = 3 \pm 2 \times 10^{-6}$ (solid line in figure 6.7 (b)). The OPV4 data could not be fitted because of the peculiar behavior at low temperatures (Figure 6.7 (b)). The slope of the birefringence decreases below 335 K, even though the fraction of aggregated material is almost constant. This reduction is not caused by a decreasing aggregate length. The combination of the high volume fraction and the large aggregate length (DLS experiments show an average fiber length of almost a micrometer) most probably leads to hindrance in the alignment of the fibers: the fibers cannot fully orient to the magnetically most favorable orientation because they are hindered in their motion by neighbouring aggregates. Such a reduction in the birefringence has been observed before for macrocycle aggregates [28] (see Chapter 7).

The good fits in Figures 6.4, 6.6 and 6.7 demonstrate that the growth of OPV aggregates is described very well by a cooperative growth model. The parameters describing the aggregate growth are summarized in Table 6.1. The good fits show there is no need to incorporate the full temperature dependence of K_a, which would require an additional fitting parameter.

	OPV3 $C_{OPV3} = 8.9 \times 10^{-4}$ M		OPV4 $C_{OPV4} = 6.7 \times 10^{-4}$ M	
	value	*technique*	*value*	*technique*
h_p	$120 \pm 6\times$ kJ/mol	CD	$144 \pm 6\times$ kJ/mol	CD
K_a	$8 \pm 3 \times 10^{-6}$ $3 \pm 2 \times 10^{-6}$	DLS Birefringence	$1.2 \pm 0.3 \times 10^{-6}$	DLS

Table 6.1: *The values for the growth parameters of the OPV derivatives found with CD, DLS and magnetic birefringence.*

The values found for h_p are comparable to the ones in reference [22], where also CD was used for determining the enthalpy. The larger chromophore length for the OPV4 molecules gives a stronger π-π-interaction, causing $h_{p,OPV4}$ to be larger than $h_{p,OPV3}$. This is consistent with the observation that $T_{p,OPV3} < T_{p,OPV4}$, despite the slightly higher molar concentration of OPV3. The larger h_p, the faster the aggregates will grow with decreasing temperature and the larger the aggregates will be.

In contrast to the good agreement for h_p, the obtained values for K_a are much smaller than the values found in reference [22], which is caused by the fact that the concentration we used is higher. T_p increases with increasing concentration, and thereby the temperature where K_a is evaluated. Since the equilibrium constant decreases with increasing temperature, $K_a(T = T_p)$ decreases with increasing concentration [7].

The small values of K_a indicate a high degree of cooperativity, with the consequence of a large aggregate size. In this particular case of OPV molecules, structural effects are the most probable cause of the cooperativity. The molecule should be flat to be incorporated in a stack, where in solution, it is most likely not flat. Therefore, to become part of an aggregate, the molecule must adopt a thermodynamically less favorable conformation [8], which is the activation step, leading to the cooperative growth behavior.

Conclusion

In conclusion, we have determined the thermodynamic growth parameters for OPV aggregates using a combination of AFM, spectroscopic techniques, DLS and magnetic field induced birefringence. The good agreement between the measured aggregate size and the theoretical values shows that a cooperative growth model gives an excellent description of the growth of supramolecular aggregates. Studying the controlled temperature induced growth of supramolecular aggregates will lead to a better understanding of the underlying mechanisms. We have shown that a large number of techniques is needed for an accurate characterization of the growth at all concentrations.

References

[1] Service, R.F., *Science*, **309** (5731), 95-, 2005.

[2] Shimizu, T., Masuda, M., Minamikawa, H., *Chemical Reviews*, **105** (4), 1401-1444, 2005.

[3] Ryu, J.H., Hong, D.J., Lee, M., *Chemical Communications*, 1043-1054, 2008.

[4] Chen, Z., Lohr, A., Saha-Moller, C.R., Würthner, F., *Chemical Society Reviews*, **38** (2), 564-584, 2009.

[5] Würthner, F., Thalacker, C., Diele, S., Tschierske, C., *Chemistry - A European Journal* , **7** (10), 2245-2253, 2001.

[6] Haino, T., Fujii, T., Watanabe, A., Takayanagi, U., *Proceedings of the National Academy of Sciences*, **106** (26), 10477-10481, 2009.

[7] Smulders, M.M.J., Schenning, A.P.H.J., Meijer, E.W., *Journal of the American Chemical Society*, **130** (2), 606-611, 2008.

[8] De Greef, T.F.A., Smulders, M.M.J., Wolffs, M., Schenning, A.P.H.J., Sijbesma, R.P., Meijer, E.W., *Chemical Reviews*, **109** (11), 5687-5754, 2009.

[9] Dehm, V., Chen, Z., Baumeister, U., Prins, P., Siebbeles, L.D.A., Würthner, F., *Organic Letters*, **9** (6), 1085-1088, 2007.

[10] Jonkheijm, P., Hoeben, F.J.M., Kleppinger, R., Van Herrikhuyzen, J., Schenning, A.P.H.J., Meijer, E.W., *Journal of the American Chemical Society*, **125** (51), 15941-15949, 2003.

[11] Jeukens, C., Jonkheijm, P., Wijnen, F.J.P., Gielen, J.C., Christianen, P.C.M., Schenning, A.P.H.J., Meijer, E.W., Maan, J.C., *Journal of the American Chemical Society*, **127** (23), 8280-8281, 2005.

[12] Schenning, A.P.H.J., Jonkheijm, P., Peeters, E., Meijer, E.W., *Journal of the American Chemical Society*, **123** (3), 409-416, 2001.

[13] Von Berlepsch, H., Harnau, L., Reineker, P., *Journal of Physical Chemistry B*, **102** (39), 7518-7522, 1998.

[14] Huisman, B.A.H., Bolhuis, P.G., Fasolino, A., *Physical Review Letters*, **100** (18), 188301-4, 2008.

[15] Van der Schoot, P., Nucleationand Co-Operativity in Supramolecular Polymers. In *Advances in Chemical Engineering*, (vol 35), Koopmans, R.J., Ed. Elsevier, 2009.

[16] Samori, P., Ecker, C., Gossl, I., De Witte, P.A.J., Cornelissen, J.J.L.M., Metselaar, G.A., Otten, M.B.J., Rowan, A.E., Nolte, R.J.M., Rabe, J.P., *Macromolecules*, **35** (13), 5290-5294, 2002.

[17] Rivetti, C., Guthold, M., Bustamante, C., *Journal of Molecular Biology*, **264** (5), 919-932, 1996.

[18] Koppel, D.E., *The Journal of Chemical Physics*, **57** (11), 4814-4820, 1972.

[19] Tirado, M.M., Martinez, C.L., De la Torre, J.G., *Journal of Chemical Physics*, **81** (4), 2047-2052, 1984.

[20] Van der Schoot, P., McDonald, J.A., *Langmuir*, **11** (12), 4614-4616, 1995.

[21] Berne, B.J., Pecora, R., Dynamic light scattering: with applications to chemistry, biology, and physics, Wiley, New York, 1976.

[22] Jonkheijm, P., Van der Schoot, P., Schenning, A., Meijer, E.W., *Science*, **313** (5783), 80-83, 2006.

[23] Van der Schoot, P., Theory of Supramolecular Polymerization. In Supramolecular Polymers, Ciferri, A., Ed. Taylor&Francis: 2005.

[24] Dudowicz, J., Freed, K.F., Douglas, J.F., *Journal of Chemical Physics*, **119** (23), 12645-12666, 2003.

[25] Douglas, J.F., Dudowicz, J., Freed, K.F., *Journal of Chemical Physics*, **128** (22), 224901, 2008.

[26] Wolffs, M., George, S.J., Tomovic, Z., Meskers, S.C.J., Schenning, A.P.H.J., Meijer, E.W., *Angewandte Chemie International Edition*, **46**, 8203-8205, 2007.

[27] Van Gestel, J. Theory of Helical Supramolecular Polymers, *Thesis, Technische Universiteit Eindhoven*, Eindhoven, 2003.

[28] Gielen, J.C., Ver Heyen, A., Klyatskaya, S., Vanderlinden, W., Höger, S., Maan, J.C., De Feyter, S., Christianen, P.C.M., *Journal of the American Chemical Society*, **131** (40), 14134-14135, 2009.

Chapter 7

Aggregation kinetics of macrocycles detected by magnetic birefringence

Abstract

We have used magnetic field induced birefringence as a new sensitive technique to probe the aggregation kinetics of macrocyclic molecules in solution. We have found three consecutive aggregation stages: disordered objects, ordered fibers, and a network. The transition from disordered objects to ordered fibers is found to be slow, taking days or weeks to complete. We anticipate that linking aggregation kinetics to molecular properties will lead to a better understanding of the mechanisms by which molecules self-assemble, allowing for a more rational design of the molecular building blocks.

This work has been published in:
Gielen, J.C., Ver Heyen, A., Klyatskaya, S., Vanderlinden, W., Höger, S., Maan, J.C., De Feyter, S., Christianen, P.C.M., *Journal of the American Chemical Society*, **131** (40), 14134-14135, 2009.

Introduction

Self-assembly of organic molecules offers an attractive approach for the development of potentially functional nanostructures using relatively simple molecular building blocks [1]. In contrast to the numerous investigations of the structural properties of supramolecular aggregates, only a small number of studies focus on the time scale of self-assembly [2,3], disassembly [4], and aggregate morphology transitions [5]. The kinetics can give valuable information on the aggregation route and the intermolecular interactions, allowing for better tuning of the molecular building blocks needed for rational design of complex functional nanostructures [6–8].

We have investigated the kinetics of the temperature-induced aggregation of macrocyclic molecules in solution using magnetic field induced birefringence. This technique is sensitive to the degree of molecular order of an entire aggregate rather than the short range order probed by techniques such as UV-vis and circular dichroism spectroscopy. Therefore, we can distinguish ordered and disordered macrocycle aggregates in a quantitative manner. We have found that after a monomeric solution of macrocycles is cooled to a temperature T_f below the aggregation temperature, it takes days or weeks to form ordered aggregates, with a formation rate that increases with decreasing T_f. Such slow formation is unusual for individual conjugated aggregates, which exhibit typical time scales of a few seconds [9] to several hours [10]. We attribute this exceptionally slow behavior to the polystyrene tails of the macrocycles, which hamper the aggregation of the rigid cores.

Macrocycles

The shape-persistent macrocycle (Figure 7.1) comprises a phenylene-ethynylene-butadiynylene backbone as a rigid core [11] [12]. Four extraannular tert-butyl groups and two large, flexible polystyrene chains are attached to the vertices of the backbone to enhance the solubility of the molecule.

The molecule possesses a large anisotropy in the diamagnetic susceptibility ($\Delta\chi \approx 10^{-7}$ m^3/mol) resulting from the coplanar orientation of the phenyl rings [13]. An external magnetic field tends to orient such anisotropic molecules in order to minimize their magnetic energy. However, for individual molecules, the change in energy is small relative to the thermal energy. Only a large group of ordered molecules can overcome the thermal randomization and align. Therefore, only ordered aggregates of sufficient size can be oriented by experimentally available magnetic fields, whereas disordered aggregates cannot [14]. The induced alignment can be detected optically as magnetic-field-induced bire-

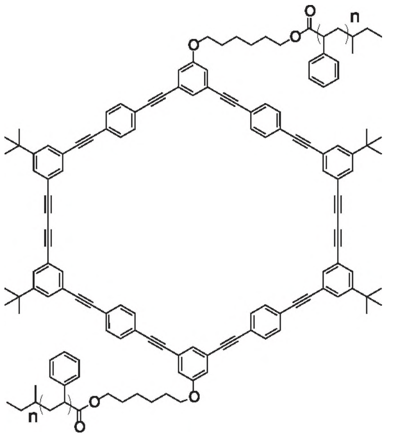

Figure 7.1: *Chemical structure of the shape-persistent coil-ring-coil macrocycle (n≈25).*

fringence Δn (magnetic birefringence). Since Δn depends on size, order, and aggregate density, we can follow the time-dependent aggregation process in solution in a contact-free way.

In cyclohexane, the macrocycle forms fibers that can be transferred to a mica substrate by drop-casting [11] [12]. Because of the effects of solvent evaporation and molecule-substrate interactions, atomic force microscopy (AFM) is not suited for studying the kinetics, but it is useful for visualizing the fiber morphology (Figure 7.2 (a)). The fibers all have a diameter of 5 nm and are not clustered.

The length distribution was determined by analyzing the length of 103 fibers in the AFM picture of Figure 7.2 (a). Fibers with a length shorter than 0.25 μm were hard to recognize in the AFM picture and were therefore ignored in the analysis. The length histogram displays the typical exponential distribution expected for supramolecular aggregates with an average length of 1.6 ± 0.1 μm (Figure 7.2 (b)) [15].

To estimate the persistence length l_p, we compared the length and end-to-end distance of 87 free-laying fibers in the AFM image with the theoretical prediction for equilibrated fibers and trapped fibers (Figure 7.2 (c)) [16] [17]. This shows that the fibers are equilibrated on the surface, giving $l_p = 1.0 \pm 0.2$ μm. The persistence length of semi-flexible aggregates is important for magnetic alignment.

Underneath the fibers, an additional layer is visible in the AFM images. It consists of a macrocycle layer with holes, formed by the unaggregated mono-

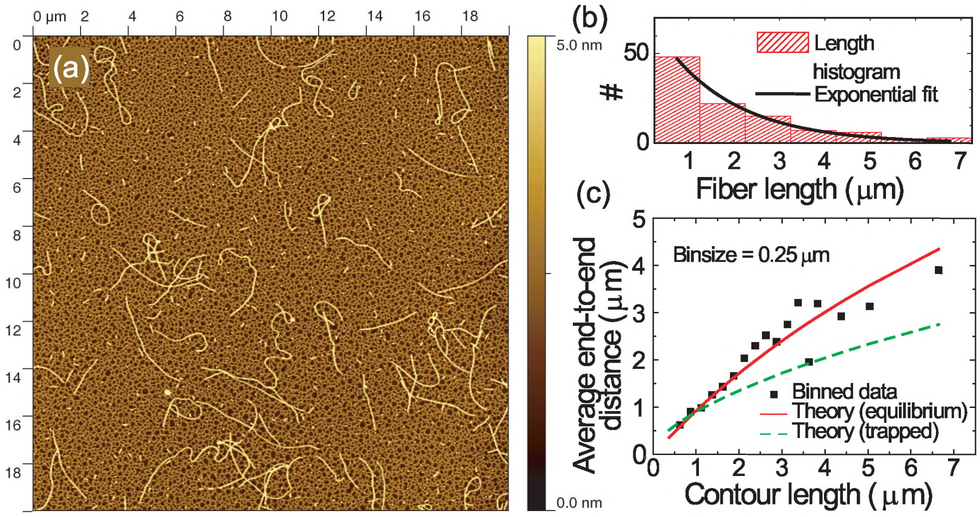

Figure 7.2: *(a) AFM image of a 10^{-6} M solution drop-cast on mica at room temperature, showing the fibers. (b) Histogram of aggregate length (based on 103 fibers longer than 0.25 μm, bin size = 1 μm). The fit yields a typical length of 1.6 ± 0.1 μm. (c) Measured average end-to-end distance versus the contour length for the fibers from the AFM analysis, compared to the theoretical curves for equilibrated (red solid line) and trapped fibers (green dashed line) [17].*

mers. The holes are not uniform in dimension and are probably formed due to dewetting phenomena. Upon dilution of the drop-cast solution the holes become larger. The aggregates in this background layer are formed during evaporation of the solvent due to molecule-substrate interactions, and are not present in solution [18].

Experimental details

AFM was performed with a commercial (multi mode) AFM operating in tapping mode. A calibration silicon grating was used to calibrate the piezo scanner. Both topographical and amplitude images were recorded under ambient conditions (air environment and room temperature) with scan rates less than 1 Hz, collecting 512 x 512 points for each image. The commercial rectangular silicon cantilevers from Veeco (115-135 μm long, 30-40 μm wide, 3.5-4.5 μm thick) have a nominal spring constant in the range of 20-80 N/m and a resonance frequency of 260-303 KHz.

The magnetic field induced birefringence was measured with the setup described in Chapter 2. The sample was contained in a 5 mm optical cell (Hellma) with a water-based temperature controller (± 0.1 °C). The magnetic birefringence was measured by slowly sweeping the magnetic field between 0 and 20 T. The small birefringence of the pure solvent, caused by the experimental setup, was used as a background.

The light scattering measurements were performed with a computerized homemade goniometer, using a step size of 1 degree in the angular range of 30 to 110 degrees, corresponding to the scattering wave vectors of 1.1×10^7 to 3×10^7 m^{-1} (an extensive description of the scattering setup can be found in Chapter 3). The scattered intensity was measured using a single mode optical fiber with a collimating lens in combination with an ALV/SO-SIPD single photon detector, using a 5 s integration time per angle. A water based temperature controller was used to stabilize the temperature within 0.1 K during the measurements.

The UV-vis absorbance spectra were measured with a home-made setup. Unpolarized light from a halogen-deuterium light source (Avantes, DH2000) was guided to the sample through an optical fiber (Thorlabs, multimode fiber). The light transmitted through was collected by a second fiber that coupled the light into a spectrometer (Ocean Optics, SD2000) containing a grating and a diode array (resolution 0.5 nm). The sample was stored in a temperature controlled bath, from which it was shortly taken out to measure a spectrum.

We measured the magnetic birefringence of a 10^{-4} M macrocycle solution in cyclohexane up to 400 h after cooling to the measurement temperature T_f (10, 14, 16, or 18 °C). Between the measurements, the samples were not exposed to a magnetic field. To start, the solution was heated above 35 °C for 15 min to dissolve all of the aggregates, as verified by light scattering. The sample was then cooled to T_f using air and a water bath, yielding an average cooling rate of ~1-2 K/min. A T_f lower than 10 °C resulted in coagulation of the solvent ($T_{melt} = 6.59$°C). For a T_f higher than 18 °C, no (ordered) aggregates were observed on an experimentally accessible time scale. The UV-vis absorbance was measured for comparable time scales and temperatures as the magnetic birefringence measurements, to probe the aggregation process with an additional independent technique.

Results

A set of magnetic birefringence curves as a function of time after preparation is shown in Figure 7.3 (a). At early times, there is no birefringence. With

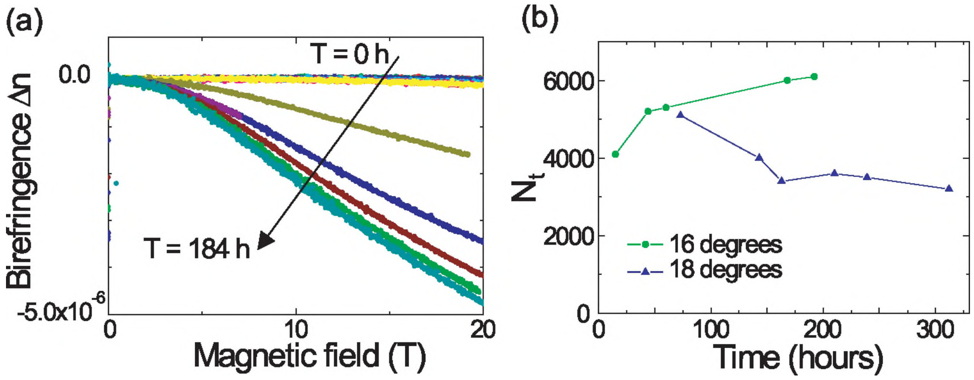

Figure 7.3: *(a) Time dependent magnetic birefringence curves at $T_f = 16$ °C. Right after cooling down (t = 0 h), there is no birefringence. In time, the signal increases until it saturates after ∼ 180 h. (b) Number of molecules per aggregate N_t, obtained by fitting the birefringence curves, as a function of time for $T_f = 16°C$ and $T_f = 18°C$. Assumed is an exponential distribution of aggregate sizes $P(N) \sim \exp(-N/N_t)$.*

time, an appreciable signal develops that resembles the usual $\mathcal{S}$-shaped curve (see Chapter 2). For low field strengths, Δn increases quadratically with B, followed by a slower increase in the intermediate regime up to 20 T. Application of higher fields would further increase the alignment until the birefringence saturates, but this would require fields higher than 20 T for the macrocycle aggregates.

Figure 7.4 (a) shows the magnetic birefringence caused by the macrocycle alignment at B = 20 T as a function of time after cooling. We can distinguish three different time regimes, which we will discuss on the basis of the $T_f = 14$ °C measurements. Immediately after the system is cooled, there is no birefringence signal, and there is no change in the UV-vis absorbance spectrum (Figure 7.5) that would indicate aggregation (*vide infra*). However, light scattering experiments indicate the presence of large objects characterized by strong scattering, predominantly at small scattering vectors (Figure 7.6 (a)). The objects are so large that they precipitate, causing a decrease in the scattering intensity in time. The absence of both a magnetic birefringence signal and a shift of the absorbance maximum proves that these objects have a negligible degree of (long-range) order (regime I in Figure 7.4 (b)).

To observe the morphology of the disordered objects, AFM was performed on a 10^{-4} M solution at 18 °C, 1 hour after cooling down, drop-casted on mica (Figure 7.6 (b)). A clear difference can be observed between the mica substrate

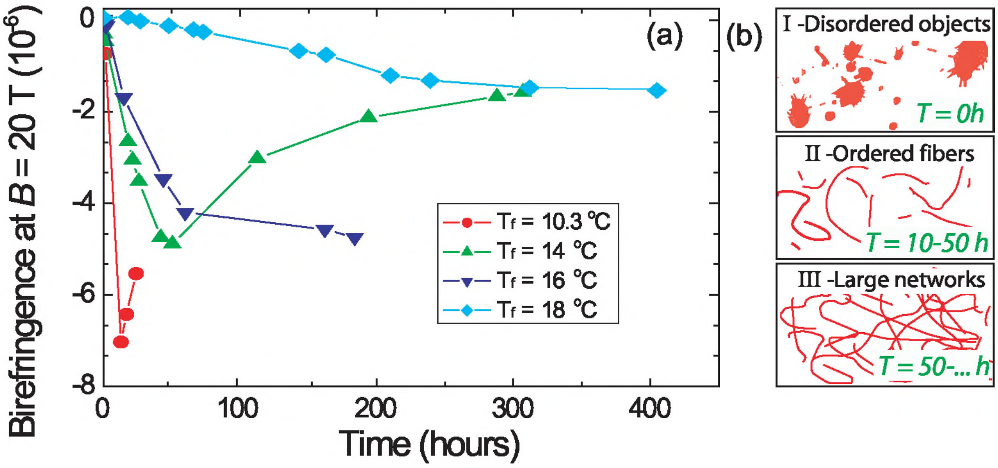

Figure 7.4: *(a) Solution birefringence at $B = 20$ T as a function of time for different temperatures T_f. (b) Schematic representation of the situation at $T_f = 14°C$ showing the transition from disordered objects (I) to ordered fibers (II) to a large network of fibers (for low T_f) (III).*

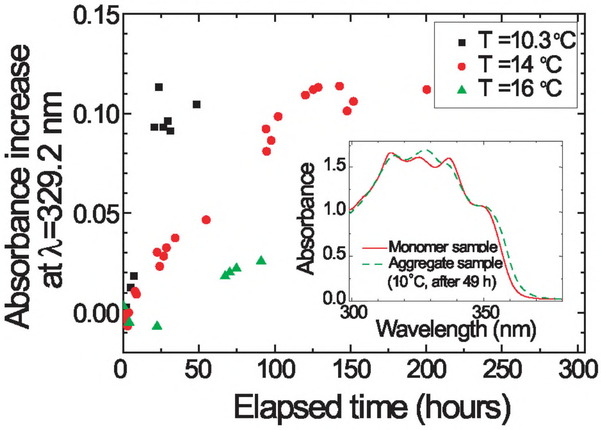

Figure 7.5: *Time dependent increase of the absorbance at $\lambda = 329.2$ nm (aggregate peak) for $T_f = 10.3$, 14 and 16 °C. Spectra were normalized at λ=315.1 nm, the absorbance maximum of the monomer solution. Inset shows the full spectra of a solution with monomers and aggregates respectively.*

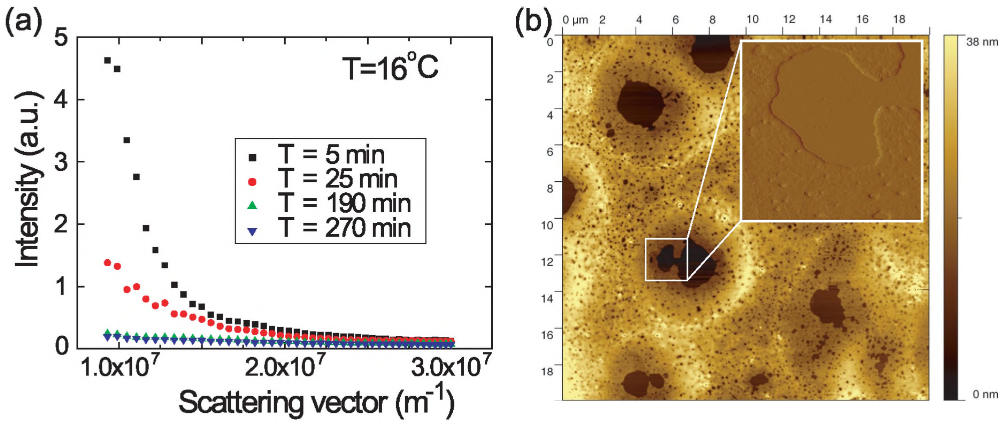

Figure 7.6: *(a) Static light scattering measured at several moments after cooling down. The strong scattering at low scattering vectors indicates the presence of large objects. (b) AFM topography image of a* 10^{-4} *M solution, drop casted from a solution at 18 °C, 1 hour after cooling down. Inset shows an amplitude image of the selected area. No fiber-shaped aggregates can be observed.*

(flat holes) and the macrocycle layer. In contrast to an AFM image of a solution stored in the fridge for several weeks, no fibers are observed after evaporation of the solvent. Due to the high concentration, it was difficult to determine the shape and size of the disordered objects.

During a period of a few days, the disordered objects are transformed into ordered fibers, which can be aligned in a magnetic field (regime II), causing Δn and the aggregate absorbance to increase in time (*vide infra*). We can exclude the presence of other aggregate morphologies, since AFM [18] and small-angle X-ray scattering [19] have shown that over a range of concentrations and temperatures, only fiber-shaped aggregates exist in equilibrated solutions.

After 50 h, the fibers slowly cluster to form a network (regime III), causing a reduced Δn. We verified that this reduction was not caused by precipitation. The network formation only occurs for $T_f < 16$°C and can be observed with the naked eye (Figure 7.7). A small rise in temperature quickly breaks up this network; drop-casting a solution with networks on mica at room temperature still results in individual fibers on the substrate (Figure 7.2 (a)).

The formation of ordered aggregates leads to a change in the UV-vis absorbance spectrum due to the coupling of molecular dipole moments. Figure 7.5 shows the absorbance at $\lambda = 329.2$ nm (aggregate peak) for the absorbance spectra normalized at λ=315.1 nm (monomer peak). For all temperatures, the

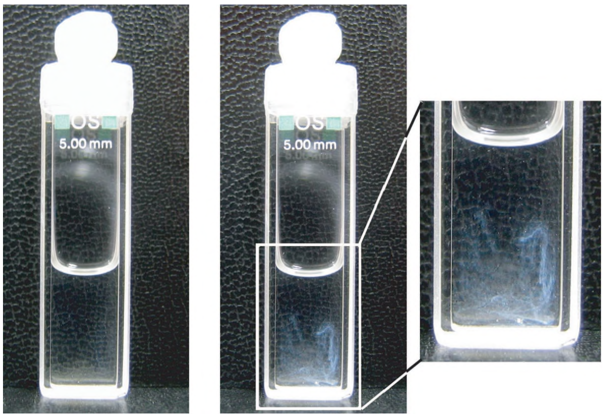

Figure 7.7: *Pictures of a cuvet with the macrocycle solution. The left picture shows a cuvet at 18 °C, the right picture (with close up) shows a cuvet at 10 °C. The white substance observed in the right cuvet is a network of fibers.*

spectrum right after cooling is identical to the monomer spectrum. For the lower temperatures, the aggregate peak increases in time with respect to the monomer peak, indicating the formation of ordered aggregates. For T_f=18 °C (not shown in the graph), the change in the absorbance spectrum is too small to measure the kinetics of the transformation, because of the low fraction of aggregated molecules. The saturation values of the absorbance are different for the different temperatures. The difference is caused by the temperature dependence of the fraction of aggregated molecules, and by the fact that the absorbance measurements were done on different samples, which may have resulted in a small variation in the concentrations. The time scales found are comparable to the time scales found with magnetic birefringence.

Discussion

Figure 7.4 (b) shows a schematic representation of the three regimes. After cooling down, disordered large objects are formed (regime I). In time, these objects are slowly transformed to ordered fibers (regime II). The average fiber length in this regime was determined by fitting the shapes of the Δn curves (Figure 7.3) with equation (2.20) on page 17. The molecular principle magnetic susceptibilities were calculated by summing the susceptibilities of the individual chemical groups ($\chi_{xx} = \chi_{yy} = -1.8 \times 10^{-9}$ and $\chi_{zz} = -1.2 \times 10^{-8}$ m^3/mol) [20] [13]. We found that on average an aggregate consists of ~5000 molecules, and that the aggregate size is essentially constant over time. If an intermolecular distance of 0.6 nm is assumed [19], this corresponds to an average fiber length of 2-3 μm, which agrees reasonably well with the length found by AFM for $C = 10^{-6}$ M. For the lowest temperatures, the ordered fibers of regime II cluster together, forming a big network (regime III).

The time scale on which the conversions between consecutive regimes take place is slow and strongly temperature-dependent: the lower T_f, the faster the kinetics. At $T_f = 18$ °C, the transformation of disordered objects to ordered fibers takes more than 300 h, whereas this time shortens to 50 h at 14 °C and to 10 h at 10 °C. These time scales are consistent with UV-vis absorbance measurements. Only for $T_f = 18$ °C was the fraction of aggregated material too low to observe a change in the absorbance spectrum upon aggregation. This further confirms the usefulness of magnetic birefringence as compared with UV-vis absorbance.

To summarize, cooling a monomeric solution leads to the fast formation of large disordered objects that are slowly converted into thermodynamically stable, ordered fibers, either directly or via an intermediate step of monomers. The conversion kinetics depends on the energetic landscape, including the barriers between the monomeric-, ordered- and disordered states, each of which can depend on temperature in a different way, causing the unexpected inverse temperature dependence of the fiber formation rate.

Conclusion

In conclusion, we have used magnetic birefringence as a new, sensitive technique to probe the kinetics of supramolecular aggregation. We have found three consecutive stages for the macrocycle system: disordered objects, ordered fibers, and a network. The transition rate from disordered objects to ordered conjugated fibers is low and increases with decreasing temperature T_f. Linking aggregation kinetics to molecular properties will lead to a better understanding of the mechanisms by which molecules self-assemble, and the use of magnetic fields can be a valuable tool for these studies.

References

[1] Service, R.F., *Science*, **309** (5731), 95, 2005.

[2] Pasternack, R.F., Gibbs, E.J., Collings, P.J., DePaula, J.C., Turzo, L.C., Terracina, A., *Journal of the American Chemical Society*, **120** (24), 5873-5878, 1998.

[3] Kerssemakers, J.W.J., Munteanu, E.L., Laan, L., Noetzel, T.L., Janson, M.E., Dogterom, M., *Nature*, **442** (7103), 709-712, 2006.

[4] Pasternack, R.F., Gibbs, E.J., Bruzewicz, D., Stewart, D., Engstrom, K.S., *Journal of the American Chemical Society*, **124** (14), 3533-3539, 2002.

[5] Zhang, L., Eisenberg, A., *Macromolecules*, **32** (7), 2239-2249, 1999.

[6] Jyothish, K., Hariharan, M., Ramaiah, D., *Chemistry - A European Journal*, **13** (20), 5944-5951, 2007.

[7] Pasternack, R.F., Fleming, C., Herring, S., Collings, P.J., DePaula, J., DeCastro, G., Gibbs, E.J., *Biophysical Journal*, **79** (1), 550-560, 2000.

[8] Lohr, A., Lysetska, M., Würthner, F., *Angewandte Chemie International Edition*, **44** (32), 5071-5074, 2005.

[9] Smulders, M.M.J., Schenning, A.P.H.J., Meijer, E.W., *Journal of the American Chemical Society*, **130** (2), 606-611, 2008.

[10] Pasternack, R.F., Gibbs, E.J., Sibley, S., Woodard, L., Hutchinson, P., Genereux, J., Kristian, K., *Biophysical Journal*, **90** (3), 1033-1042, 2006.

[11] Rosselli, S., Ramminger, A.D., Wagner, T., Silier, B., Wiegand, S., Haussler, W., Lieser, G., Scheumann, V., Höger, S., *Angewandte Chemie-International Edition*, **40** (17), 3138-3141, 2001.

[12] Rosselli, S., Ramminger, A.D., Wagner, T., Lieser, G., Höger, S., *Chemistry-a European Journal*, **9** (15), 3481-3491, 2003.

[13] Gupta, R.R., Diamagnetische Suszeptibilität, Landolt Börnstein, Gruppe II Atom- und Molekularphysik, vol.16, Berlin, Springer, 1986.

[14] Christianen, P.C.M., Shklyarevskiy, I.O., Boamfa, M.I., Maan, J.C., *Physica B: Condensed Matter*, **346-347**, 255-261, 2004.

[15] Van der Schoot, P., Supramolecular Polymers, 2nd ed., Ciferri, A., Ed., CRC Press, Boca Raton, 2005.

[16] Rivetti, C., Walker, C., Bustamante, C., *Journal of Molecular Biology*, **280** (1), 41-59, 1998.

[17] Samori, P., Ecker, C., Gossl, I., De Witte, P.A.J., Cornelissen, J.J.L.M., Metselaar, G.A., Otten, M.B.J., Rowan, A.E., Nolte, R.J.M., Rabe, J.P., *Macromolecules*, **35** (13), 5290-5294, 2002.

[18] Ver Heyen, A., Unravelling and guiding the molecular self-assembly on surfaces, *Thesis Katholieke Universiteit Leuven*, Leuven, 2008.

[19] Dingenouts, N., Klyatskaya, S., Rosenfeldt, S., Ballauff, M., Höger, S., *Macromolecules*, **42** (15), 5900-5902, 2009.

[20] Maret, G., Dransfeld, K., Biomolecules and Polymers in High Steady Magnetic Fields. In Strong and Ultrastrong Magnetic Fields and Their Applications, Herlach, F., Ed. Springer: New York, 1985; pp 143-204.

Summary

Creating new well-defined structures with a nanometer or micrometer length scale is of great importance, which can lead to new devices, new materials, and allows the study of fundamental physical phenomena. A promising approach for creating such structures is the use of organic molecules that spontaneously form higher dimensional structures in solution. The goal is to use carefully designed molecules to create so called supramolecular aggregates. In plain words, the process of supramolecular self-assembly can be compared to *LEGO*. *LEGO* pieces, as analogue to the organic molecular building blocks, can be designed to attach to each other in a unique and predictable way. By making clever combinations, complicated structures can be created, containing thousands of individual pieces.

With this process, extremely small self-repairing structures can be created in a relatively cheap and easily processable way. Almost any shape and size is possible, ranging from large spherical aggregates with a diameter in the micrometer range, to small wires of only a few nanometers thin. There are many applications, for example in the transport of light through narrow channels, as miniature gas sensors or as small capsules in drug delivery systems.

In this thesis, we use magnetic fields to improve our understanding of the formation of supramolecular self-assemblies. Due to the anisotropic magnetic properties of the molecules, a supramolecular aggregate can be oriented in a magnetic field. The way it aligns, parallel or perpendicular to the magnetic field, and the field strength required for the alignment, depends on the size, degree of order, and the intermolecular organization of the aggregate.

We investigate the relation between environmental aspects (like temperature and solvent) and the shape and internal structure of the resulting aggregates, we influence the shape with a magnetic field, we compare the growth process with theoretical models and we describe the kinetics of an aggregate system. Understanding these aspects leads to a better understanding of the formation process, which will allow us to build aggregates with the desired size, shape and functionality.

Chapter 2 describes the theory of aligning supramolecular aggregates in magnetic fields. Because of the optical anisotropy of the molecular building blocks, the alignment results in anisotropic refractive indices of the solution parallel and perpendicular to the magnetic field respectively. The presented theory allows us to relate the magnetic field induced birefringence to the internal organization, size and internal order of aggregates. It also describes the setup for measuring the birefringence, which is extensively used throughout this thesis.

Chapter 3 describes the use of laser light scattering as an additional technique to measure the size and shape of aggregates in solution. We describe the experimental setup, and give an introduction to dynamic and static light scattering, illustrated with some examples. In principle, no magnetic fields are involved in a light scattering experiment. However, in a magnetic field the orientational distribution function of the aggregates changes and thereby the diffusivity. We discuss the consequences for a light scattering experiment, and we show that the alignment improves the accuracy in the case of anisotropically shaped aggregates.

In Chapter 4 we use magnetic alignment to determine the internal organization of elongated sexithiophene aggregates in solution, by combining small-angle X-ray scattering and magnetic birefringence. The different aggregate axes can be probed independently by performing the X-ray experiments on magnetically aligned aggregates. This allowed us to reveal the shape and internal aggregate structure: a multi-walled rigid cylinder, which is considerably different from aggregate types found in other solvents. This result could only be obtained using a combination of techniques in the presence of a magnetic field.

In addition to an induced alignment, a magnetic field can influence the morphology of aggregates. A recent example is the deformation of sexithiophene vesicles in a magnetic field. In Chapter 5, we describe the extraordinary behavior of micrometer long thiacyanine fibers in a magnetic field. In a relatively low magnetic field of 2 T, the fiber morphology reversibly changes from a flexible worm to a rigid rod. To investigate the origin of this change in flexibility, we have characterized the magnetic properties of the fibers, using a complementary set of techniques, including magnetic birefringence, polarized absorbance and small angle X-ray scattering. We find that the fibers have a 6-8 nm diameter, with a brickwork molecular arrangement and that they can be aligned in fields in excess of 15 T. We think that the rigidification of the fibers is caused by a field induced change in the internal structure, rather than by the simple magnetic alignment of fiber segments.

Chapter 6 deals with some theoretical aspects of aggregate formation. Several models have been developed to describe the growth of different supramolecular systems. We have investigated the growth mechanism of oligo (p-phenylene-vinylene) aggregates using a complementary set of techniques: atomic force microscopy, dynamic light scattering, magnetic birefringence and circular dichroism spectroscopy. We have determined the temperature dependent length of the chiral fibers in solution, and we have determined the relevant thermodynamic parameters within a cooperative-growth model. A large number of techniques is essential to perform this type of study at all concentrations.

For the last chapter, we have used magnetic field induced birefringence as a new sensitive technique to probe the aggregation kinetics of macrocyclic molecules in solution. We have found three consecutive aggregation stages. Right after cooling a monomeric solution, we have observed the formation of disordered objects. These objects cannot be aligned in a magnetic field. In time, these objects are transformed into ordered fibers that can be aligned. The transition from disordered objects to ordered fibers is found to be very slow, taking days or weeks to complete. Waiting even longer will cause the ordered fibers to form a network at low temperatures. We anticipate that linking aggregation kinetics to molecular properties will lead to a better understanding of the mechanisms by which molecules self-assemble. Magnetic fields can be a valuable tool for these studies.

Samenvatting

Het maken van kleine structuren met een typische lengteschaal van nanometers of micrometers is een interessant onderzoeksgebied. Niet alleen vanwege de ontwikkeling van nieuwe materialen en toepassingen, maar ook omdat deze structuren ons in staat stellen om natuurwetenschappelijke verschijnselen op een hele kleine schaal te bestuderen. Een veelbelovende strategie om deze nanostructuren te maken, blijkt het gebruik van organische moleculen te zijn. Deze kunnen in oplossing onderling bindingen aan gaan en zo een groter object vormen, een zogeheten supramoleculair aggregaat. Vrijwel elke denkbare vorm en afmeting is mogelijk, variërend van micrometer grote bollen tot kleine draadjes van slechts enkele nanometers dik. De toepassingen hiervan zijn zeer divers. Voorbeelden zijn kleine transportkanaaltjes voor licht, gas sensoren of capsules voor het overbrengen van medicijnen. Simpel gezegd is de vorming van supramoleculaire aggregaten te vergelijken met *LEGO*, waarin de moleculen te vergelijken zijn met *LEGO* blokjes. De blokjes zijn speciaal ontworpen zodat ze maar op één bepaalde manier op elkaar passen. Door slimme combinaties te maken kun je ingewikkelde structuren maken die wel uit duizenden blokjes bestaan.

Dit proefschrift beschrijft het onderzoek aan supramoleculaire structuren in hoge magneetvelden. Omdat de moleculen in deze structuren er, net als *LEGO* blokjes, verschillend uitzien langs de verschillende symmetrie-assen, hebben ze ook anisotrope magnetische eigenschappen. Hierdoor kun je de aggregaten uitlijnen in een sterk magneetveld. De manier van uitlijnen, bijvoorbeeld loodrecht of juist parallel aan de richting van het magneetveld, en de sterkte van het benodigde veld, hangt af van de grootte, de mate van ordening, en de structuur in het aggregaat. We hebben onderzocht hoe de vorm en structuur van een aggregaat afhangt van de omgevingsfactoren (bijv. oplosmiddel en temperatuur), de vorm beïnvloed met een magneetveld, en we hebben gekeken naar hoe snel en hoe lang de aggregaten groeien. Een beter begrip van deze aspecten stelt ons in staat om aggregaten te maken met een goed gedefinieerde afmeting, vorm en functionaliteit.

Hoofdstuk 2 beschrijft de theorie van het uitlijnen van aggregaten in een magneetveld. Omdat de moleculen een optische anisotropie bezitten, heeft een oplossing met uitgelijnde aggregaten dubbelbrekende eigenschappen: de brekingsindices voor licht met een polarisatie parallel en loodrecht op de veldrichting zijn verschillend. De beschreven theorie relateert de dubbelbreking aan de interne structuur en het aantal moleculen in de aggregaten. Ook de opstelling voor het meten van dubbelbreking, die veelvuldig gebruikt is voor het onderzoek in dit proefschrift, staat beschreven.

Hoofdstuk 3 beschrijft het gebruik van lichtverstrooiing als aanvullende techniek om de vorm en afmeting van supramoleculaire aggregaten te bepalen. De opstelling staat beschreven, en een korte inleiding op statische- en dynamische lichtverstrooiing wordt gegeven, geïllustreerd met enkele voorbeelden. Normaal gesproken spelen magneetvelden geen rol bij lichtverstrooiingsexperimenten, maar omdat de oriëntatie van de aggregaten in een magneetveld verandert, kan het de resultaten van een verstrooiingsexperiment wel beïnvloeden. In dit hoofdstuk laten we zien dat de nauwkeurigheid van verstrooiingsexperimenten vergroot kan worden door het gebruik van magneetvelden.

In Hoofdstuk 4 gebruiken we het magnetisch uitlijnen om de interne structuur van sexithiofeen-aggregaten in oplossing te bepalen, dankzij een gecombineerd röntgenverstrooiings- en dubbelbrekingsexperiment. Door de gebruikte technieken konden we langs de verschillende assen van het aggregaat de ordening bekijken. Hieruit bleek dat dat de aggregaten cilindervormig waren en uit verschillende concentrische lagen bestonden. Dit is een heel andere structuur dan die voorheen in andere oplosmiddelen was gevonden. De exacte interne organisatie kon allen bepaald worden dankzij de toepassing van verschillende technieken in een magneetveld.

Magneetvelden kunnen niet alleen gebruikt worden voor het uitlijnen van aggregaten, soms kan ook de vorm van een aggregaat veranderen in een veld. Recentelijk bleek het bijvoorbeeld mogelijk om met een magneetveld bolvormige aggregaten te vervormen tot ellipsoïdes. In Hoofdstuk 5 beschrijven we het bijzondere gedrag van thiacyanine aggregaten. In een magneetveld van slechts 2 T veranderen deze aggregaten van flexibele slierten in starre cilinders. Dit proces is volledig reversibel, als het magneetveld weer wordt uitgezet worden de fibers weer flexibel. Om dit proces van veranderde flexibiliteit beter te uitlijnen, hebben we de fibers in een magneetveld bestudeerd met een combinatie van technieken: X-ray verstrooiing, dubbelbreking en gepolariseerde absorptie. Hieruit blijkt dat de fibers een diameter hebben van slechts 6-8 nm, en dat de moleculen in de fiber geordend zitten zoals bakstenen in een gemetselde muur. De veranderende flexibiliteit lijkt veroorzaakt te worden door een structurele verandering in de fibers.

In Hoofdstuk 6 hebben we het groeiproces van oligo (p-phenylene-vinylene) aggregaten bestudeerd met een combinatie van verschillende technieken: AFM, dynamische lichtverstrooiing, magnetisch dubbelbreking en circulair dichroïsme. We hebben bij verschillende temperaturen de lengte bepaald, deze vergeleken met de verschillende groeimodellen die hiervoor ontwikkeld zijn, en hieruit de bijbehorende thermodynamische constanten bepaald. Een beter begrip van dit groeiproces stelt ons in staat die groei te optimaliseren, en daarmee betere en complexere structuren te maken.

In het laatste hoofdstuk hebben we het magnetisch uitlijnen gebruikt om kinetische aspecten te meten van de vorming van macrocycle fibers in oplossing. We hebben gezien dat de vorming uit drie fases bestaat. Vlak na het afkoelen van een oplossing met macrocycle moleculen worden grote ongeordende objecten gevormd, die niet kunnen worden uitgelijnd met een magneetveld. Langzaam worden deze objecten omgezet in geordende fibers, die wel uitlijnen in een magneetveld. Deze omzetting duurt erg lang, en de snelheid blijkt omgekeerd evenredig met de temperatuur. Na nog langere tijd clusteren de fibers samen in een netwerk. Het is belangrijk om dit soort processen te begrijpen, omdat het ons in staat stelt om controle te krijgen op de tijdschaal waarop aggregaten worden gevormd, wat van groot belang is voor de orde van de aggregaten. Magneetvelden kunnen hier bij een belangrijke rol spelen.

List of publications

1. Gielen, J.C., Takazawa, K., Shklyarevskiy, I.O., Portale, G., Bras, W., Maan, J.C., Christianen, P.C.M., Magnetic field induced rigidification of thiacyanine nanofibers, *in preparation.*

2. Gielen, J.C., Smulders, M.M.J., George, S.J., Jonkheijm, P., Byelov, D., Van der Schoot, Maan, J.C., Meijer, E.W., Schenning, A.P.H.J., Christianen, P.C.M., Characterizing the growth process of oligo(p-phenylene vinylene) aggregates, *in preparation.*

3. Van Herrikhuyzen, J., Willems, R., George, S.J., Flipse, C., Gielen. J.C., Christianen, P.C.M., Schenning, A.P.H.J., Meskers, S.C.J., AFM nanomanipulation of shape persistent, self-assembled oligo(p-phenyelene vinylene) gold nanoparticles, *submitted to the Journal of the American Chemical Society.*

4. Helmich, F., Lee, C.C., Nieuwenhuizen, M.M.L., Gielen, J.C., Christianen, P.C.M., Larsen, A., Fytas, G., Leclère, P.E.L.G., Schenning, A.P.H.J., Meijer, E.W., Dilution-induced Self-assembly of Porphyrin Fibers, *accepted in Angewandte Chemie.*

5. Moes, M.J.A., Gielen, J.C., Bleichrodt, R.J., Van Loon, J.J.W.A., Christianen, P.C.M., Boonstra, J., Simulation of microgravity by magnetic levitation and random positioning: effect on human A431 cell morphology, *Microgravity Science and Technology*, submitted.

6. Lakhwani, G., Gielen, J.C., Kemerink, M., Christianen, P.C.M., Janssen, R.A.J., Meskers, S.C.J., Intensive Chiroptical Properties of Chiral Polyfluorenes Associated with Fibril Formation, *Journal of Physical Chemistry B* **113**(43) 14047-14051 (2009).

7. Gielen, J.C., Ver heyen, A., Klyatskaya, S., Vanderlinden, W., Höger, S., Maan, J.C., De Feyter, S., Christianen, P.C.M., Aggregation Kinetics of

Macrocycles Detected by Magnetic Birefringence, *Journal of the American Chemical Society*, **131**(40), 14134-14135 (2009).

8. Van den Heuvel, M., Prenen, A.M., Gielen, J.C., Christianen, P.C.M., Broer, D.J., Löwik, D.W.P.M., Van Hest, J.C.M., Patterns of Diacetylene-Containing Peptide Amphiphiles Using Polarization Holography, *J. Am. Chem. Soc.*, **131** (41), 15014-15017 (2009).

9. Gielen, J.C., Shklyarevskiy, I.O., Schenning, A.P.H.J., Christianen, P.C. M., Maan, J.C., Using magnetic birefringence to determine the molecular arrangement of supramolecular nanostructures, *Science and Technology of Advanced Matererials* **10**, 014601 (2009).

10. Janssen, P.G.A., Jabbari-Farouji, S., Surin, M., Vila, X., Gielen, J.C., De Greef, T.F.A., Vos, M.R.J., Bomans, P.H.H., Sommerdijk, N.A.J.M., Christianen, P.C.M., Leclere, P., Lazzaroni, R., Van der Schoot, P., Meijer, E.W., Schenning, A.P.H.J., Insights into Templated Supramolecular Polymerization: Binding of Naphthalene Derivatives to ssDNA Templates of Different Lengths, *Journal of the American Chemical Society* **131**(3), 1222–1231 (2009).

11. Gielen, J.C., Wolffs, M., Portale, G., Bras, W., Henze, O., Kilbinger, A.F.M., Feast, W.J., Maan, J.C., Schenning, A.P.H.J., Christianen, P.C. M., Molecular Organization of Cylindrical Sexithiophene Aggregates Measured by X-ray Scattering and Magnetic Alignment, *Langmuir* **25**(3), 1272–1276 (2009).

12. Matmour, R., De Cat, I., George, S.J., Adriaens, W., Leclere, P., Bomans, P.H.H., Sommerdijk, N.A.J.M., Gielen, J.C., Christianen, P.C.M., Heldens, J.T., Van Hest, J.C.M., Lowik, D.W.P.M., De Feyter, S., Meijer, E.W., Schenning, A.P.H.J., Oligo(p-phenylenevinylene)-Peptide Conjugates: Synthesis and Self-Assembly in Solution and at the Solid-Liquid Interface, *Journal of the American Chemical Society* **130**(44), 14576–14583 (2008).

13. Jakobs, R.T.M., Van Herrikhuyzen, J., Gielen, J.C., Christianen, P.C.M., Meskers, S.C.J., Schenning, A.P.H.J., Self-assembly of amphiphilic gold nanoparticles decorated with a mixed shell of oligo(p-phenylene vinylene)s and ethyleneoxide ligands, *Journal of Materials Chemistry* **18**(29), 3438–3441 (2008)

14. Van Herrikhuyzen, J., Portale, G., Gielen, J.C., Christianen, P.C.M., Sommerdijk, N.A.J.M., Meskers, S.C.J., Schenning, A.P.H.J., Disk mi-

celles from amphiphilic Janus gold nanoparticles, *Chemical Communications* **6**, 697–699 (2008).

15. Janssen, P.G.A., Jonkheijm, P., Thordarson P., Gielen, J.C., Christianen, P.C.M., Van Dongen, J.L.J., Meijer, E.W., Schenning, A.P.H.J., Tuning the self-assembly of a ditopic crown ether functionalized oligo(p-phenylene-vinylene), *Journal of Materials Chemistry* **17**(25), 2654–2660 (2007).

16. Jeukens, C.R.L.P.N., Jonkheijm, P., Wijnen, F.J.P., Gielen, J.C., Christianen, P.C.M., Schenning, A.P.H.J., Meijer, E.W., Maan, J.C., Polarized emission of individual self-assembled oligo(p-phenylene vinylene)-based nanofibers on a solid support, *Journal of the American Chemical Society* **127**(23), 8280–8281 (2005).

Curriculum Vitae

Jeroen Gielen is geboren op 11 oktober 1983 te Utrecht. Hij behaalde zijn gymnasium diploma aan het Kandinsky College te Nijmegen, waarna bij begon met de studie Natuur- en Sterrenkunde aan de (toen nog) Katholieke Universiteit Nijmegen. Zijn afstudeerstage deed hij op de afdeling Experimentele Vaste Stoffysica 1/High Field Magnet Laboratory, met als onderwerp fluorescentiemicroscopie aan supramoleculaire nanostructuren. Hij studeerde af in 2005 aan de (inmiddels) Radboud Universiteit Nijmegen. Daarna begon hij met zijn promotieonderzoek onder leiding van dr. P.C.M. Christianen en prof.dr.ir. J.C. Maan. De belangrijkste resultaten hiervan staan beschreven in dit proefschrift.